POLITECNICO DI MILANO

SCUOLA DI INGEGNERIA INDUSTRIALE E DELL'INFORMAZIONE

Corso di Laurea Magistrale in Ingegneria Matematica

Thermo-Electro-Chemical Modeling and Simulation of Ion Transport in Nanochannels

Relatore: Prof. Riccardo Sacco

Co-relatore: Prof. Joseph W. Jerome

Tesi di Laurea Magistrale di:

Fabio Manganini

Matr. 770306

Anno Accademico 2012 - 2013

Contents

List of Figures

List of Tables

Abstract

Cellular biology is regulated by the exchange of electric charge and chemicals between the intracellular and extracellular environments. Such exchange is operated by ionic channels, which are protein tunnels across the cell membrane walls filled with ions and water. Ionic channels are responsible for fundamental functions in the life of organisms: control of electrical signaling in the nervous system; coordination of muscle contraction (in particular the heart); regulation of uptake of foodstuffs in the intestine, secretion of hormones, and many more.

Recent discoveries in bio- and nano-technology have given the opportunity of building synthetic nanochannels, which have a wide range of applications: biosensing, DNA detection, drug delivery and nanofluidics. The study of ionic transport is thus crucial for controlling the flow of ions across the nanopore and for understanding how biological channels function. To this purpose, theoretical and computational modeling of ionic transport can be used as a supporting tool to experimental analysis and design of bio-synthetic structures.

In this thesis work a novel contribution to the modeling and simulation of ion channels is the introduction of a hierarchy of hydrodynamic models for charge transport through ionic channels. Special interest is devoted to the analysis of temperature changes and consequent thermal exchanges, which are usually neglected in conventional theories. Extensively conducted simulations indicate that temperature changes affect ion permeation in the nanochannels studied here. Simulations also display a strong dependence of the computed solutions on saturation velocity parameter, which can affect system behaviour with respect to heat changes since it prescribes the collision frequency of ions. Lack of quantitative information of such parameter is a limitation of the present analysis and deserves further experimental investigation. Finally, computational experiments demonstrate that the effect of nonlinear convective terms is relatively small so that they can be neglected without severely affecting the accuracy of the prediction of system dynamics.

Introduzione

La biologia cellulare è regolata dallo scambio di carica elettrica e sostanze chimiche tra l'ambiente intracellulare e l'ambiente che circonda la cellula.

Tale scambio è gestito dai canali ionici, che sono fondamentalmente proteine cave che attraversano le pareti della membrana cellulare, e sono riempite di ioni e molecole d'acqua. I canali ionici sono responsabili di attività fondamentali per la vita delle cellule e degli organismi. Ad esempio, essi controllano la trasmissione del segnale elettrico nel sistema nervoso, coordinano la contrazione dei muscoli (in particolare il cuore), regolano l'assorbimento di cibo nell'intestino, la secrezione di ormoni, e altro ancora.

Gli sviluppi recenti nel campo della Nanotecnologia permettono di fabbricare con materiali sintetici canali ionici di dimensioni nanometriche (nanopori) utilizzabili in numerose applicazioni, ad esempio, la biopercezione, la rilevazione del DNA, la diffusione e rilascio di farmaci e la nanofluidica. Lo studio del trasporto degli ioni è quindi cruciale non solo per controllare il flusso di ioni attraverso il nanoporo, ma anche per capire come funzionano i canali dal punto di vista biologico. A questo proposito, la modellizzazione teorica e computazionale del trasporto ionico può essere vantaggiosamente utilizzata sia come uno strumento di supporto per l'analisi sperimentale e la progettazione di nuove strutture bio-sintetiche, sia per poter meglio caratterizzare i principi fondamentali del comportamento biologico delle cellule.

In questo lavoro di tesi viene fornito un nuovo contributo nell'ambito della modellizzazione e simulazione di canali ionici introducendo una gerarchia di modelli idrodinamici per la descrizione e lo studio del trasporto di carica attraverso i canali ionici, con applicazioni a importanti canali proteici ed a basilari dispositivi bio-ibridi. Particolare interesse è rivolto all'analisi degli scambi termici tra gli ioni che fluiscono nel canale e il fluido interstiziale, un aspetto del problema biofisico che è solitamente trascurato nelle teorie tradizionali.

Il Capitolo 1 è diviso in due parti principali: nella prima parte, forniamo un'introduzione dal punto di vista biologico dei canali ionici e spieghiamo

i motivi per cui essi hanno un ruolo fondamentale per la vita delle cellule. In seguito, nella seconda parte, introduciamo il lettore ai recenti sviluppi raggiunti nella Nanotecnologia, con particolare enfasi alla progettazione e fabbricazione di nanocanali sintetici in una vasta gamma di applicazioni bio-ingegneristiche. Particolare cura è dedicata ad illustrare i principi basilari del funzionamento di nanocanali sintetici, i quali si comportano in modo molto simile ai dispositivi a semiconduttore, come per esempio i diodi a giunzione *pn*.

Il legame tra biologia ed elettronica è analizzato in dettaglio nel Capitolo 2, nel quale viene derivata una gerarchia di modelli matematici per la descrizione del moto di particelle cariche in un mezzo materiale (cationi ed anioni in soluzione acquosa) seguendo l'approccio della fisica dei dispositivi a semiconduttore. Tale approccio consiste nell'applicare il metodo dei Momenti all'Equazione di Trasporto di Boltzmann (insieme ad appropriate condizioni di chiusura) con lo scopo di ottenere sistemi di leggi di conservazione per il flusso convettivo e diffusivo di massa, calore e carica. A tali sistemi va aggiunta la risoluzione dell'equazione di Poisson per il potenziale elettrostatico per determinare in modo auto-consistente la distribuzione del campo in corrispondenza di una data densità di carica ionica mobile e di un dato profilo di densità di carica fissa nel canale. In ordine crescente di complessità, la gerarchia comprende:

- il modello Drift Diffusion (DD) (noto come sistema Poisson Nernst Planck (PNP) nella letteratura biofisica);
- il modello elettro-termico (ET);
- il modello idrodinamico (HD);
- il modello termo-idrodinamico (THD).

Nel caso del più semplice modello PNP, il flusso di corrente viene calcolato ignorando la dissipazione di calore verso il mezzo. Tuttavia, è ben noto che il contributo al bilancio termico tra cariche mobili e mezzo materiale fornito dal flusso di carica riveste un ruolo significativo nei dispositivi a semiconduttore (l'effetto Joule), cosicchè una generalizzazione della teoria PNP per i canali ionici in biologia sembra un naturale avanzamento per migliorare l'accuratezza del modello. Il modello ET prescrive un'unica temperatura per il sistema acqua-più-ioni; il modello HD impiega diverse temperature per ciascuna specie ionica ma la temperatura dell'acqua è mantenuta ad un valore costante; inoltre il modello HD tiene conto anche di termini convettivi non lineari; infine, il modello THD estende la formulazione HD aggiungendo

un'equazione per il flusso di calore del fluido interstiziale del canale.

Nel Capitolo 3 illustriamo lo schema generale che abbiamo utilizzato per risolvere numericamente il modello THD in una geometria monodimensionale e in condizioni stazionarie. Il sistema viene risolto in maniera disaccoppiata estendendo all'attuale impostazione THD la mappa iterativa di Gummel che è un'iterazione di punto fisso largamente utilizzata nel trattamento computazionale del modello DD per la simulazione di dispositivi a semiconduttore. Ad ogni passo della procedura iterativa di Gummel, si risolve una successione di equazioni alle derivate parziali fino ad ottenere una soluzione auto-consistente. Ogni equazione nell'algoritmo è riconducibile ad un problema ai limiti modello (BVP) della forma diffusione-trasporto-reazione.

Il Capitolo 4 tratta della soluzione numerica del sopracitato BVP per mezzo di un'approssimazione ad Elementi Finiti (FE). Nello specifico, utilizziamo il metodo Duale Misto Ibridizzato (DMH), che è caratterizzato da proprietà di conservazione, da risultati di convergenza ottimali e da un costo computazionale comparabile a quello della usuale discretizzazione FE con formulazione agli spostamenti.

Il Capitolo 5 introduce il contetto di principio del massimo continuo (CMP) per un operatore ellittico del second'ordine. Viene affrontata anche la controparte discreta del CMP, ovvero il principio del massimo discreto (DMP). Dimostriamo che, adottando appropriate tecniche di stabilizzazione numerica (diagonalizzazione della matrice dei flussi e diffusione artificiale), la soluzione discreta calcolata dal metodo DMH soddisfa un DMP, da cui segue che viene eliminata alla radice la possibile insorgenza di oscillazioni numeriche in presenza di termini di trasporto e/o reazione dominanti senza peraltro ridurre l'accuratezza della soluzione calcolata.

Nel Capitolo 6 viene condotta un'estesa validazione numerica dei modelli e dei metodi computazionali proposti in questo lavoro di tesi nella simulazione di svariati tipi di nanocanali biologici e sintetici. L'attenzione è rivolta allo studio dei profili di temperatura previsti dai modelli THD, HD o ET e di come le variazioni di temperatura influiscano sulle relazioni corrente-tensione (I-V) rispetto al modello base DD (PNP).

Nel Capitolo 7, vengono riassunti i prinicipali aspetti della trattazione teorica e computazionale svolta nel lavoro di tesi, indicando anche possibili sviluppi successivi di ricerca nell'ambito della modellazione e simulazione dei canali ionici.

Introduction

Ionic channels are responsible for fundamental functions in the life of cells and organisms. For example, they control electrical signaling in the nervous system; they coordinate the contraction of muscles (in particular the heart); they regulate uptake of foodstuffs in the intestine, secretion of hormones, and many more.

Recent development in bio- and nano-technology allow to build synthetic nanochannels that can be used in a wide range of applications: biosensing, DNA detection, drug delivery and nanofluidics.

The study of ionic transport is, therefore, crucial not only for controlling the flow of ions across the nanopore, but also for understanding how biological channels function. In this respect, theoretical and computational modeling of ionic transport can be profitably used as a supporting tool to experimental analysis and design of novel bio-synthetic structures as well as for better characterizing fundamental principles of biological cellular behaviour.

In this thesis work a novel contribution in the area of modeling and simulation of ion channels is given by introducing a hierarchy of hydrodynamic models for the description and investigation of charge transport through ionic channels with application to significant channel proteins and basic bio-hybrid devices. Special interest is devoted to the analysis of temperature changes and consequent thermal exchanges between ions flowing in the channel and the interstitial channel fluid, which are usually neglected in conventional theories.

Extensively conducted simulations indicate that temperature changes affect ion permeation in nanochannels. Simulations also show the dependence of the computed solutions on model parameters, particularly the saturation velocity v_{sat}, whose precise quantitative characterization is yet an open issue that warrants further experimental investigation and subsequent model calibration. Finally, computational experiments demonstrate that nonlinear convective terms give a relatively small contribution to ion flow so that they can be neglected without severely affecting the accuracy of the prediction of system dynamics.

Chapter 1 is divided into two main parts: in the first part, we give an introduction to the biology of ion channels and to the reason why they have a fundamental role in the life of cells. Then, in the second part, we introduce the reader to the recent developments achieved in Nanotechnology, with particular emphasis on the design and fabrication of syntethic nanochannels in a wide range of applications in bio-engineering. Special care is devoted to illustrating the basic functioning principles of syntethic nanochannels which act in a very similar manner to that of semiconductor devices, such as diodes.

The link between biology and electronics is exploited in Chapter 2, where a hierarchy of mathematical models that describe motion of charged particles in a medium (cations and anions into water solution) is derived following the approach of semiconductor device physics. The approach consists in applying the Moments method to the Boltzmann Transport Equation (together with appropriate closure assumptions) in order to derive systems of conservation laws that describe the diffusive and convective flow of mass, heat and charge. The Poisson equation for the electrostatic potential must be adjoined to determine the self-consistent distribution of the field in correspondence of a given ionic mobile charge density and a given fixed charge density in the channel. In increasing order of complexity, the hierarchy includes:

- the Drift Diffusion (DD) model (which is also well-known as Poisson Nernst Planck (PNP) system in the biophysics literature);
- the electro-thermal (ET) model;
- the hydrodynamic (HD) model;
- the thermo-hydrodynamic (THD) model.

In the simplest PNP model, current flow is predicted ignoring heat dissipation to the medium. However, heat contribution to charge flow is well known to play a significant role in semiconductor devices (Joule heating effects, for example), so that a generalization of the PNP theory of ion channels in biology seems to be a natural step to improve modeling accuracy. The ET model prescribes equal temperature for the water-plus-ions system; the HD model uses different temperatures for each ion species but water temperature is held at a fixed value; furthermore the HD model accounts for nonlinear convective terms; finally, the THD model extends the HD formulation by adding a heat flow equation for the interstitial channel fluid.

In Chapter 3 we illustrate the general scheme we have used for numerically solving the THD model in a one dimensional geometry and at steady-state.

The system is solved in a decoupled fashion by extending to the present THD setting the Gummel iterative map which is a fixed point iteration widely used in the computational treatment of the DD model in semiconductor device simulation. At each step of the Gummel iterative procedure, a sequence of linear partial differential equations is solved until a self-consistent solution is obtained. Each equation in the algorithm is represented by a boundary value model problem (BVP) of diffusion-advection-reaction form.

Chapter 4 deals with the numerical solution of the above BVP problem by means of a Finite Element (FE) approximation. The approach we use is the dual mixed hybridized (DMH) method, which is characterized by conservation properties, optimal convergence results and a computational effort comparable to that of a standard displacement-based FE discretization.

Chapter 5 introduces the concept of continuous maximum principle (CMP) for a second order elliptic operator. The discrete counterpart of the CMP, that is, the discrete maximum principle (DMP), is also addressed. We prove that, adopting appropriate numerical stabilization techniques (lumping of the flux mass matrix and artificial diffusion), the discrete solution computed by the DMH method satisfies a DMP, thus numerical oscillations that arise in the case of dominating advection and/or reaction terms are suppressed.

In Chapter 6 we perform an extensive numerical validation of models and computational methods proposed in this thesis work in the simulation of several types of biological and synthetic nanochannels. The focus is on the study of temperature profiles predicted by THD, HD or ET models and how temperature changes affect the current-voltage (I-V) relations compared to the basic DD (PNP) model.

Chapter 7 contains a summary of the main theoretical and computational aspects that have been covered in the present thesis, illustrating also possible further research developments in the area of modeling and simulation of ionic nanochannels.

Chapter 1

Biological and Electronic Views of Particle Transport through the Cell Membrane

In this Chapter, we give a general introduction to the biological setting which is the object of the thesis work. In particular, we aim at illustrating the role of ionic channels in the regulation of the electrical cellular activity and their connection with electronic devices.

In Section 1.1, we give a brief description on how *ionic channels* can generate electrical current in cells, thus providing a fundamental aspect in the life of biological systems. For more detailed information, we refer to [47, 44, 11].

In Section 1.2, we list some applications in biotechnology in order to emphasize the importance of studying ionic channels and their corresponding synthetic devices (nanochannels, nanopores, nanofluidic diodes), which have greatly attracted the interest of the scientific community in recent years. We outline similarities (and differences) between the motion of ions through biological channels and the motion of charge in semiconductor devices, thus introducing a link between the biological view and the electronic view of the problem at hand.

1.1 Ion transport through cell membranes

The basic living unit of the body is the *cell*: each organ is an aggregate of many different cells held together by intercellular supporting structures. The entire body, then, contains about 100 trillion cells ($\sim 10^{14}$ cells). Although the many cells of the body often differ markedly from one another (since each

type of cell is specially adapted to perform one or a few particular functions), all of them have certain basic characteristics that are alike: a typical cell, as seen by the light microscope, is shown in Figure 1.1. Its two major parts are the nucleus and the cytoplasm. The nucleus is separated from the cytoplasm by a nuclear membrane, and the cytoplasm is separated from the surrounding fluids by a *cell membrane*.

The principal fluid medium of the cell is *water*, which is present in most cells, except for fat cells, in a concentration of 70 to 85 per cent. Many cellular chemicals are dissolved in the water. Others are suspended in the water as solid particulates. Chemical reactions take place among the dissolved chemicals or at the surfaces of the suspended particles or membranes.

Figure 1.1: Structure of the cell as seen with the light microscope.

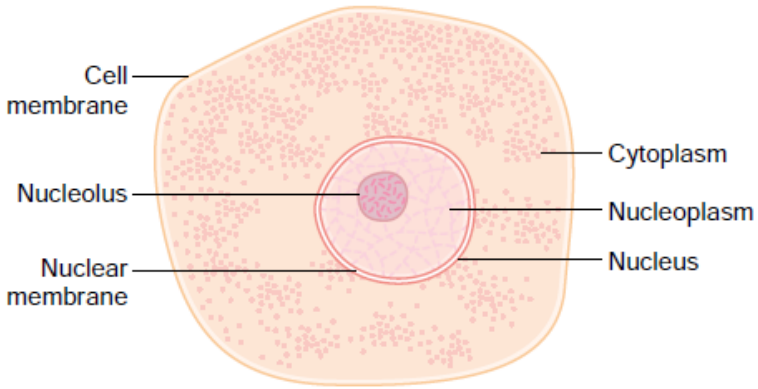

The cell membrane The cell membrane (also called the plasma membrane), which envelops the cell, is a thin, pliable, elastic structure with a thickness t_m of only 7.5 to 10 nanometers. The diameter d_c of cells varies from 7.5 to 150 micrometers . Thus, the ratio t_m/d_c varies in the range $50 \times 10^{-6} \div 1.3 \times 10^{-3}$. Despite of its relative small dimension, the cell membrane plays some fundamental roles for the living of the cell: it preserves the cell integrity separating the *intracellular fluid* from the *extracellular fluid* and it regulates the passage of substances from the outside to the inside of the cell, and viceversa.

The cell membrane consists almost entirely of a lipid bilayer, but it also contains large numbers of protein molecules in the lipid, many of which penetrate all the way through the membrane, as shown in Figure 1.2. Most of these penetrating proteins constitute a pathway through the cell membrane. Some proteins, called *channel proteins*, allow free movement of water as well

as selected ions or molecules. The channel proteins are usually highly selective with respect to the types of molecules or ions that are allowed to cross the membrane.

Figure 1.2: Cross-section of a cell membrane.

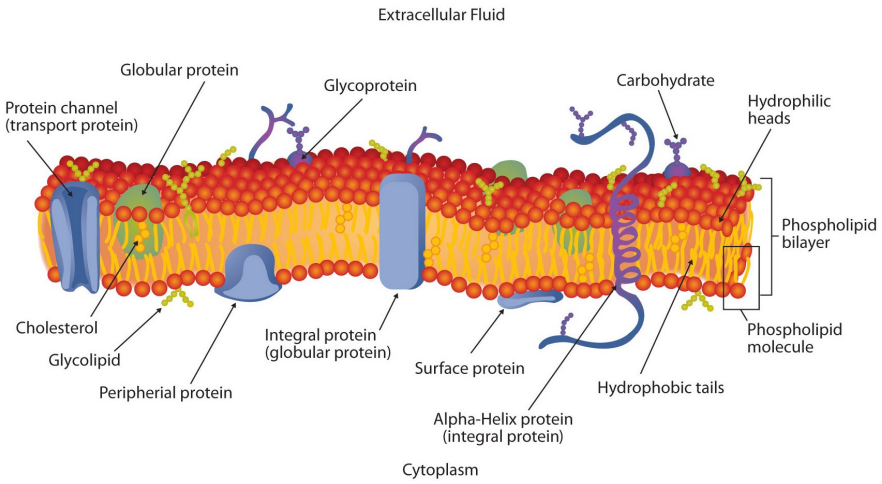

Ions provide inorganic chemicals for cellular reactions. Also, they are necessary for operation of some of the cellular control mechanisms. For instance, ions acting at the cell membrane are required for transmission of electrochemical impulses in nerve and muscle fibers. The most important ions in the cell are potassium K^+, magnesium Mg^{++}, phosphate, sulfate SO_4^{--}, bicarbonate HCO_3^-, and smaller quantities of sodium Na^+, chloride Cl^-, and calcium Ca^{++}. An ion is called *cation* if positively charged, *anion* if negatively charged.

Ionic channels Certain cells, commonly called excitable cells, are unique because of their ability to generate *electrical signals*. Some examples are neuron cells, muscle cells, and touch receptor cells. Like all cells, an excitable cell maintains a different concentration of ions in its cytoplasm than in its extracellular environment. Together, these concentration differences create a small *electrical potential* across the plasma membrane. Then, when the potential difference reaches a threshold value, typically 55 millivolts, specialized channels in the plasma membrane, called *ion channels*, open and allow rapid ion movement into or out of the cell, and this movement creates an electrical signal.

Ionic channels are large proteins that reside in the membrane of cells (Figure 1.3) and conduct ions through a narrow tunnel of *fixed charge* formed

by the amino acid residues of the protein.

Channels are ideally placed (in membranes in series with the cell's interior) to control biological function [96]. Ion channels should be viewed as natural *nanotubes* that link the solutions in and outside cell to the electric field in the cell's membrane.

Figure 1.3: Ion channels function as pores to permit the flux of ions down their electrochemical potential gradient.

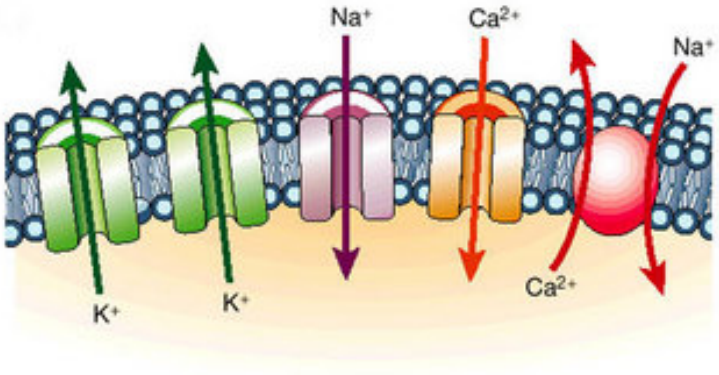

Channels are responsible for signaling in the nervous system, coordination of muscle contraction, and transport in all tissues. Channels are obvious targets for drugs and disease [87]: many of the drugs used in clinical medicine act directly or indirectly through channels.

Transport of charged particles In biological channels, ions move (mainly) under the control of gradients of *concentration* and *electric potential* [47]. The gradient of electric potential forces a particle to move accordingly to its sign. This mechanism is called *drift* (see Figure 1.4a). The gradient of concentration moves particles from regions at higher concentration to those at lower concentration. This mechanism is called *diffusion* (see Figure 1.4b). The flow of ions through the channel generates an *electrical current*. From a practical point of view, we are mainly interested in computing the current *density* $\mathbf{J}$, which allows to know how much charge crosses a generic cross-sectional area in a unit of time. When only drift and diffusion processes are considered, the current density takes the following form

$$\mathbf{J} = \mathbf{J}_{drift} + \mathbf{J}_{diffusion} \tag{1.1}$$

where the contributions due to drift and diffusion have been separated. Notice that $\mathbf{J}_{drift}$ and $\mathbf{J}_{diffusion}$ might act in opposite directions, in which case they tend to cancel out reciprocally, see Figure 1.4.

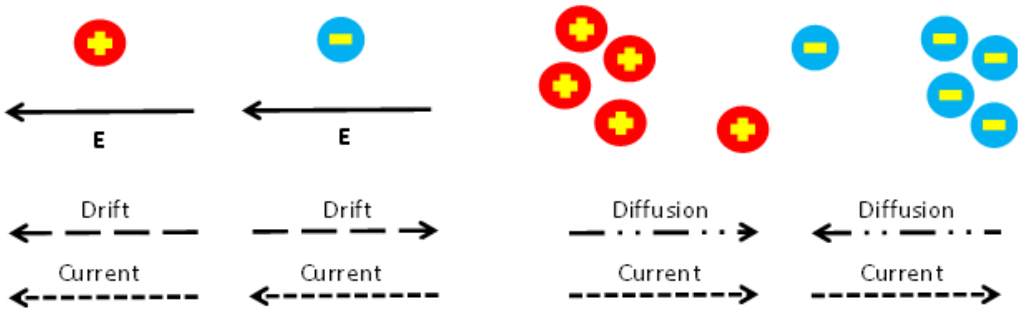

(a) Drift **(b)** Diffusion

Figure 1.4: Drift and diffusion processes. The current direction is (chiefly) that of the positive charges.

There are other processes that affect the constitutive characterization of the current density **J**. In this work, in addition to drift and diffusion driving forces, the effects of thermal gradients and convective terms will be accounted for with appropriate physical models. This issue will be the object of Chapter 2.

1.2 From biology to electronics

Ion channels in nanotechnology We have seen that transmembrane transport occurs via biological channels and pores, which lie at the heart of virtually any functioning living cell [47]. Because these channels are rather fragile and can function only when inserted in a lipid membrane, it is very hard to use them directly in man-made systems. The ionic channels, when used outside of a biological organism, could open a route to a variety of breakthrough applications in the field of biotechnology: biosensing [64, 34, 45, 68], modeling of biological channels [62, 93, 25], drug delivery [35] and nanofluidics [77, 80, 33, 57, 39, 32]. Accordingly, it is very attractive to construct solid-state pores, which would exhibit similar properties to those of biological channels but would be stable in a variety of dynamically changing operation conditions (such as temperature, pH, ionic strength). Researchers are trying to design practical machines that use ion channels. The emerging fields of nanofluidics and solid-state nanopores offer a variety of different platforms for the fabrication of such systems [1, 34, 64, 15, 104, 84, 3, 55, 106].

Engineering ion channels: nanofluidic devices Nanopipettes [103, 99] and nanopores [3, 92, 94] are the first relevant examples of a system that con-

trol ion flow electrically without the need of introducing moving (mechanical) parts. The next step forward is represented by the design and implementation of *ionic diodes* that function according to a similar mechanism as that of semiconductor diodes [100, 56]: one can turn off or on the ion flow by simply switching the polarity of the voltage bias along the device. Figure 1.7 shows a schematization of a pore that has been chemically modified to have positive and negative surface charges positioned along the channel walls. This pattern allows the pore to be used as a diode, one of the basic building blocks of an electronic circuit. Figure 1.5 shows the functioning scheme of a realistic nanofluidic diode, while Figure 1.6 shows some microscopic details of the device.

Figure 1.5: Figure from [27]. (a) Schematic diagram of a nanofluidic diode consisting of a positively charged surface and neutral surface in either half of the channel. The positive charge is produced by avidin while the neutral charge is produced by biotin moieties. (b) Epifluorescence image showing fluorescently labeled avidin in half the nanofluidic diode. (Reproduced with permission from Nano Lett., 2007, 7, 547.32) (c) and (d) Schematic diagram and microscopic image of a solid-oxide nanofluidic diode composed by Al2O3 and SiO2 nanochannels. (Reproduced with permission from ACS Nano, 2009, 3, 575.35).

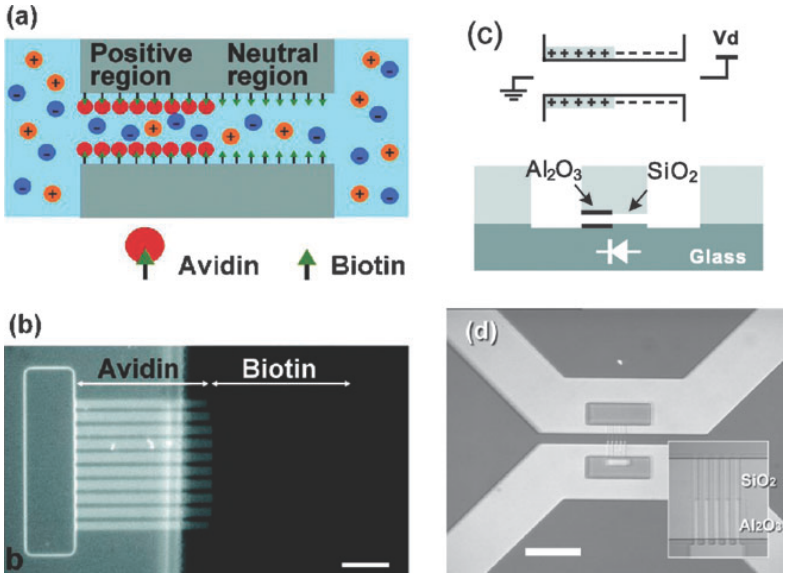

Analogies between nanofluidic and semiconductor devices There is a strong similarity in the physical principles that describe, on the one hand, the flow of electrons and holes in a doped semiconductor and, on the other hand, the flow of ions through a charged ion channel. In fact, both ions

Figure 1.6: Figure from [27]. (a) Phase-contrast microscopic top-view image of the device. Five 60 mm-long nanochannels connect between two microfluidic channels connecting the nanochannels and microchannels. The transparent bar lying across the nanochannels is a PDMS wall separating two microchannels. (b) Cross-section SEM image which shows that each nanochannel is 2.5 mm wide and about 20 nm thick. (Reproduced with permission from Nano Lett., 2007, 7, 3165.26)

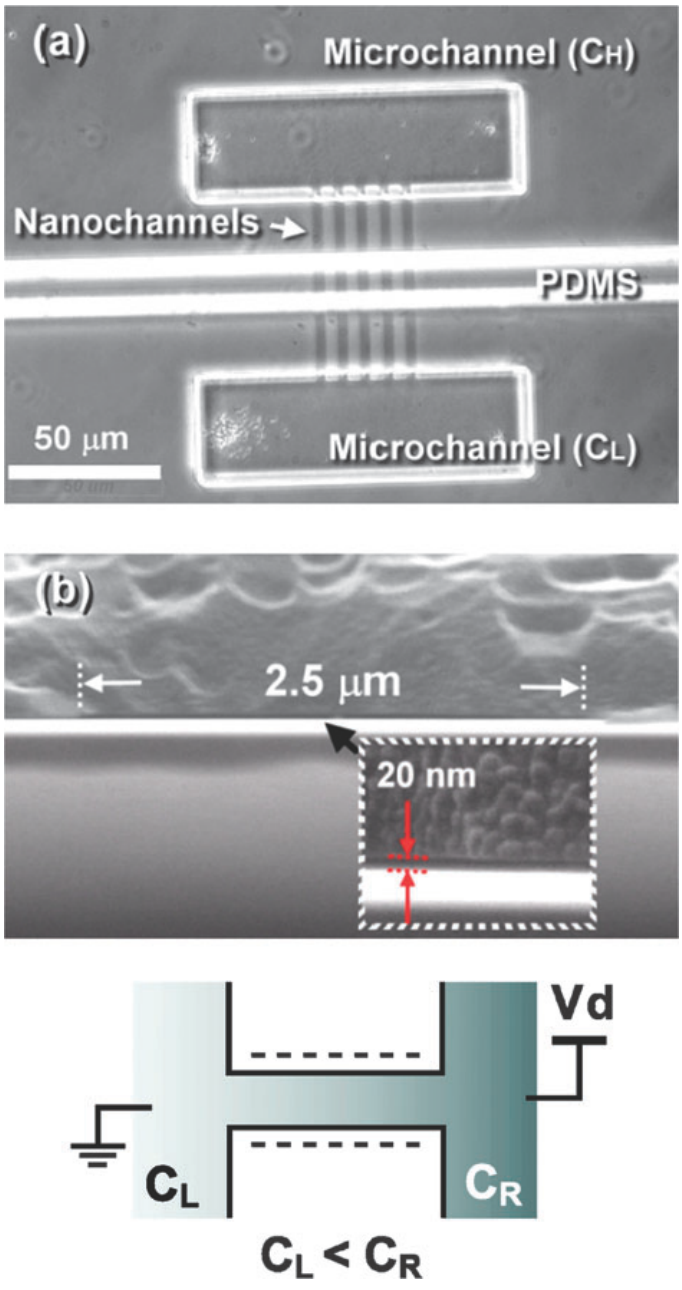

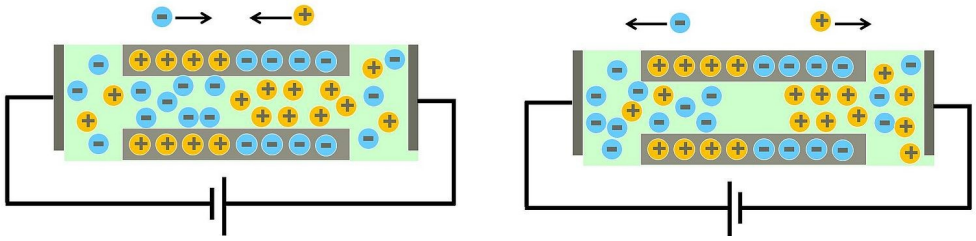

(a) Forward bias **(b)** Reverse bias

Figure 1.7: Schematic of a nanochannel diode. Ions accumulate at the junction under forward bias (left) but deplete from the junction under reverse bias(right).

and electrons flow by *diffusion* and *drift* mechanisms; they obey *Maxwell-Boltzmann* statistics [16] and the Debye-Huckle theory can handle both in terms of the *screening effect* of the electric field from the individual charged particles [37].

Another strong similarity is that the *permanent charge* in the selectivity filter of an ion channel plays an analogous role in ion conduction as the *doping profile* in regulating current transport (of quasi-particles) in a semiconductor [38]. The nanochannels with negative surface charges have enhanced cation concentration, while those containing positive surface charges have anions as majority charge carriers. This is analogous to the case of p-type and n-type semiconductors, respectively.

Finally, diodes and nanochannels share the phenomenon of Donnan equilibrium [59]. When two nanochannels with different surface charge polarities connect, the majority counter-ions from both sides diffuse across the junction and leave a fixed surface charge behind. The exposed surface charges generate a *Donnan potential*, which is equivalent to the *built-in potential* in a semiconductor system. These two potentials describe the same physical mechanism, which is to counterbalance the diffusion of mobile ions across the space charge region until the system reaches equilibrium.

Differences between nanofluidic and semiconductor devices While the semiconductor and nanofluidic systems share some similar attributes, they are also different in several aspects. First, in fluidic systems most of the cations and anions of interest *do not recombine* as electrons and holes do in semiconductors. In addition, the *mobilities* of ions in solutions are very small compared to the corresponding values for electrons and holes in typical semiconductors: the difference among these quantities being of $10^6 \div 10^7$ orders of magnitude.

Chapter 2

Physical Models for Transport of Charged Particles

In this chapter we show a hierarchy of mathematical models which describe the motion of charged particles in a medium. We are interested in a mixture of (monovalent) anions and cations, surrounded by water, passing through a nanofluidic channel. The formal derivation of the model equations relies on the analogy between ion transport in a biological channel and charge transport in semiconductor devices that has been outlined in Chapter 1. Thus, the equations are obtained using the notation and language of semiconductor device physics according to the historical fact that they were first derived for semiconductors in 60s and 70s [95, 12] while their application to biology is more recent [24].

The starting point is the *Boltzmann Transport Equation* (BTE), which is discussed in Section 2.1. Afterwards, by applying the *moments method* (Section 2.2), the equations for particle, momentum and energy conservation are obtained and grouped to form the so-called *Hydrodynamic* (HD) model , see Section 2.3. Section 2.4 lists the hierarchy of models based on the HD system.

Remark 2.1. About notation: symbol p used as subscript refers to positively charged particles (holes or cations); symbol n to negatively charged particles (electrons or anions). Symbol ν could be either p or n. When symbols $\mp$ or $\pm$ appear, the superior sign is always referred to n-type particles, the other to p-type particles. The value for ν must be chosen accordingly to that sign.

2.1 The Boltzmann Transport Equation

Maxwell equations [49] do not suffice in describing charge transport in semiconductors, since they do not give any information on how the current density should be expressed in terms of carrier concentration and electric potential. To exploit this relationship, charged carriers (*electrons* and *holes*) are treated as particles in a diluite gas, so that classical results from kinetic gas theory and mechanical statistics can be applied.

To this purpose, we follow the lines of [50, 88] and introduce the *distribution function* $f_\nu(\mathbf{x}, \mathbf{k}, t)$ that describes particle concentration ν in the phase space ($\mathbf{x}$ is the spatial coordinate, $\mathbf{k}$ the wave number and t denotes the time variable). The quantity $f_\nu(\mathbf{x}, \mathbf{k}, t)\, d\mathbf{x}\, d\mathbf{k}\, dt$ equals the number of particles in the phase space volume $d\mathbf{x}\, d\mathbf{k}\, dt$ centered around the point $(\mathbf{x}, \mathbf{k}, t)$.

Liouville theorem states that the number of particles in the phase space is time invariant [97, 60]:

$$\frac{d}{dt} f_\nu(\mathbf{x}(t), \mathbf{k}(t), t) = 0. \tag{2.1}$$

In other words, the number of particles entering the volume $d\mathbf{x}\, d\mathbf{k}\, dt$ placed around $\mathbf{x}$ with momentum $\mathbf{k}$ in a time interval dt must equal the number of particles leaving it within the same time.
By expanding the total time derivative, we obtain:

$$\frac{\partial f_\nu}{\partial t} + \frac{d\mathbf{x}}{dt} \cdot \nabla_{\mathbf{x}} f_\nu + \frac{d\mathbf{k}}{dt} \cdot \nabla_{\mathbf{k}} f_\nu = 0. \tag{2.2}$$

The carrier group velocity is:

$$\mathbf{u}_\nu = \frac{d\mathbf{x}}{dt} \tag{2.3}$$

The momentum $\mathbf{k}$ is related to the vector forces $\mathbf{F}$ by the impulse theorem:

$$\mathbf{F} = \frac{d}{dt}(\hbar \mathbf{k}). \tag{2.4}$$

where $\hbar = h/2\pi$ is the reduced Planck constant.
We split the forces into external and internal forces: $\mathbf{F} = \mathbf{F}_{ext} + \mathbf{F}_{int}$. If we neglect magnetic induction (i.e.: the Lorentz force), the external forces depend only on the electric field $\mathbf{E}$:

$$\mathbf{F}_{ext} = \mp q\mathbf{E}, \tag{2.5}$$

where q is the electron charge. We rewrite equation (2.2):

$$\frac{\partial f_\nu}{\partial t} + \mathbf{u}_\nu \cdot \nabla_{\mathbf{x}} f_\nu \mp \frac{q}{\hbar}\mathbf{E} \cdot \nabla_{\mathbf{k}} f_\nu = -C_{coll}, \tag{2.6}$$

where

$$C_{coll} := \mathbf{F}_{int}/\hbar \cdot \nabla_{\mathbf{k}} f_\nu. \tag{2.7}$$

Equation (2.6) expresses the balance between the rate of change of f_ν due to convection (the LHS) and the rate of change of f_ν due to collisions (the RHS). We refer to equation (2.6) as the Boltzmann Transport Equation (BTE).

The modeling of internal forces, i.e. the C_{coll} term, is a rather complicated task since several collision mechanisms are involved: electron-lattice, electron-ion collisions, and also inter-particle collisions of various type so that to calculate the effect of these mechanisms from the laws of dynamics, statistical laws have to be invoked.

We introduce the quantity $S(\mathbf{k}, \mathbf{k}')\, d\mathbf{k}'$ which is the probability per unit time that a carrier in the state $\mathbf{k}$ is scattered into the momentum volume $d\mathbf{k}'$. The explicit form for the *scattering rate* $S(\mathbf{k}, \mathbf{k}')$ is determined by the physical principles underlying each considered scattering mechanism; for some examples see [70, 73].
One way of writing the collision term is the following:

$$\begin{aligned} C_{coll}(\mathbf{x}, \mathbf{k}, t) = \int_B \{ & S(\mathbf{k}, \mathbf{k}') f_\nu(\mathbf{x}, \mathbf{k}, t)[1 - f_\nu(\mathbf{x}, \mathbf{k}', t)] \\ & - S(\mathbf{k}', \mathbf{k}) f_\nu(\mathbf{x}, \mathbf{k}', t)[1 - f_\nu(\mathbf{x}, \mathbf{k}, t)]\} d\mathbf{k}', \end{aligned} \tag{2.8}$$

where B is the first Brillouin zone. This expression accounts for short range interactions of particles with their environment (crystal impurities, phonons, etc.) but not for particle-particle interactions, otherwise this effect would result into a high non linearity in f_ν (the rate $S(\mathbf{k}, \mathbf{k}')$ would depend on f_ν in this case).
We can give a physical interpretation of equation (2.8) as follows: the rate of change of f_ν due to collisions at $(\mathbf{x}, \mathbf{k}, t)$ is given by the 'sum' of rates of particles being scattered from all possible states $(\mathbf{x}, \mathbf{k})$ into the state $(\mathbf{x}, \mathbf{k}')$ at the time t minus the 'sum' of rates of the particles being scattered from the state $(\mathbf{x}, \mathbf{k}')$ into any possible state $(\mathbf{x}, \mathbf{k})$ at time t.

By substituting (2.8) into (2.6), we obtain the Boltzmann Transport Esquation in explicit form:

$$\begin{aligned}
&\frac{\partial f_\nu}{\partial t} + \mathbf{u}_\nu \cdot \nabla_{\mathbf{x}} f_\nu \mp \frac{q}{\hbar}\mathbf{E} \cdot \nabla_{\mathbf{k}} f_\nu = \\
&= -\int_B \{S(\mathbf{k},\mathbf{k}') f_\nu(\mathbf{x},\mathbf{k},t)[1 - f_\nu(\mathbf{x},\mathbf{k}',t)] \\
&- S(\mathbf{k}',\mathbf{k}) f_\nu(\mathbf{x},\mathbf{k}',t)[1 - f_\nu(\mathbf{x},\mathbf{k},t)]\} d\mathbf{k}'.
\end{aligned} \tag{2.9}$$

This integro-differential equation allows, in principle, to calculate the function f_ν and then deduce the quantities of interest, namely carrier concentrations and velocities. However, a closed solution of (2.9) is possible only for very simple cases and with severe simplifications on the collision term.

Therefore, the most successful technique for solving the BTE is to simulate the motion of one or more carriers at microscopic level with Monte Carlo methods [17, 61]. These methods are very computationally intensive though, and so scarcely suitable for engineering and/or industrial applications. They are mainly adopted as a benchmark solution in the calibration of various parameters (diffusion coefficient, mobility, relaxation time, etc.).

We therefore seek alternative approaches to solve the BTE. A widely adopted method is the so called *moments method*, which elaborates the information hidden in the BTE in order to get simpler but still meaningful equations. This method is discussed is Section 2.2.

2.2 Moments method applied to the BTE

The BTE gives a *microscopic* description of carrier transport in terms of the distribution function f_ν in the seven-dimensional space $(\mathbf{x}, \mathbf{k}, t)$.

It is of advantage to simplify the equation by reducing the number of problem dimensions. Typically this is achieved by, first, multiplying both sides of BTE by suitable powers of $\mathbf{u}_\nu$, and then integrating the result over the $\mathbf{k}$ space. This leads to a set of equations in the $(\mathbf{x}, t)$ space only. Consequently, some information originally carried by the distribution function f_ν is lost. However, in many practical cases, the information retained by the equations in the $(\mathbf{x}, t)$ space is sufficient to capture the essential features of the problem [91].

The multiplication of BTE with increasing powers of the group velocity $\mathbf{u}_\nu$ and its subsequent integration over space $\mathbf{k}$ is called *moments method* [50, 82, 70]. It leads, in principle, to an infinite hierarchy of moments equations. We limit the analysis to the first three moments, namely the zeroth-, first-, and second-order moments.

The truncation by itself, however, does not give a closed system, since all the moments are coupled (see [70, Ch.2]). To overcome this difficulty,

the moment equations of the system are expressed in terms of suitable dependent *macroscopic* variables (for instance, the temperature) and the selection of compatible relations among these variables (*closure assumptions*) leads eventually to a closed system.

Another problem is that terms originating from the collision integral C_{coll} depend on the moments in a complicated manner. The critical issue of collision mechanism will be resolved using the so-called *relaxation-time* approximation.

2.2.1 Macroscopic variables

Before proceeding, we need to define some variables of physical interest as in the standard kinetic gas theory [48, 65]:

- **carrier concentration**

$$\nu = \int_B f_\nu \, d\mathbf{k}; \tag{2.10}$$

- **drift velocity**

$$\mathbf{v}_\nu = \frac{1}{\nu} \int_B \mathbf{u}_\nu f_\nu \, d\mathbf{k}; \tag{2.11}$$

- **momentum density**

$$\mathbf{p}_\nu = m_\nu \nu \mathbf{v}_\nu; \tag{2.12}$$

- **random velocity**

$$\mathbf{c}_\nu = \mathbf{u}_\nu - \mathbf{v}_\nu; \tag{2.13}$$

- **pressure tensor**

$$(P_\nu)_{ij} = m_\nu \int_B (c_\nu)_i (c_\nu)_j f_\nu \, d\mathbf{k}; \tag{2.14}$$

- **internal energy density**

$$e_{I\nu} = \frac{1}{2\nu} \int_B |\mathbf{c}_\nu|^2 f_\nu \, d\mathbf{k}; \tag{2.15}$$

- **heat flux**

$$(q_\nu)_i = \frac{m_\nu}{2} \int_B (c_\nu)_i |\mathbf{c}_\nu|^2 f_\nu \, d\mathbf{k}; \tag{2.16}$$

We have denoted with m_ν the effective mass of the carrier.

2.2.2 Derivation of the model

Following [50], we now derive the equations for charge, momentum and energy conservation of carriers as an application of the moments method to the BTE. For a generalized approach of moments method, we refer to [82].

We introduce the functions:

$$\begin{aligned} g_0(\mathbf{u}_\nu) &\equiv 1, \\ g_1(\mathbf{u}_\nu) &= m_\nu \mathbf{u}_\nu, \\ g_2(\mathbf{u}_\nu) &= \frac{m_\nu}{2}|\mathbf{u}_\nu|^2, \end{aligned}$$

and we state the assumption that f_ν decreases sufficiently rapidly at the boundary ∂B of the Brillouin zone:

$$\lim_{|\mathbf{k}|\to\partial B} g_i(\mathbf{u}_\nu) f_\nu(\mathbf{k}) = 0, \quad i = 0, 1, 2.$$

The following *integral identities* hold:

1. $\int_B (c_\nu)_i f_\nu \, d\mathbf{k} = 0$
2. $\int_B \frac{\partial f_\nu}{\partial k_i} \, d\mathbf{k} = 0$
3. $\int_B (u_\nu)_j \frac{\partial f_\nu}{\partial k_i} \, d\mathbf{k} = -\nu\delta_{ij}$
4. $\int_B |\mathbf{u}_\nu|^2 \frac{\partial f_\nu}{\partial k_i} \, d\mathbf{k} = -2\nu v_i,$

where δ_{ij} is the Kronecker symbol. The first identity follows from the definition of macroscopic variables, while the other identities follow from an integration by parts and the assumptions on f_ν above (remember also that, if the mass theorem applies, it holds $\frac{\partial (u_\nu)_i}{\partial k_j} = \frac{\hbar}{m_\nu}\delta_{ij}$). We will also use the identity

$$\int_B (u_\nu)_i (u_\nu)_j f_\nu \, d\mathbf{k} = \nu (v_\nu)_i (v_\nu)_j + \int_B (c_\nu)_i (c_\nu)_j f_\nu \, d\mathbf{k}, \tag{2.17}$$

which follows from an expansion of the components of $\mathbf{u}_\nu$ in terms of $\mathbf{c}_\nu + \mathbf{v}_\nu$ and using the integral identity 1., and the identity

$$\begin{aligned} &\frac{1}{2}\int_B (u_\nu)_i |\mathbf{u}_\nu|^2 f_\nu \, d\mathbf{k} \\ &= \frac{\nu (v_\nu)_i}{2}|\mathbf{v}_\nu|^2 + (v_\nu)_i \nu e_{I\nu} + \sum_j (v_\nu)_j (P_\nu)_{ij}/m_\nu + \frac{1}{2}\int_B (c_\nu)_i |\mathbf{c}_\nu|^2 f_\nu \, d\mathbf{k}, \end{aligned} \tag{2.18}$$

which follows again from an expansion of $\mathbf{u}_\nu$, from the definition of $e_{I\nu}$ and $\mathbf{P}_\nu$, and from the integral identity 1.

2.2.3 Moment of order 0: charge conservation

Equation (2.6) is multiplied by $g_0(\mathbf{u}_\nu)$ and integrated over the $\mathbf{k}$ space; using the integral identity 2., we immediately get:

$$\frac{\partial \nu}{\partial t} + \operatorname{div}(\nu \mathbf{v}_\nu) = \left(\frac{\partial \nu}{\partial t}\right)_{coll} \tag{2.19}$$

where

$$\left(\frac{\partial \nu}{\partial t}\right)_{coll} = -\int_B C_{coll}\, d\mathbf{k}. \tag{2.20}$$

Equation (2.19) expresses the conservation of charge: the increase of carrier density plus the outflow of carriers equals the increase of density due to collisions.

2.2.4 Moment of order 1: momentum conservation

Equation (2.6) is multiplied by $g_1(\mathbf{u}_\nu)$ and integrated over the $\mathbf{k}$ space; by the application of the definition of $\mathbf{P}_\nu$, the identity (2.17), and the integral identity 3., one finds:

$$\frac{\partial \mathbf{p}_\nu}{\partial t} + \mathbf{div}(\mathbf{p}_\nu \otimes \mathbf{v}_\nu) = \mp q\nu\mathbf{E} - \mathbf{div}\,\mathbf{P}_\nu + \left(\frac{\partial \mathbf{p}_\nu}{\partial t}\right)_{coll} \tag{2.21}$$

where

$$\left(\frac{\partial \mathbf{p}_\nu}{\partial t}\right)_{coll} = -m_\nu \int_B \mathbf{u}_\nu\, C_{coll}\, d\mathbf{k}. \tag{2.22}$$

The LHS of equation (2.21) is the rate of change plus the outflow of momentum density; the RHS represents the forces exerted by the electric field and by carrier pressure (mechanical force) and the rate of momentum density gained during collisions. The symbol $\otimes$ is the tensor-product among vectors $\mathbf{a}$ and $\mathbf{b}$ (also called dyadic product):

$$(\mathbf{a} \otimes \mathbf{b})_{ij} = a_i b_j$$

The divergence operator applied to the previous tensor can be expanded as:

$$\mathbf{div}(\mathbf{a} \otimes \mathbf{b}) = \mathbf{b} \operatorname{div} \mathbf{a} + (\mathbf{a} \cdot \nabla)\mathbf{b}$$

2.2.5 Moment of order 2: energy conservation

Equation (2.6) is multiplied by $g_2(\mathbf{u}_\nu)$ and integrated over the $\mathbf{k}$ space; by the application of the definition of $\mathbf{q}_\nu$, the identity (2.18), and the integral identity 4., one finds:

$$\frac{\partial}{\partial t}\left(\frac{m_\nu \nu}{2}|\mathbf{v}_\nu|^2 + m_\nu \nu e_{I\nu}\right) + \operatorname{div}\left(\mathbf{v}_\nu\left[\frac{m_\nu \nu}{2}|\mathbf{v}_\nu|^2 + m_\nu \nu e_{I\nu}\right]\right) = -\operatorname{div}(\mathbf{v}_\nu \mathbf{P}_\nu) \mp q\nu \mathbf{v}_\nu \cdot \mathbf{E} - \operatorname{div}\mathbf{q}_\nu + \left(\frac{\partial W_\nu}{\partial t}\right)_{coll} \quad (2.23)$$

where

$$\left(\frac{\partial W_\nu}{\partial t}\right)_{coll} = -\frac{m_\nu}{2}\int_B |\mathbf{u}_\nu|^2 \, C_{coll}\, d\mathbf{k}, \quad (2.24)$$

and the product $\mathbf{v}_\nu \mathbf{P}_\nu$ is a row vector-matrix multiplication. The scalar variable W_ν denotes the *total carrier energy* (per unit volume):

$$W_\nu = \frac{m_\nu}{2}\int_B |\mathbf{u}_\nu|^2 \, f \, d\mathbf{k} = \frac{m_\nu \nu}{2}|\mathbf{v}_\nu|^2 +_\nu \nu e_{I\nu}. \quad (2.25)$$

The *energy per unit concentration* is

$$w_\nu = W_\nu / \nu. \quad (2.26)$$

Equation (2.23) contains on the LHS, the time rate of change and the outflow of total energy, on the RHS the work performed by mechanical forces, the energy supplied by electrical forces to the carriers, the heat flux into the system and the rate of change of total energy density due to collisions.

2.2.6 Poisson equation

Equations (2.19), (2.21) and (2.23) constitute the mass, momentum and energy conservation system. In addition to these transport equations, one should consider the Maxwell equations to relate the electro-magnetic field with carrier concentrations. However, assuming to adopt the quasi-static approximation [88], the coupling between electric and magnetic fields is broken, thus one has to consider only the much simpler *Poisson equation*:

$$\operatorname{div}(\epsilon \mathbf{E}) = \rho, \quad (2.27)$$

ϵ being the dielectric constant of the lattice and ρ the space charge density, respectively. In a semiconductor $\rho = q(p - n + N_{dop})$, where p, n are hole

and electron concentrations, respectively, and N_{dop} is the doping profile concentration.
The electric field $\mathbf{E}$ is expressed in terms of the scalar electric potential ϕ

$$\mathbf{E} = -\nabla\phi. \tag{2.28}$$

Substituting (2.28) into (2.27) we have

$$-\operatorname{div}(\epsilon\nabla\phi) = q(p - n + N_{dop}). \tag{2.29}$$

2.2.7 Moment closure

In the case of one species of carrier, the system formed by equations (2.19), (2.21), (2.23) and (2.29) has 15 dependent variables, namely $\nu, \phi, \mathbf{v}_\nu, \mathbf{P}_\nu, e_{I\nu}$ and $\mathbf{q}_\nu$ ($\mathbf{P}_\nu$ is symmetric); the number of variables exceeds the number of equations, thus we need further relations among these variables to close the system.
We begin introducing a new tensor variable $\mathbf{T}_\nu$, the effective carrier *temperature*, which is related to the carrier pressure by the ideal gas law:

$$(P_\nu)_{ij} = \nu k_B (T_\nu)_{ij} \tag{2.30}$$

where k_B is the Boltzmann constant.

The following assumptions are made:

1. The pressure tensor $\mathbf{P}_\nu$ is *isotropic*, i.e., $(P_\nu)_{ij} = (P_\nu)_s \delta_{ij}$, for a suitable scalar function $(P_\nu)_s$. Notice that this amounts to neglecting shear viscosity. Using (2.14) and (2.15), the specific (i.e., per unit mass) pressure $(P_\nu)_s$ is related to $e_{I\nu}$ via $m_\nu \nu e_{I\nu} = \frac{3}{2}(P_\nu)_s$.

2. From the previous assumption and (2.30), the carrier temperature may be represented by a scalar quantity T_ν, related to internal energy by

$$m_\nu e_{I\nu} = \frac{3}{2} k_B T_\nu. \tag{2.31}$$

   Thus, the total carrier energy is

$$W_\nu = \frac{1}{2} m_\nu \nu |\mathbf{v}_\nu|^2 + \frac{3}{2} k_B \nu T_\nu \tag{2.32}$$

3. The heat flux $\mathbf{q}_\nu$ is expressed according to Fourier law as:

$$\mathbf{q}_\nu = -\kappa_\nu \nabla T_\nu, \tag{2.33}$$

where κ_ν is the thermal conductivity of the carrier. In semiconductor physics, the following relationship, known as Wiedmann-Franz law, holds

$$\kappa_\nu = \left(\frac{5}{2} + r\right)\left(\frac{k_B}{q}\right)^2 \varsigma T_\nu \tag{2.34}$$

where ς is the conductivity of the material and r is a constant, usually $r = -1$.

2.2.8 The moments system

Collecting equations (2.19), (2.21) and (2.23), and making use of the assumptions of Section 2.2.7, we can write the set of equations derived from the moments method for the carrier ν:

$$\frac{\partial \nu}{\partial t} + \operatorname{div}(\nu \mathbf{v}_\nu) = \left(\frac{\partial \nu}{\partial t}\right)_{coll} \tag{2.35a}$$

$$\frac{\partial \mathbf{p}_\nu}{\partial t} + \mathbf{v}_\nu \operatorname{div} \mathbf{p}_\nu + (\mathbf{p}_\nu \cdot \nabla)\mathbf{v}_\nu = \mp q\nu\mathbf{E} - \nabla(\nu k_B T_\nu) + \left(\frac{\partial \mathbf{p}_\nu}{\partial t}\right)_{coll} \tag{2.35b}$$

$$\frac{\partial W_\nu}{\partial t} + \operatorname{div}(\mathbf{v}_\nu W_\nu) = -\operatorname{div}(\mathbf{v}_\nu \nu k_B T_\nu) \mp q\nu\mathbf{v}_\nu \cdot \mathbf{E} + \operatorname{div}\,(\kappa_\nu \nabla T_\nu) + \left(\frac{\partial W_\nu}{\partial t}\right)_{coll} \tag{2.35c}$$

At this point we need to replace the collision terms with appropriate functions of the macroscopic variables.

2.2.9 Collision terms

Generation/recombination The collision term $\left(\frac{\partial \nu}{\partial t}\right)_{coll}$ accounts for particle generation/recombination mechanisms. In semiconductors it is an important term to be properly modeled (see [88, Chapter 4]). In the case of ion channels the above term is set to zero if no ions are absorbed or annihilated by the ion channel. Under this assumption we have:

$$\left(\frac{\partial \nu}{\partial t}\right)_{coll} \equiv 0. \tag{2.36}$$

Relaxation time approximation Recalling the notion of scattering rate $S(\mathbf{k}, \mathbf{k}')$ introduced in Section 2.1, we define the quantity $\tau(\mathbf{k})$ [70, 73]:

$$\frac{1}{\tau(\mathbf{k})} = \int_B S(\mathbf{k}, \mathbf{k}')\, d\mathbf{k}'. \tag{2.37}$$

It describes the average time between two consecutive collisions at $\mathbf{k}$. By assuming that all scattering processes are elastic, the collision term (2.7) can be approximated as:

$$C_{coll} \simeq \frac{f_\nu - f_{\nu 0}}{\tau} \tag{2.38}$$

where $f_{\nu 0}$ is the equilibrium distribution function. The physical motivation for the approximation (2.38) is as follows: suppose that at $t = 0$ all external forces are switched off (i.e.: $\mathbf{E} = \mathbf{0}$) and f_ν is homogeneous ($\nabla_{\mathbf{x}} f_\nu = \nabla_{\mathbf{k}} f_\nu = 0$). Thus, from (2.6) it follows that the distribution function may change as a result of collisions only. We get:

$$\begin{cases} \dfrac{\partial f_\nu}{\partial t} = -\dfrac{f_\nu - f_{\nu 0}}{\tau} \\ f_\nu(0) = f_0^\nu \end{cases} \tag{2.39}$$

The solution of this differential equation is

$$f_\nu = f_{\nu 0} + (f_0^\nu - f_{\nu 0})\, e^{-t/\tau} \tag{2.40}$$

so that the quantity τ represents the time required by the disturbed state to return to the state of equilibrium and for this reason it is called *relaxation time*.

Momentum and energy relaxation times Following [50, 31], we define the *momentum* relaxation time τ_{p_ν} via:

$$-\frac{\mathbf{p}_\nu}{\tau_{p_\nu}} = \left(\frac{\partial \mathbf{p}_\nu}{\partial t}\right)_{coll} \tag{2.41}$$

and the *energy* relaxation τ_{w_ν} time via:

$$-\frac{W_\nu - W^0}{\tau_{w_\nu}} = \left(\frac{\partial W_\nu}{\partial t}\right)_{coll} \tag{2.42}$$

where $W^0 = \frac{3}{2} k_B \nu T_0$ is the carrier energy at equilibrium, a situation in which $\mathbf{v}_\nu = \mathbf{0}$ and T_0 is a constant value representing the lattice temperature.

2.3 The Hydrodynamic model

2.3.1 Conservative form

We are finally able to write the *conservative* form of the *Hydrodynamic* (HD) model. By replacing the collision integrals with their relaxation-time approximations (2.36), (2.41), (2.42) equations (2.35a), (2.35b) and (2.35c) become:

$$\frac{\partial \nu}{\partial t} + \operatorname{div}(\nu \mathbf{v}_\nu) = 0 \tag{2.43a}$$

$$\frac{\partial \mathbf{p}_\nu}{\partial t} + \mathbf{div}(\mathbf{p}_\nu \otimes \mathbf{v}_\nu) = \mp q\nu\mathbf{E} - \nabla(\nu k_B T_\nu) - \frac{\mathbf{p}_\nu}{\tau_{p_\nu}} \tag{2.43b}$$

$$\frac{\partial W_\nu}{\partial t} + \operatorname{div}(\mathbf{v}_\nu W_\nu) = -\operatorname{div}(\mathbf{v}_\nu \nu k_B T_\nu) \mp q\nu\mathbf{v}_\nu \cdot \mathbf{E} + \operatorname{div}(\kappa_\nu \nabla T_\nu) - \frac{W_\nu - W^0}{\tau_{w_\nu}}. \tag{2.43c}$$

Equations (2.43) must be supplemented by the definitions (2.12) and (2.32). The Poisson equation must also be adjoined:

$$\begin{cases} \operatorname{div}(\epsilon\mathbf{E}) = q(p - n + N_{dop}) \\ \mathbf{E} = -\nabla\phi. \end{cases} \tag{2.44}$$

With respect to the carrier concentration ν, the momentum density $\mathbf{p}_\nu$ and the energy density w_ν, the HD system may be viewed as a second-order perturbation of a non-linear hyperbolic system of conservation laws, with an additional elliptic constraint represented by the Poisson equation (2.44). Due to its hyperbolic nature, the HD model in conservative form has to be solved numerically with appropriate methods, the most common being the *Discontinuous Galerkin* (DG) and *Essentially Non Oscillatory* (ENO) schemes [89, 90, 46]. For a brief introduction to DG methods we refer the reader to Appendix A.

Remark 2.2. The name "Hydrodynamic" comes from the similarity with the compressible Navier-Stokes equations of fluid mechanics (see, e.g., [78, Chapter 13]). The main differences are that in the present case: 1. moving particles are electrically charged; 2. the viscous effects in the stress tensor $\mathbf{P}_\nu$ have been neglected.
The complete viscous-hydrodynamic model for semiconductors was introduced in 1992 [2] and it has been numerically solved, e.g., in [7]. The HD model was originally proposed for semiconductors in 1970 [12].

2.3.2 Non conservative form

DG and ENO approximation schemes attack the numerical solution of the HD model in its conservative form in such a way that the unknowns of the system are $\nu, \mathbf{p}$ and w. A different approach, used for example in [71, 72, 42, 40, 6], adopts the non-conservative form of the HD system in order to apply the *box-integration* method, leading to a discretization scheme which generalizes the well known Scharfetter-Gummel method [85] to both the momentum- and energy -conservation equations.

Here, we report the HD system in the form presented in the cited bibliography, since part of our numerical methods are based on that formulation. The continuity equation (2.43a) is unchanged

$$\frac{\partial \nu}{\partial t} + \operatorname{div}(\nu \mathbf{v}_\nu) = 0 \tag{2.45}$$

while the momentum equation (2.43b) becomes

$$\mathbf{J}_\nu + \nu \tau_p \frac{d}{dt}\left(\frac{\mathbf{J}_\nu}{\nu}\right) = \pm q D_\nu \nabla \nu - q \mu_\nu \nu \nabla \left(\phi \mp \frac{k_B T_\nu}{q}\right) \tag{2.46}$$

and the energy equation (2.43c) becomes

$$\begin{cases} \dfrac{\partial(\nu w_\nu)}{\partial t} + \operatorname{div} \mathbf{S}_\nu = \mathbf{E} \cdot \mathbf{J}_\nu - \dfrac{\nu}{\tau_{w_\nu}}(w_\nu - w_\nu^0) \\ \mathbf{S}_\nu = -\kappa_\nu \nabla T_\nu \mp \dfrac{\mathbf{J}_\nu}{q}(w_\nu + k_B T_\nu) \end{cases} \tag{2.47}$$

where $\mathbf{S}_\nu$ is the carrier energy flow and $w_\nu^0 = W^0/\nu$.

New quantities of great importance have been introduced:

- **current density**
$$\mathbf{J}_\nu = \mp q \nu \mathbf{v}_\nu \tag{2.48}$$
- **mobility**
$$\mu_\nu = \frac{q}{m_\nu} \tau_{p_\nu} \tag{2.49}$$
- **diffusion coefficient** (generalized Einstein relation)
$$D_\nu = \mu_\nu \frac{k_B T_\nu}{q} = \frac{k_B T_\nu}{m_\nu} \tau_{p_\nu} \tag{2.50}$$

As usual, the Poisson equation must be adjoined.

Remark 2.3. The conservative and non conservative forms of the HD system reported in Sections 2.3.1 and 2.3.2 are completely equivalent. To see this, one can derive equation (2.46) from (2.43b) using equation (2.43a), the definitions of $\mathbf{p}, \mu_\nu$ and D_ν and noting that

$$\frac{d}{dt}(\cdot) = \frac{\partial(\cdot)}{\partial t} + \mathbf{v}_\nu \cdot \nabla_{\mathbf{x}}(\cdot).$$

Equation (2.47) is a simple reordering of (2.43c).

2.4 Hierarchy of models for charge transport

In this section we illustrate a hierarchy of physical models describing the motion of a binary mixture of monovalent ions (i.e.:$z = \pm 1$) in a medium, typically water. To keep the analogy with semiconductors, we will refer to the medium as "lattice", and it will be spotted by the symbol L.

The models are based on the HD system of Section 2.3.2. They are listed in decreasing order of complexity, from the Thermo-HD (THD) model, which adds an energy equation for the lattice, down to the simplest Drift Diffusion (DD) model, known as Poisson-Nernst-Planck (PNP) model in the theory of electrodiffusion of ions [81].

In each member of the hierarchy the Poisson equation must be adjoined:

$$\begin{cases} \operatorname{div}(\epsilon \mathbf{E}) = q(p - n + N_{dop}) \\ \mathbf{E} = -\nabla \phi. \end{cases} \tag{2.51}$$

We also remind that we have assumed $\left(\frac{\partial \nu}{\partial t}\right)_{coll} = 0$, see Section 2.2.9.

2.4.1 Thermal Hydrodynamic (THD) model

In this model the lattice is supposed not to be in thermal equilibrium with the carriers (energy exchanges can heat up the lattice) and so a heat flow equation for the lattice has to be solved. A new variable, the *lattice temperature* $T_L = T_L(\mathbf{x}, t)$, is introduced.

The lattice heat flow equation is derived in the same way as done for the carrier energy equation (2.35c) with the additional assumption that particles forming the lattice do not have a translational motion but only a vibrational motion, so that we can set their velocity $\mathbf{v}_L$ to zero. This assumption is commonly adopted for the quasi-particles called *phonons* in solid-state physics of semiconductor devices. In the case of biological channels, where

the electrolytic fluid (water) plays the role of lattice, the assumption $\mathbf{v}_L = \mathbf{0}$ amounts to neglecting the motion of liquid induced by an applied electric field (usually referred to as *electroosmosis*) with respect to the electro-thermo-chemical transport terms. For a detailed and quantitative analysis of this assumption see [101, 102] and references cited therein.

Under the previous assumption, equation (2.35c) in the case of lattice is:

$$\frac{\partial W_L}{\partial t} = \text{div } (\kappa_L \nabla T_L) + \left(\frac{\partial W_L}{\partial t}\right)_{coll} \tag{2.52}$$

where κ_L is the lattice thermoconductivity coefficient, and

$$W_L = \varrho_L c_L T_L \tag{2.53}$$

is the lattice *energy density*, ϱ_L and c_L being the lattice *specific mass density* and the lattice *specific heat*, respectively.

The collision term $\left(\frac{\partial W_L}{\partial t}\right)_{coll}$, which is the rate of change of W_L due to interactions with moving particles, satisfies the following closure relation [28]:

$$\left(\frac{\partial W_L}{\partial t}\right)_{coll} + \left(\frac{\partial W_p}{\partial t}\right)_{coll} + \left(\frac{\partial W_n}{\partial t}\right)_{coll} = 0. \tag{2.54}$$

Using (2.54) together with the energy relaxation time approximation (2.42), equation (2.52) becomes:

$$\frac{\partial W_L}{\partial t} - \text{div } (\kappa_L \nabla T_L) = \left[\frac{n}{\tau_{w_n}}(w_n - w_n^{eq}) + \frac{p}{\tau_{w_p}}(w_p - w_p^{eq})\right]. \tag{2.55}$$

The equations of the THD system are:

Charge conservation

$$\frac{\partial n}{\partial t} - \frac{1}{q}\text{div}\,\mathbf{J}_n = 0 \tag{2.56a}$$

$$\frac{\partial p}{\partial t} + \frac{1}{q}\text{div}\,\mathbf{J}_p = 0 \tag{2.56b}$$

Momentum conservation

$$\mathbf{J}_n + n\tau_{p_n}\frac{d}{dt}\left(\frac{\mathbf{J}_n}{n}\right) = qD_n\nabla n - q\mu_n n\nabla\left(\phi - \frac{k_B T_n}{q}\right) \tag{2.56c}$$

$$\mathbf{J}_p + p\tau_{p_p}\frac{d}{dt}\left(\frac{\mathbf{J}_p}{n}\right) = -qD_p\nabla p - q\mu_p p\nabla\left(\phi + \frac{k_B T_p}{q}\right) \tag{2.56d}$$

Energy conservation (carriers)

$$\begin{cases} \dfrac{\partial(nw_n)}{\partial t} + \operatorname{div}\mathbf{S}_n = \mathbf{E}\cdot\mathbf{J}_n - \dfrac{n}{\tau_{w_n}}(w_n - w_n^{eq}) \\ \mathbf{S}_n = -\kappa_n\nabla T_n - \dfrac{\mathbf{J}_n}{q}(w_n + k_B T_n) \end{cases} \tag{2.56e}$$

$$\begin{cases} \dfrac{\partial(pw_p)}{\partial t} + \operatorname{div}\mathbf{S}_p = \mathbf{E}\cdot\mathbf{J}_p - \dfrac{p}{\tau_{w_p}}(w_p - w_p^{eq}) \\ \mathbf{S}_p = -\kappa_p\nabla T_p + \dfrac{\mathbf{J}_p}{q}(w_p + k_B T_p) \end{cases} \tag{2.56f}$$

Energy conservation (lattice)

$$\begin{cases} \varrho_L c_L \dfrac{\partial T_L}{\partial t} + \operatorname{div}\mathbf{S}_L = \left[\dfrac{n}{\tau_{w_n}}(w_n - w_n^{eq}) + \dfrac{p}{\tau_{w_p}}(w_p - w_p^{eq})\right] \\ \mathbf{S}_L = -\kappa_L\nabla T_L \end{cases} \tag{2.57}$$

Remark 2.4. Rest energies w_n^{eq}, w_p^{eq} are no longer constant, since they refer now to $T_L \neq T_0 = const$, that is:

$$w_\nu^{eq} = \frac{3}{2}k_B T_L. \tag{2.58}$$

2.4.2 Hydrodynamic (HD) model

This model is nothing but the same as that illustrated in Section 2.3.2. It is reported here for sake of completeness.

Like the THD model, the HD model accounts for non-linear convective terms ($\frac{1}{2}m_\nu^*\mathbf{v}_\nu^2$ in the definition of w_ν and the material derivative $\frac{d}{dt}\left(\frac{\mathbf{J}_\nu}{\nu}\right)$ in the momentum balance equation), so that it can predict non-equilibrium phenomena like *velocity overshoot* which may appear when carriers experience a sudden variation of the electric field, either in space or time. When that happens, the carrier mean velocity $\mathbf{v}_\nu$ increases faster than the carrier temperature T_ν, thereby making the convective energy more important in a relative sense.

In this case, in contrast with the THD model, we suppose that the lattice evolves slowly with respect to carrier dynamics, so that one can set the lattice temperature T_L equal to a constant value, that is

$$T_L = T_0 = const. \tag{2.59}$$

In this picture, the lattice acts as an ideal heat-sink: carriers interact with it, but energy exchanges do not heat up the lattice (i.e., infinite thermal capacitance and null thermal resistance are assumed).

The equations of the HD system are:

Charge conservation

$$\frac{\partial n}{\partial t} - \frac{1}{q}\operatorname{div}\mathbf{J}_n = 0 \tag{2.60a}$$

$$\frac{\partial p}{\partial t} + \frac{1}{q}\operatorname{div}\mathbf{J}_p = 0 \tag{2.60b}$$

Momentum conservation

$$\mathbf{J}_n + n\tau_{p_n}\frac{d}{dt}\left(\frac{\mathbf{J}_n}{n}\right) = qD_n\nabla n - q\mu_n n\nabla\left(\phi - \frac{k_B T_n}{q}\right) \tag{2.60c}$$

$$\mathbf{J}_p + p\tau_{p_p}\frac{d}{dt}\left(\frac{\mathbf{J}_p}{n}\right) = -qD_p\nabla p - q\mu_p p\nabla\left(\phi + \frac{k_B T_p}{q}\right) \tag{2.60d}$$

Energy conservation

$$\begin{cases} \dfrac{\partial(nw_n)}{\partial t} + \operatorname{div}\mathbf{S}_n = \mathbf{E}\cdot\mathbf{J}_n - \dfrac{n}{\tau_{w_n}}(w_n - w_n^{eq}) \\ \mathbf{S}_n = -\kappa_n\nabla T_n - \dfrac{\mathbf{J}_n}{q}(w_n + k_B T_n) \end{cases} \tag{2.60e}$$

$$\begin{cases} \dfrac{\partial(pw_p)}{\partial t} + \operatorname{div}\mathbf{S}_p = \mathbf{E}\cdot\mathbf{J}_p - \dfrac{p}{\tau_{w_p}}(w_p - w_p^{eq}) \\ \mathbf{S}_p = -\kappa_p\nabla T_p + \dfrac{\mathbf{J}_p}{q}(w_p + k_B T_p) \end{cases} \tag{2.60f}$$

2.4.3 Electro-Thermal (ET) model

This model differs quite significantly from the previous two since some important simpliyfing assumptions are made.

Firstly, the material derivatives in the momentum conservation equation are neglected. This drastically reduces model complexity, making the numerical solution of the model much simpler to achieve.

Secondly, local equilibrium among holes, electrons and lattice is assumed, that is:

$$T_n = T_p = T_L =: T(\mathbf{x}, t). \tag{2.61}$$

This situation occurs when the system is assumed to have had enough time to evolve and to reach a steady state.

Finally, the kinetic part of the energy is considered to be small compared to the thermal one (i.e.: $\frac{1}{2}m_\nu^*|\mathbf{v}_\nu|^2 \ll \frac{3}{2}k_BT$), and thus we have

$$w_\nu \simeq \frac{3}{2}k_BT. \tag{2.62}$$

The resulting energy equations for anions, cations and lattice are, respectively:

$$\frac{\partial(nw_n)}{\partial t} + \operatorname{div}\left(-\kappa_n\nabla T - \frac{\mathbf{J}_n}{q}(w_n + k_BT)\right) = \mathbf{E}\cdot\mathbf{J}_n - \frac{n}{\tau_{w_n}}(w_n - w_n^{eq}) \tag{2.63a}$$

$$\frac{\partial(pw_p)}{\partial t} + \operatorname{div}\left(-\kappa_p\nabla T + \frac{\mathbf{J}_p}{q}(w_p + k_BT)\right) = \mathbf{E}\cdot\mathbf{J}_p - \frac{p}{\tau_{w_p}}(w_p - w_p^{eq}) \tag{2.63b}$$

$$\varrho_L c_L\frac{\partial T}{\partial t} + \operatorname{div}\left(-\kappa_L\nabla T_L\right) = \left[\frac{n}{\tau_{w_n}}(w_n - w_n^{eq}) + \frac{p}{\tau_{w_p}}(w_p - w_p^{eq})\right] \tag{2.63c}$$

Summing up the three energy equations one finds the energy equation for the total system:

$$\frac{\partial W_{tot}}{\partial t} + \operatorname{div}\left(-\kappa_{tot}\nabla T + \frac{5}{2}\frac{k_BT}{q}\left(\mathbf{J}_p - \mathbf{J}_n\right)\right) = \mathbf{E}\cdot\mathbf{J}_{tot} \tag{2.64}$$

where

$$W_{tot} := \left[\varrho_L c_L + \frac{3}{2}k_B(n+p)\right]T \tag{2.65}$$

is the system energy density, $\kappa_{tot} = \kappa_L + \kappa_n + \kappa_p$ and $\mathbf{J}_{tot} = \mathbf{J}_p + \mathbf{J}_n$.

The equations of the ET system are:

Charge conservation

$$\frac{\partial n}{\partial t} - \frac{1}{q}\operatorname{div}\mathbf{J}_n = 0 \tag{2.66a}$$

$$\frac{\partial p}{\partial t} + \frac{1}{q}\operatorname{div}\mathbf{J}_p = 0 \tag{2.66b}$$

Momentum conservation

$$\mathbf{J}_n = qD_n\nabla n - q\mu_n n\nabla\left(\phi - \frac{k_BT}{q}\right) \tag{2.66c}$$

$$\mathbf{J}_p = -qD_p\nabla p - q\mu_p p\nabla\left(\phi + \frac{k_BT}{q}\right) \tag{2.66d}$$

Energy conservation (total system)

$$\begin{cases} \dfrac{\partial W_{tot}}{\partial t} + \operatorname{div}\mathbf{S}_{tot} = \mathbf{E}\cdot\mathbf{J}_{tot} \\ \mathbf{S}_{tot} = -\kappa_{tot}\nabla T + \dfrac{5}{2}\dfrac{k_BT}{q}\left(\mathbf{J}_p - \mathbf{J}_n\right). \end{cases} \tag{2.66e}$$

Remark 2.5. The momentum conservation equations furnish now explicit expressions for the currents as a function of concentration, electric potential and temperature. This allows one to adopt the basic ideas of the Scharfetter-Gummel discretization method [85], which is the most widely used numerical scheme in contemporary semiconductor device simulation because of its stability and accuracy.

2.4.4 Drift Diffusion (DD) model

The simplest description of carrier transport is the *Drift-Diffusion* model. In addition to the simpliyfying assumptions of the Electro-Thermal model, the DD model forces both carrier temperatures to a constant value. This allows one to write the following equations:

Charge conservation

$$\frac{\partial n}{\partial t} - \frac{1}{q}\operatorname{div}\mathbf{J}_n = 0 \tag{2.67a}$$

$$\frac{\partial p}{\partial t} + \frac{1}{q}\operatorname{div}\mathbf{J}_p = 0 \tag{2.67b}$$

Momentum conservation

$$\mathbf{J}_n = qD_n\nabla n - q\mu_n n\nabla\phi \tag{2.67c}$$

$$\mathbf{J}_p = -qD_p\nabla p - q\mu_p p\nabla\phi. \tag{2.67d}$$

The condition of a constant temperature is consistently derived from the energy equation of the HD model in the following way. In fact, if we assume that the motion of carriers is damped instantaneously by frequent collisions

with the surrounding environment and that the energy transfer in this damping is small, the HD energy equation forces the temperature to a fixed value: after multiplying the energy equation (2.43c) by the energy-relaxation time τ_{w_ν}, thanks to the assumption of frequent collisions we can formally take the limit $\tau_{w_\nu} \to 0$ and get $T = T_0$.

In Biology, the expressions (2.67c) and (2.67d) are known as Nernst-Planck equations and their coupling with the Poisson equation results in the so-called Poisson-Nernst-Planck (PNP) model [8, 10, 18, 19], which is equivalent to the DD model just presented. A mathematical and numerical study of the one-dimensional steady-state PNP model can be found, e.g., in [75, 9, 86]. The interplay between particles and the electrolytic fluid was introduced for the first time in [81], resulting in the so-called *PNP-velocity-extended* model, which was subsequently analized, e.g., in [51, 53, 86, 69]. For recent applications of the PNP model, see [67, 52, 13].

Chapter 3

Functional Iterations for Charge Transport in Ion Channels

In this Chapter, we describe how to iteratively solve the mathematical models for charge transport introduced in Chapter 2. With this purpose we generalize to the present context the decoupled algorithm known as *Gummel* iteration that is widely adopted in semiconductor device simulation (see for a through presentation and analysis [50, 88, 70]). The use of the Gummel procedure allows to subdivide the system into blocks of single equations to be solved separately and in sequence until convergence is achieved. We treat the THD model, which is the most general member of the hierarchy illustrated in Chapter 2.

In Section 3.1 we state and discuss the three main assumptions at the base of our computations, namely 1. we deal only with *steady-state* and 2. *one-dimensional* computations, and 3. *nonlinear relations* from PNP model hold between concentrations and potential.

In Section 3.2 we report the THD model in scalar form and at steady-state, together with Dirichlet-type Boundary Conditions (BC).

In Section 3.3 we write Poisson equation in a nonlinear form, and we explain how to solve it by means of Newton's method.

Section 3.4 is devoted to the linearization of the momentum equation in order to obtain an explicit expression for the current.

In Section 3.5 we illustrate the *Gummel iterative* algorithm for the solution of the THD system.

In Section 3.6, we show that all the linearized equations of the THD system can be cast into a generic advection-diffusion-reaction model problem, which we address as Boundary Value Problem (BVP). The approximate solution of

the BVP by means of the Finite Element Method is illustrated in Chapter 4.

3.1 Assumptions

3.1.1 Steady-state conditions

In this work we limit our computations to the *steady-state* situation, i.e.:

$$\frac{\partial(\cdot)}{\partial t} \equiv 0. \tag{3.1}$$

This choice is motivated by the fact that our main purpose is the comparison of the I-V curves obtained adopting different physical models. When computing the I-V curves, one is interested in characterizing channel properties in static conditions and not during a transient period (the current that flows through the open channel can be studied independently of the gating process that opens it [83]). That is, we assume that the transmembrane potential generating the current flow in the channel is maintained constant for enough time to let the system reach a steady state.

3.1.2 One-dimensional geometry

We briefly explain the motivations that lead us to consider simulations in one spatial dimension only.

The PNP system neglects the heat generated by current flow, that is, the *temperature* (of ions and/or water) is not a variable of the system but it is held at a constant value. In [24], the authors used the HD model to study a one-dimensional ionic channel under a wide range of conditions. Results predicted possible substantial temperature changes in ion permeation, thus resulting in less current flow with a given transmembrane potential. In our work, we wish to further investigate these conclusions by simulating different types of channels and by including the effect of heat loss to water. At this level, the one dimensional setting seems the appropriate starting point for the validation and mutual comparison of the various models presented in the thesis.

For computational results performed with multidimensional PNP model and PNP-velocity-extended model on synthetic nanochannels, see, e.g., [54, 30, 101, 102].

3.1.3 Electrochemical potentials

In our computations, the solution of the Poisson equation relies on constitutive relations which express the concentrations n and p as exponential functions of the electric potential ϕ and of the electrochemical potentials ϕ_n and ϕ_p, namely:

$$n = N_{ref} \exp\left(\frac{\phi - \phi_n}{k_B T_n/q}\right) \tag{3.2a}$$

$$p = N_{ref} \exp\left(\frac{\phi_p - \phi}{k_B T_p/q}\right) \tag{3.2b}$$

where N_{ref} is a reference concentration to be specified (see Section 3.2.1). These relations are derived as follows.

From equations (2.67c), (2.67d) and using Einstein relation (2.50), we can readily write

$$\mathbf{J}_\nu = -q\mu_\nu\nu\left(\nabla\phi \mp V_{th0}\nabla \ln\left(\frac{\nu}{N_{ref}}\right)\right) \tag{3.3}$$

$$= -q\mu_\nu\nu\nabla\phi_\nu \tag{3.4}$$

where $V_{th0} := \dfrac{k_B T_0}{q}$ is the *thermal potential* and

$$\phi_\nu := \phi \mp V_{th0} \ln\left(\frac{\nu}{N_{ref}}\right) \tag{3.5}$$

is the *electrochemical potential*. Inverting (3.5) and generalizing to non constant temperatures T_n and T_p we recover expressions (3.2).

Remark 3.1. In semiconductor physics, relations (3.2) are known as Maxwell-Boltzmann statistics and potentials ϕ_n, ϕ_p as *quasi-Fermi levels*. Furthermore, the concentration N_{ref} assumes the physical meaning of intrinsic carrier concentration n_i in the semiconductor (see, e.g., [88, 70]).

3.2 Steady-state one-dimensional THD model

The THD system (2.56) and the Poisson equation (2.51) are rewritten here on the domain $\Omega = (0, L)$, at steady-state, together with Dirichlet-type boundary conditions:

Poisson equation

$$\begin{cases} \dfrac{\partial}{\partial x}(\epsilon E) = q(p - n + N_{dop}) \\ E = -\dfrac{\partial \phi}{\partial x} \end{cases} \tag{3.6a}$$

Charge conservation

$$\frac{1}{q}\frac{\partial J_n}{\partial x} = 0 \tag{3.6b}$$

$$\frac{1}{q}\frac{\partial J_p}{\partial x} = 0 \tag{3.6c}$$

Momentum conservation

$$J_n + n\tau_{p_n} v_n \frac{\partial}{\partial x}\left(\frac{J_n}{n}\right) = qD_n \frac{\partial n}{\partial x} - q\mu_n n \frac{\partial}{\partial x}\left(\phi - \frac{k_B T_n}{q}\right) \tag{3.6d}$$

$$J_p + p\tau_{p_p} v_p \frac{\partial}{\partial x}\left(\frac{J_p}{p}\right) = -qD_p \frac{\partial p}{\partial x} - q\mu_p p \frac{\partial}{\partial x}\left(\phi + \frac{k_B T_p}{q}\right) \tag{3.6e}$$

Energy conservation (carriers)

$$\begin{cases} \dfrac{\partial S_n}{\partial x} = EJ_n - \dfrac{n}{\tau_{w_n}}(w_n - w_n^{eq}) \\ S_n = -\kappa_n \dfrac{\partial T_n}{\partial x} - \dfrac{J_n}{q}(w_n + k_B T_n) \end{cases} \tag{3.6f}$$

$$\begin{cases} \dfrac{\partial S_p}{\partial x} = EJ_p - \dfrac{p}{\tau_{w_p}}(w_p - w_p^{eq}) \\ S_p = -\kappa_p \dfrac{\partial T_p}{\partial x} + \dfrac{J_p}{q}(w_p + k_B T_p) \end{cases} \tag{3.6g}$$

Energy conservation (lattice)

$$\begin{cases} \dfrac{\partial S_L}{\partial x} = \left[\dfrac{n}{\tau_{w_n}}(w_n - w_n^{eq}) + \dfrac{p}{\tau_{w_p}}(w_p - w_p^{eq})\right] \\ S_L = -\kappa_L \nabla T_L \end{cases} \tag{3.6h}$$

Boundary Conditions

$$\begin{cases} \phi(0) = \phi_0, & \phi(L) = \phi_L; \\ n(0) = n_0, & n(L) = n_L; \\ p(0) = p_0, & p(L) = p_L; \\ T_n(0) = T_{n0}, & T_n(L) = T_{nL}; \\ T_p(0) = T_{p0}, & T_p(L) = T_{pL}; \\ T_L(0) = T_{L0}, & T_L(L) = T_{LL}. \end{cases} \tag{3.6i}$$

3.2.1 Boundary conditions

In this section we show how to derive Dirichlet boundary conditions from experimental set up. Figure 3.1 illustrates the scheme of a generic ion channel connected with two reservoirs (also called baths) $\mathtt{L}$ and $\mathtt{R}$, which are supposed to be in thermodynamical equilibrium: potential is held at an externally applied bias $\overline{V}_{\mathtt{L}}, \overline{V}_{\mathtt{R}}$, ions have equal and constant concentrations $C_{\mathtt{L}} := \bar{p}_{\mathtt{L}} = \bar{n}_{\mathtt{L}}$, $C_{\mathtt{R}} := \bar{p}_{\mathtt{R}} = \bar{n}_{\mathtt{R}}$ (so that there is no net charge being $N_{dop} \equiv 0$ in the baths) and temperatures are fixed to $\overline{T}_{\mathtt{L}}, \overline{T}_{\mathtt{R}}$. Thermodynamical equilibrium and charge neutrality are assumed at the end points of the channel (i.e.: at $x = 0$ and at $x = L$).

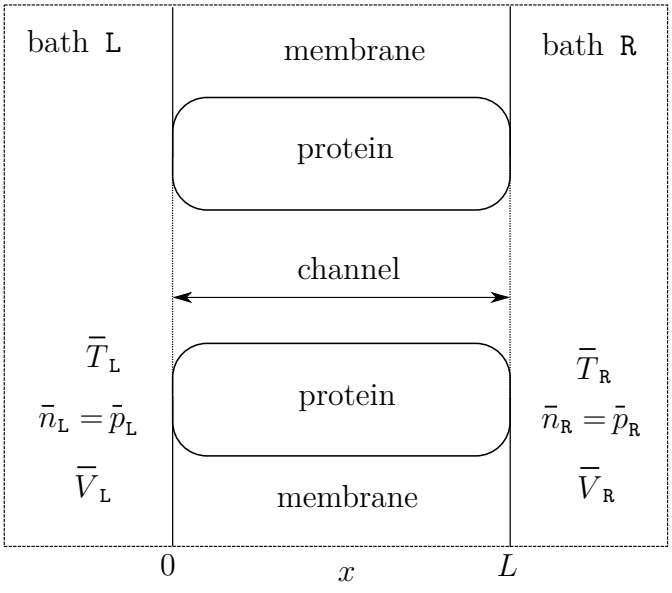

Figure 3.1: Schematic view of a protein channel embedded in a membrane that separates the two baths. Each bath has constant temperature, potential and concentrations. The channel extends from $x = 0$ to $x = L$.

Temperature Boundary conditions for temperatures are set as:

$$T_{n0} = T_{p0} = T_{L0} = \overline{T}_{\mathtt{L}} \tag{3.7a}$$

$$T_{nL} = T_{pL} = T_{LL} = \overline{T}_{\mathtt{R}} \tag{3.7b}$$

which express an instantaneous thermalization of ions with the two reservoirs.

Concentration To determine boundary conditions for potential and concentrations, we follow the treatment of the built-in potential in a metal-semiconductor junction [88, 70], which has been already used in biological channels (see, e.g., [19, 20]).

Local thermal equilibrium implies the existence of a unique electrochemical potential at the channel ends, which, for convenience, is fixed equal to the externally applied voltage:

$$\phi_n(0) = \phi_p(0) = \overline{V}_{\mathtt{L}} \tag{3.8a}$$

$$\phi_n(L) = \phi_p(L) = \overline{V}_{\mathtt{R}} \tag{3.8b}$$

so that from relations (3.2) we have

$$n(0) = N_{ref} \exp\left(\frac{\phi(0) - \overline{V}_{\mathtt{L}}}{k_B \overline{T}_{\mathtt{L}}/q}\right) \tag{3.9a}$$

$$p(0) = N_{ref} \exp\left(\frac{\overline{V}_{\mathtt{L}} - \phi(0)}{k_B \overline{T}_{\mathtt{L}}/q}\right) \tag{3.9b}$$

and

$$n(L) = N_{ref} \exp\left(\frac{\phi(L) - \overline{V}_{\mathtt{R}}}{k_B \overline{T}_{\mathtt{R}}/q}\right) \tag{3.10a}$$

$$p(L) = N_{ref} \exp\left(\frac{\overline{V}_{\mathtt{R}} - \phi(L)}{k_B \overline{T}_{\mathtt{R}}/q}\right). \tag{3.10b}$$

In order to properly set boundary conditions that account for different bulk concentrations, N_{ref} must assume the value $C_{\mathtt{L}}$ at $x = 0$ and $C_{\mathtt{R}}$ at $x = L$. We thus assume $N_{ref} = N_{ref}(x)$ to be a linear function of the position x, such that $N_{ref}(0) = C_{\mathtt{L}}$ and $N_{ref}(L) = C_{\mathtt{R}}$. This is the expression for N_{ref} to be used in realations (3.2). With this latter assumption, from (3.9) and (3.10) we get

$$n(0)p(0) = C_{\mathtt{L}}^2 \tag{3.11a}$$

$$n(L)p(L) = C_{\mathtt{R}}^2. \tag{3.11b}$$

The assumption of charge neutrality implies the conditions:

$$p(0) - n(0) + N_{dop}(0) = 0 \tag{3.12a}$$
$$p(L) - n(L) + N_{dop}(L) = 0. \tag{3.12b}$$

Together, (3.11a) and (3.12) imply

$$n(0) = \frac{\sqrt{N_{dop}^2(0) + 4C_{\mathtt{L}}^2} + N_{dop}(0)}{2} \quad n(L) = \frac{\sqrt{N_{dop}^2(L) + 4C_{\mathtt{R}}^2} + N_{dop}(L)}{2} \tag{3.13a}$$

$$p(0) = \frac{\sqrt{N_{dop}(0)^2 + 4C_{\mathtt{L}}^2} - N_{dop}(0)}{2} \quad p(L) = \frac{\sqrt{N_{dop}(L)^2 + 4C_{\mathtt{R}}^2} - N_{dop}(L)}{2} \tag{3.13b}$$

which show that concentrations at the boundaries are determined by the local doping profile N_{dop} and the bulk concentrations $C_{\mathtt{L}}$, $C_{\mathtt{R}}$.

Potential From relations (3.9),(3.10), we can see that the potential within the channel is not equal to the applied potential but is rather offset by the *built-in potential* V_{bi} (called *Donnan potential* in biology):

$$\phi(0) = \overline{V}_{\mathtt{L}} + V_{bi}(0) \tag{3.14a}$$
$$\phi(L) = \overline{V}_{\mathtt{R}} + V_{bi}(L) \tag{3.14b}$$

where

$$V_{bi}(0) := \frac{k_B \overline{T}_{\mathtt{L}}}{q} \ln\left(\frac{n(0)}{C_{\mathtt{L}}}\right) = -\frac{k_B \overline{T}_{\mathtt{L}}}{q} \ln\left(\frac{p(0)}{C_{\mathtt{L}}}\right) \tag{3.15a}$$
$$V_{bi}(L) := \frac{k_B \overline{T}_{\mathtt{R}}}{q} \ln\left(\frac{n(L)}{C_{\mathtt{R}}}\right) = -\frac{k_B \overline{T}_{\mathtt{R}}}{q} \ln\left(\frac{p(L)}{C_{\mathtt{R}}}\right). \tag{3.15b}$$

3.3 Nonlinear Poisson (NLP) equation

By substituting relations (3.2) into the Poisson equation (3.6a), and incorporating boundary conditions (3.6i), we get:

$$-\epsilon \frac{\partial^2 \phi}{\partial x^2} = q\left[N_{ref} \exp\left(\frac{\phi_p - \phi}{k_B T_p/q}\right) - N_{ref} \exp\left(\frac{\phi - \phi_n}{k_B T_n/q}\right) + N_{dop}\right] \quad \text{in } \Omega \tag{3.16a}$$

$$\phi(0) = \phi_0, \qquad \phi(L) = \phi_L \tag{3.16b}$$

where we have supposed ϵ to be constant. Equation (3.16) is a nonlinear equation with respect to ϕ, and so it will be addressed as *Nonlinear Poisson* (NLP) equation.

3.3.1 The abstract Newton method

In this section, we introduce the Newton method in the abstract setting of nonlinear differential operators. We refer to Appendix B for the required notation and tools in Functional Analysis that are used in the discussion below.

Let V be a Banach space endowed with the norm $\|\cdot\|_V$. We consider the nonlinear differential operator $F : V \to V$ and the associated problem: find $U \in V$ such that

$$F(U) = 0. \tag{3.17}$$

The Abstract Newton Method for the iterative solution of problem (3.17) reads: given $U^{(0)} \in V$, for all $j \geq 0$ until convergence, solve the following *linearized* problem

$$F'(U^{(j)})\delta U^{(j)} = -F(U^{(j)}) \tag{3.18a}$$

$$U^{(j+1)} = U^{(j)} + \delta U^{(j)}. \tag{3.18b}$$

The following result tells us that, provided to start sufficiently close to the zero of F, the Newton method converges quadratically.

Theorem 3.1 (Local convergence for the Newton Method)**.** *Let $U \in V$ be a solution of problem* (3.17)*. Assume that F' is Lipschitz continuous in the ball $B(U;\varepsilon)$, i.e., that there exists $K > 0$ such that*

$$||F'(v) - F'(z)||_{L(V;V)} \leq K||v - z||_V \qquad \forall\, v, z \in B(U;\varepsilon), \quad v \neq z. \tag{3.19}$$

Then, there exists in correspondance $\varepsilon' > 0$, with $\varepsilon' \leq \varepsilon$, such that for all $U^{(0)} \in B(U;\varepsilon')$ the sequence $\left\{U^{(j)}\right\}$ generated by (3.18) *converges quadratically to U, i.e., there exists $C > 0$ such that, for a suitable $j_0 \geq 0$, we have*

$$||U - U^{(j+1)}||_V \leq C||U - U^{(j)}||_V^2 \qquad \forall\, j \geq j_0. \tag{3.20}$$

For a theoretical convergence of Newton's method at the operator level see [105, Ch.5].

3.3.2 Functional iteration

To treat the nonlinear character of the Poisson equation (3.16), we use the Newton iterative process (3.18) with the following identifications:

$$U := \phi \tag{3.21a}$$

$$F(\phi) := -\epsilon\frac{\partial^2\phi}{\partial x^2} - q\left[N_{ref}\exp\left(\frac{\phi_p-\phi}{k_BT_p/q}\right) - N_{ref}\exp\left(\frac{\phi-\phi_n}{k_BT_n/q}\right) + N_{dop}\right] \tag{3.21b}$$

From definition (B.4) one can compute the Fréchet derivative of F to obtain:

$$F'(\phi)\delta\phi = -\epsilon\frac{\partial^2\delta\phi}{\partial x^2} + \frac{qN_{ref}}{V_{th0}}\left[\frac{T_0}{T_p}\exp\left(\frac{\phi_p-\phi}{k_BT_p/q}\right) + \frac{T_0}{T_n}\exp\left(\frac{\phi-\phi_n}{k_BT_n/q}\right)\right]\delta\phi. \tag{3.22}$$

where ϕ is a function of $H^1(0,L)$ satisfying the first two boundary conditions in (3.6i) and $\delta\phi$ is an arbitrary function belonging to $V := H_0^1(0,L)$.

Then, given $\phi^{(0)}$, at each step $j \geq 0$ until convergence, we have to solve the following *linear* problem:

$$-\epsilon\frac{\partial^2\delta\phi}{\partial x^2} + \frac{qN_{ref}}{V_{th0}}\left[\frac{T_0}{T_p}\exp\left(\frac{\phi_p-\phi}{k_BT_p/q}\right) + \frac{T_0}{T_n}\exp\left(\frac{\phi-\phi_n}{k_BT_n/q}\right)\right]\delta\phi = -F(\phi^{(j)}) \qquad \text{in } \Omega = (0,L) \tag{3.23a}$$

$$\delta\phi(0) = \delta\phi(L) = 0. \tag{3.23b}$$

and then set

$$\phi^{(j+1)} = \phi^{(j)} + \theta_j\delta\phi \tag{3.24}$$

where θ_j is a *damping* parameter, suitably chosen in the interval $(0,1]$, introduced to avoid excessively large increments between consecutive Newton steps, particularly during the very first iterations where the available iterate $\phi^{(j)}$ may be quite far from the exact solution (see [88, Chapter 7]).

3.4 Linearization of the momentum equation

We want to linearize the momentum equations (3.6d) and (3.6e) with the purpose of finding an explicit expression for the current J_ν. We follow the approach proposed in [71, 72].

We first rewrite equations (3.6d) and (3.6e) (after some manipulation) into the form:

$$J_\nu \mp \frac{\tau_{p_\nu}}{q} J_\nu \frac{\partial}{\partial x}\left(\frac{J_\nu}{\nu}\right) = \pm q\overline{D}_\nu \left[\widehat{T}_\nu \frac{\partial \nu}{\partial x} + \nu \frac{\partial}{\partial x}\left(\widehat{T}_\nu \mp \widehat{\phi}\right)\right] \tag{3.25}$$

where

$$\overline{D}_\nu := \mu_\nu \frac{k_B T_0}{q}$$

and

$$\widehat{T}_\nu := \frac{T_\nu}{T_0}, \qquad \widehat{\phi} := \frac{\phi}{k_B T_0/q}$$

are the dimensionless temperature and electric potential, respectively. From equations (3.6b) and (3.6c), we deduce that J_ν is constant in Ω. Denoting by $\overline{J_\nu}$ the value of such a constant, equation (3.25) becomes:

$$\overline{J_\nu}\left[1 \mp \frac{\tau_{p_\nu}}{q} J_\nu \frac{\partial}{\partial x}\left(\frac{1}{\nu}\right)\right] = \pm q\overline{D}_\nu \left[\widehat{T}_\nu \frac{\partial \nu}{\partial x} + \nu \frac{\partial}{\partial x}\left(\widehat{T}_\nu \mp \widehat{\phi}\right)\right]. \tag{3.26}$$

Even if we assume that $\widehat{\phi}$ and $\widehat{T}_\nu$ are known, the latter equation is still nonlinear in the concentration ν. To overcome this difficulty, we treat the nonlinear dependence in an iteratively fashion. Suppose that we are at the k-th step of an iterative procedure, we define the quantity

$$\lambda_\nu := \frac{\tau_{p_\nu}}{q} \overline{J_\nu}^{(k-1)} \frac{\partial}{\partial x}\left(\frac{1}{\nu^{(k-1)}}\right) \tag{3.27}$$

which is known from the previous iteration. Using (3.27) into (3.26), we get an explicit expression for $\overline{J_\nu}$ in terms of the variables $\widehat{T}_\nu, \nu$ and $\widehat{\phi}$:

$$\overline{J_\nu} = \pm \frac{q\overline{D}_\nu}{1 \mp \lambda_\nu}\left[\widehat{T}_\nu \frac{\partial \nu}{\partial x} + \nu \frac{\partial}{\partial x}\left(\widehat{T}_\nu \mp \widehat{\phi}\right)\right]. \tag{3.28}$$

Remark 3.2. The coefficient λ_ν accounts for the convective terms by a modification of the diffusion coefficient. If one forces λ_ν to zero, the contribution of the convective terms is removed from the model.

Remark 3.3. In [72], it is proved that, for $\overline{J_\nu}$ to be real, a necessary condition is

$$|\lambda_\nu| \leq \frac{1}{2}. \tag{3.29}$$

Equation (3.29) can be used to monitor an unphysical behaviour which may be exhibited by λ_ν, typically at the beginning of an iterative solution procedure.

3.5 Gummel iteration for the THD system

The THD system (3.6) can be solved using a decoupled iterative algorithm, known as *Gummel iteration* [43]. This latter method consists in a nonlinear block Gauss-Seidel iteration on the system because each of the PDE's constituting the overall problem is solved successively until a self-consistency among the various blocks is reached. In this event, the algorithm is said to converge.

The Gummel algorithm starts with an *initial guess* $(\phi^0, \phi_p^0, \phi_n^0, T_p^0, T_n^0, T_L^0)$ for the dependent variables that satisfies the boundary conditions (3.6i) and (3.8). The generic k-th step of the algorithm reads:

1. solve NLP equation (3.16) (with Newton's method, see Section 3.3.2) in order to obtain an updated potential ϕ^{k+1};

2. solve the continuity equations (3.6b) and (3.6c) supplied with the generalized expressions of the currents (3.28) in order to obtain the updated concentrations p^{k+1}, n^{k+1};

3. compute the currents J_ν^{k+1} and the drift velocities v_ν^{k+1};

4. solve the energy equations (3.6f) and (3.6g) in order to obtain the updated temperatures T_p^{k+1}, T_n^{k+1};

5. solve the lattice energy equation (3.6h), in order to obtain the updated lattice temperature T_L^{k+1};

6. update the electrochemical potentials

$$\phi_n^{k+1} = \phi^{k+1} - \frac{k_B T_n^{k+1}}{q} \ln\left(\frac{n^{k+1}}{N_{ref}}\right) \tag{3.30a}$$

$$\phi_p^{k+1} = \phi^{k+1} + \frac{k_B T_p^{k+1}}{q} \ln\left(\frac{p^{k+1}}{N_{ref}}\right) \tag{3.30b}$$

7. check the convergence of the iteration by controlling whether the maximum absolute difference between two consecutive iterations k and $k+1$ is less than a prescribed tolerance

$$\max_{\eta \in U} ||\eta^{k+1} - \eta^k||_\infty < toll. \tag{3.31}$$

where U is the set of unknowns $(\phi, \phi_p, \phi_n, T_p, T_n, T_L)^T$. If condition (3.31) is satisfied, the algorithm stops.

A flow chart of the Gummel procedure for the THD model is shown in Figure 3.2.

Remark 3.4. The momentum balance equations do not appear explicitly in the algorithm 1. – 7. because they are used as constitutive relations in order to express the current J_ν in terms of concentrations and potentials (cf. (3.28)).

Theory of Gummel iterative procedure The mathematical analysis of the convergence of the Gummel decoupling algorithm for the stationary DD model of semiconductors can be found in [50].

The Gummel map is a *fixed point* iteration of the form $z \mapsto T(z)$, arising from the coupled elliptic DD system, and it consists of a nonlinear block Gauss-Seidel iteration on the system. The fixed point $\phi^* = T(\phi^*)$ corresponds to a *simultaneous* solution of the DD system. Existence of a fixed point of the mapping T follows from the maximum principle and Schauder's fixed point theorem. In [58] it is shown that a nonlinear version of the GMRES method provides an effective means of accelerating the speed of convergence of the nonlinear fixed point map T. In the latter reference, the pivotal role of the solution of the NLP equation in performing as a "natural" preconditioner of the GMRES method is also highlighted.

3.6 Unified framework for THD model

All the linearized equations of the THD system (3.6) that need to be solved during the iterative procedure described in Section 3.5 can be cast into the following generic Boundary Value model Problem (BVP) with advection, diffusion and reaction phenomena:

find $u \in H^1(\Omega)$ such that:

$$\begin{cases} \dfrac{\partial}{\partial x}\left(vu - D\dfrac{\partial u}{\partial x}\right) + cu = g & \text{in } \Omega \\ u = \overline{u_0} & \text{at } x = 0 \\ u = \overline{u_L} & \text{at } x = L \end{cases} \tag{3.32}$$

Table 3.1 specifies how to choose the coefficients v, D, c and g for each equation of the linearized THD system (3.6) in the Gummel algorithm of Figure 3.2.

Figure 3.2: Gummel iteration flow chart for the steady-state THD model.

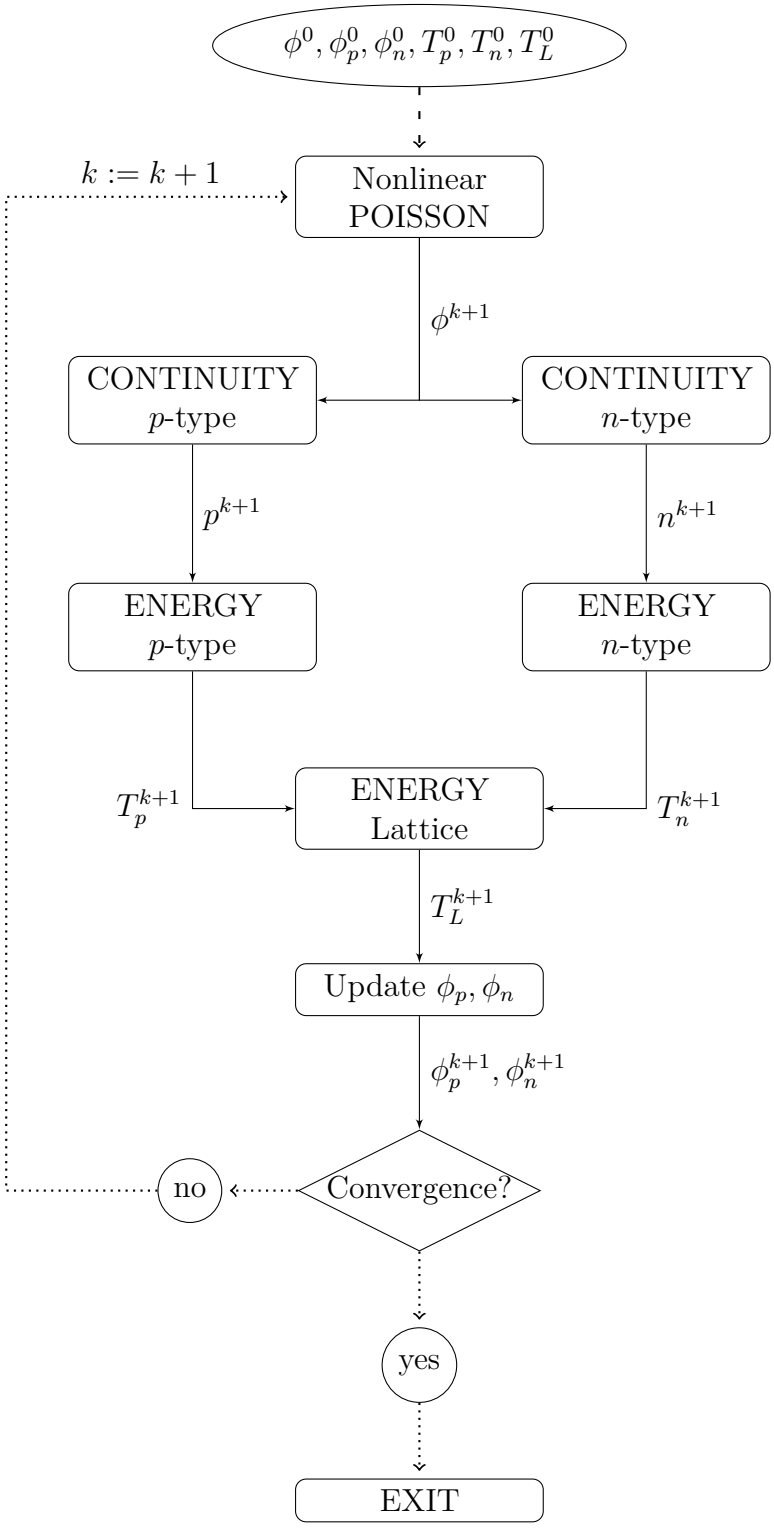

Table 3.1: Expressions of the coefficients v, D, c, g of the BVP (3.32) for each equation of the linearized THD system. The unknown u and boundary conditions $\overline{u_0}, \overline{u_L}$ are also specified.

Symbol	**Equation**			
	(3.23a)	(3.6b), (3.6c)	(3.6f), (3.6g)	(3.6h)
u	$\delta\phi$	ν	T_ν	T_L
v	0	$\pm\frac{q\overline{D}_\nu}{1\mp\lambda_\nu}\frac{\partial}{\partial x}\left(\widehat{T}_\nu \mp \widehat{\phi}\right)$	$\mp\frac{5}{2}\frac{J_\nu}{q}k_B$	0
D	ϵ	$\mp\frac{q\overline{D}_\nu}{1\mp\lambda_\nu}\widehat{T}_\nu$	κ_ν	κ_L
c	$\frac{q}{V_{th0}}\left(\frac{T_0}{T_n}n + \frac{T_0}{T_p}p\right)$	0	$\frac{3}{2}\nu\frac{k_B}{\tau_{w_\nu}}$	$\frac{3}{2}k_B\left(\frac{n}{\tau_{w_n}} + \frac{p}{\tau_{w_p}}\right)$
g	$\frac{\partial^2}{\partial x^2}(\epsilon\phi) + q(p - n + N_{dop})$	0	$\pm\frac{J_\nu}{q}\frac{m}{2}\frac{\partial}{\partial x}(v_\nu^2) + EJ_\nu - \frac{1}{2}\frac{\nu}{\tau_{w_\nu}}(mv_\nu^2 - 3k_BT_0)$	$\frac{3}{2}k_B\left(\frac{nT_n}{\tau_{w_n}} + \frac{pT_p}{\tau_{w_p}}\right)$
$\overline{u_0}$	0	ν_0	$T_{\nu 0}$	T_{L0}
$\overline{u_L}$	0	ν_L	$T_{\nu L}$	T_{LL}

Chapter 4

Finite Element Approximation

In this Chapter we deal with the numerical solution of the model BVP (3.32) using the Finite Element Method (FEM).

Sections 4.1 and 4.2 introduce the geometrical discretization of the problem and the associated finite element spaces of the approximation scheme we use, which is the Dual-Mixed-Hybridized method (DMH). In Section 4.3 we start with the basic Dual-Mixed method (DM) describing in detail how to construct the associated linear algebraic system. We conclude the section by highlighting some critical aspects of the DM method which make the adoption of the scheme computationally expensive. In Section 4.4, in order to overcome such limitations, we introduce the Hybridized version of the DM method, denoted by DMH, that is the scheme used in all numerical experiments conducted in this thesis.

The origin and motivation of Mixed and Hybrid methodologies is to be found in the field of structural engineering in the pioneering works [98, 76] whose mathematical analysis has given rise to the modern theory of saddle-point problems in the fundamental works [5, 14, 74].

4.1 Finite Element spaces

Mesh We denote by Ω the open interval $(0, L)$ and by $\partial\Omega = \{0, L\}$ its boundary on which an outward unit normal $\mathbf{n}$ is defined, in such a way that $\mathbf{n}(0) = -1$ and $\mathbf{n}(L) = +1$ (see Figure 4.1).

We introduce a partition $\mathcal{T}_h$ of $\overline{\Omega}$ into a number $M \geq 2$ of intervals $K_i = [x_i, x_{i+1}], i = 1, \ldots, M$, with $x_1 = 0$ and $x_{M+1} = L$. We denote by $h_i := x_{i+1} - x_i$ the length of each interval and set the *mesh size* $h := \max_{\mathcal{T}_h} h_i$. The partition $\mathcal{T}_h$ takes the name of *triangulation* of the domain Ω. Each K_i is an *element* of the triangulation, while the quantities x_i, $i = 1, \ldots, N$ are

Figure 4.1: Computational domain in 1D.

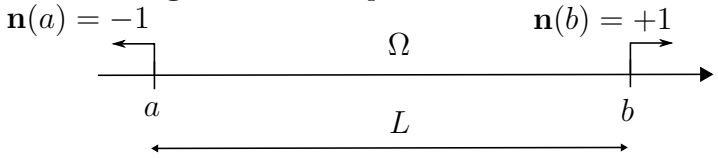

the *vertices* of the triangulation, having set $N := M + 1$. We denote with $\mathcal{N}_h := \{x_i\}_{i=1}^N$ the set of vertices of $\mathcal{T}_h$.

Discrete spaces We associate with $\mathcal{T}_h$ the following pair of function spaces:

$$V_h := \{w_h \in L^2(\Omega) \text{ s.t. } w_h|_K \in \mathbb{P}_0(K) \, \forall K \in \mathcal{T}_h\} \tag{4.1a}$$

$$Q_h := \{q_h \in C^0(\bar{\Omega}) \text{ s.t. } q_h|_K \in \mathbb{P}_1(K) \, \forall K \in \mathcal{T}_h\} \tag{4.1b}$$

V_h is the vector space of piecewise constant polynomials defined over Ω, Q_h is the vector space of piecewise linear continuous polynomials over $\bar{\Omega}$. The dimension of V_h is simply equal to the number of elements M, while the dimension of Q_h is equal to the number of vertices $N = M + 1$. Figure 4.2 shows an example of $\mathcal{T}_h$ (with $M = 5$) and of functions $w_h \in V_h$ and $q_h \in Q_h$.

4.2 Basis functions

Any function $q_h \in Q_h$, and $w_h \in V_h$ can be written in the form:

$$q_h(x) = \sum_{j=1}^{N} q_j \psi_j(x) \tag{4.2a}$$

$$w_h(x) = \sum_{k=1}^{M} w_k \varphi_k(x) \tag{4.2b}$$

where ψ_j, $j = 1, \ldots, N$ and φ_k, $k = 1, \ldots, M$ are the basis functions of Q_h and V_h. The real numbers q_j and w_k are the *degrees of freedom* of q_h, and w_h.

Lagrangian bases For the basis of Q_h we choose the piecewise linear continuous *Lagrangian basis functions* $\psi_i(x)$, such that:

$$\psi_i(x_j) = \delta_{ij} \quad i, j = 1, \ldots, N. \tag{4.3}$$

Figure 4.2: Triangulation in 1D and finite element functions. Black ticks (|) denote nodal values, while black squares (■) and black bullets (•) are the spatial positions of the degrees of freedom of V_h and Q_h, respectively.

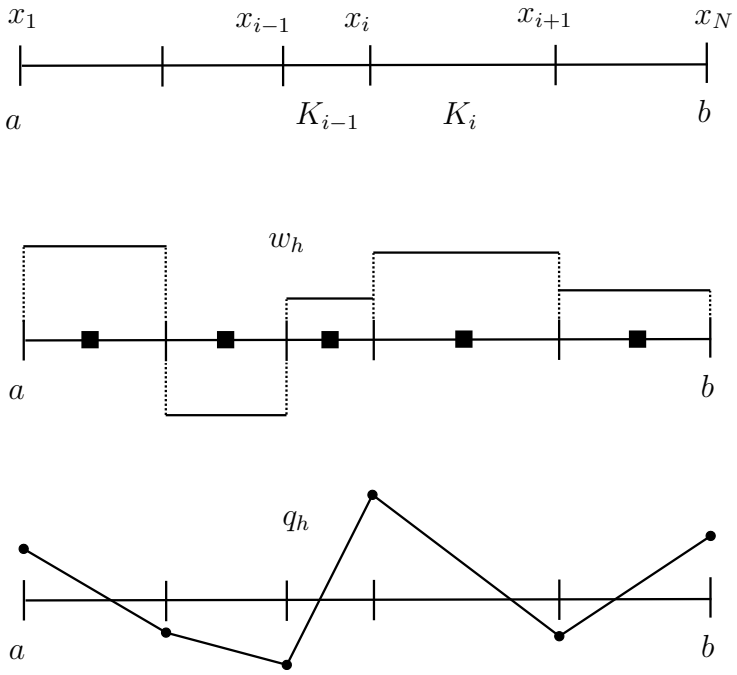

With this property the quantities q_i can be interpreted as the nodal values of q_h at the grid nodes, i.e.:

$$q_h(x_i) = q_i \quad i = 1, \ldots, N. \tag{4.4}$$

The Lagrangian property in the case of the basis functions of V_h simply consists of taking

$$\varphi_k(x) = \chi_k(x) = \begin{cases} 1 & \text{if } x \in K_k \\ 0 & \text{elsewhere} \end{cases} \tag{4.5}$$

with $k = 1, \ldots, M$. With this definition, the quantities w_k can be interpreted as the nodal value of $w_h(x)$ at the midpoint of each element K_k, $k = 1, \ldots, M$. Functions $\psi_i(x)$ and $\varphi_k(x)$ are represented in Figure 4.3.

Figure 4.3: The Lagrangian basis functions ψ_i and φ_k.

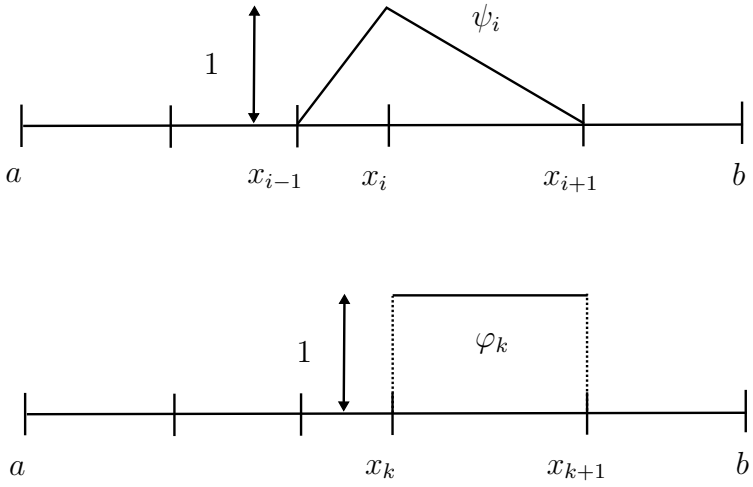

4.3 Dual Mixed (DM) method

We rewrite the equations of the BVP (3.32) in mixed form:

$$\begin{cases} \dfrac{\partial J}{\partial x} + cu = g & \text{in } \Omega \quad (4.6a) \\ J = vu - D\dfrac{\partial u}{\partial x} & \text{in } \Omega \quad (4.6b) \\ u = f & \text{on } \partial\Omega \quad (4.6c) \end{cases}$$

In the dual mixed method, the variables u and J in (4.6) are treated as independent unknowns, each of which belongs to a different functional space, namely $u \in V := L^2(\Omega)$ and $J \in Q := H(\mathrm{div}, \Omega) \equiv H^1(\Omega)$ in the one dimensional case considered in the present chapter. Then, we proceed formally by multiplying equation (4.6a) by a test function $w \in V$ and equation (4.6b) by a test function $q \in Q$, and integrate by parts over Ω to obtain the problem:

find $(u, J) \in V \times Q$ such that, for all $(w, q) \in V \times Q$:

$$\begin{cases} \displaystyle\int_\Omega D^{-1}\,(J - vu)\,q\,dx - \int_\Omega u\frac{\partial q}{\partial x}\,dx = -\int_{\partial\Omega}(q\cdot\mathbf{n})f\,d\sigma & \text{(4.7a)} \\ \displaystyle -\int_\Omega \frac{\partial J}{\partial x}w\,dx - \int_\Omega cuw\,dx = -\int_\Omega gw\,dx & \text{(4.7b)} \end{cases}$$

Existence and uniqueness of the solution pair (u, J) of problem (4.7) can be proved under suitable coercivity assumptions, see [36].

4.3.1 Finite Element formulation

The Dual-Mixed FE approximation of problem (4.7) reads:

find $(u_h, J_h) \in V_h \times Q_h$ such that, for all $(w_h, q_h) \in V_h \times Q_h$:

$$\begin{cases} \displaystyle\int_\Omega D^{-1}\,(J_h - vu_h)\,q_h\,dx - \int_\Omega u_h\frac{\partial q_h}{\partial x}\,dx = -\int_{\partial\Omega}(q_h\cdot\mathbf{n})f\,d\sigma & \text{(4.8a)} \\ \displaystyle -\int_\Omega \frac{\partial J_h}{\partial x}w_h\,dx - \int_\Omega cu_hw_h\,dx = -\int_\Omega gw_h\,dx & \text{(4.8b)} \end{cases}$$

Again, we refer to [36] for the proof of existence and uniqueness of the solution pair (u_h, J_h) of (4.8). By definition of basis of a vector space, we write u_h and J_h using the expansions (4.2):

$$u_h(x) = \sum_{k=1}^{M} u_k\varphi_k(x) \tag{4.9a}$$

$$J_h(x) = \sum_{j=1}^{N} J_j\psi_j(x) \tag{4.9b}$$

so that system (4.8) becomes:

$$\begin{aligned} \sum_{j=1}^{N} J_j\int_\Omega D^{-1}\psi_j\psi_i - \sum_{k=1}^{M} u_k\int_\Omega D^{-1}v\varphi_k\psi_i\,dx - \sum_{k=1}^{M} u_k\int_\Omega \varphi_k\frac{\partial\psi_i}{\partial x}\,dx \\ = -\int_{\partial\Omega}(\psi_i\cdot\mathbf{n})f\,d\sigma \quad i = 1,\ldots,N. \end{aligned} \tag{4.10a}$$

$$-\sum_{j=1}^{N} J_j \int_\Omega \frac{\partial \psi_j}{\partial x}\varphi_k \, dx - \sum_{l=1}^{M} u_l \int_\Omega c\varphi_l\varphi_k \, dx = -\int_\Omega g\varphi_k \, dx \quad k = 1, \ldots, M \tag{4.10b}$$

The boundary integral can be written explicitly as follows

$$-\int_{\partial\Omega} (\psi_i \cdot \mathbf{n}) f \, dx = \delta_{i1}\overline{u_0} - \delta_{iN}\overline{u_L} \quad i = 1, \ldots, N. \tag{4.11}$$

4.3.2 Algebraic system

We define matrices and vectors associated with the integrals in (4.10):

$$A_{ij} := \int_\Omega D^{-1}\psi_j\psi_i \, dx \qquad i, j = 1, \ldots, N \tag{4.12a}$$

$$B_{ki} := -\int_\Omega \varphi_k \frac{\partial \psi_i}{\partial x} \, dx \qquad k = 1, \ldots, M,\ i = 1, \ldots, N \tag{4.12b}$$

$$C_{ik} := -\int_\Omega D^{-1} v \psi_i \varphi_k \, dx \qquad i = 1, \ldots, N,\ k = 1, \ldots, M \tag{4.12c}$$

$$E_{kl} := -\int_\Omega c\varphi_l\varphi_k \, dx \qquad k, l = 1, \ldots, M \tag{4.12d}$$

$$g_k := -\int_\Omega g\varphi_k \, dx \qquad k = 1, \ldots, M \tag{4.12e}$$

$$f_i := \delta_{i1}\overline{u_0} - \delta_{iN}\overline{u_L} \qquad i = 1, \ldots, N. \tag{4.12f}$$

With this notation, system (4.10) reads:

$$\begin{bmatrix} A & B^T + C \\ B & E \end{bmatrix} \begin{bmatrix} \mathbf{J} \\ \mathbf{U} \end{bmatrix} = \begin{bmatrix} \mathbf{f} \\ \mathbf{g} \end{bmatrix} \tag{4.13}$$

where $\mathbf{J} = \{J_i\}_{i=1}^N$ and $\mathbf{U} = \{u_k\}_{k=1}^M$ are the vectors of the degrees of freedom for J_h and u_h.

Due to the local support of the basis functions (see Figure 4.3), the matrices of the algebraic system are sparse, with a precise pattern that we are now going to analyze. Before doing this, to compute integrals in (4.12) we assume henceforth that all problem coefficients D, v, c and g are replaced by their *piecewise constant* representation over $\mathcal{T}_h$. Each representation will be denoted with the symbol $\widetilde{(\cdot)}$.

- Matrix $A \in \mathbb{R}^{N\times N}$ is tri-diagonal with elements:

$$\begin{cases} A_{i,i-1} = \dfrac{h_{i-1}}{6}\widetilde{D}_{i-1} & \text{(4.14a)} \\ A_{i,i} = \dfrac{h_{i-1}}{3}\widetilde{D}_{i-1} + \dfrac{h_i}{3}\widetilde{D}_i & \text{(4.14b)} \\ A_{i,i+1} = \dfrac{h_i}{6}\widetilde{D}_i & \text{(4.14c)} \end{cases}$$

- Matrix $B \in \mathbb{R}^{M\times N}$ has a bi-diagonal structure with elements:

$$\begin{cases} B_{k,k} = +1 & \text{(4.14d)} \\ B_{k,k+1} = -1 & \text{(4.14e)} \end{cases}$$

- Matrix $C \in \mathbb{R}^{N\times M}$ has a bi-diagonal structure with elements:

$$\begin{cases} C_{i,i-1} = -\dfrac{h_{i-1}}{2}\widetilde{D}_{i-1}^{-1}\widetilde{v}_{i-1} & \text{(4.14f)} \\ C_{i,i} = -\dfrac{h_{i-1}}{2}\widetilde{D}_{i-1}^{-1}\widetilde{v}_{i-1} & \text{(4.14g)} \end{cases}$$

- Matrix $E \in \mathbb{R}^{M\times M}$ is diagonal with elements:

$$E_{k,k} = -\widetilde{c}_k h_k \qquad \text{(4.14h)}$$

- Vector $\mathbf{g} \in \mathbb{R}^M$ is

$$g_k = -\widetilde{g}_k h_k \qquad \text{(4.14i)}$$

- Vector $\mathbf{f} \in \mathbb{R}^N$ is

$$f_i = \begin{cases} +\overline{u_0} & \text{if } i = 1 \\ -\overline{u_L} & \text{if } i = N \\ 0 & \text{otherwise} \end{cases} \qquad \text{(4.14j)}$$

4.3.3 Properties of DM method

Here below and throughout this chapter, $\mathcal{C}$ denotes a positive constant not depending on h whose value is not necessarily the same at each occurence.

The DM method presented above has the following properties:

1. The approximate flux J_h is *continuous* over $\overline{\Omega}$ unlike the standard piecewise-linear displacement-based FEM approximation where J_h is discontinuous over Ω. This property qualifies the DM method as being a *conservative* scheme.

2. Optimal convergence results (cf [36]) with equal-order approximation for *both* u_h and J_h, unlike the case of the standard piecewise-linear displacement-based FEM method:

   - $\|u - u_h\|_{L^2} \leq \mathcal{C}h$;
   - $\|J - J_h\|_{H^1} \leq \mathcal{C}h$.

   Moreover, the DM method enjoys the following superconvergence property

   $$\|\Pi_0 u - u_h\|_{L^2} \leq \mathcal{C}h^2 \tag{4.15}$$

   where Π_0 is the L^2-projection operator over V_h. The estimate (4.15) gives superconvergence of $\mathcal{O}(h^2)$ at the center of gravity of each element (but nothing better). We remind that in the case of the standard piecewise-linear displacement-based FEM, the sole variable is the displacement function $u \in Q$, and its approximation $u_h \in Q_h$ satisifies the following estimates:

   $$\|u - u_h\|_{H^1} \leq \mathcal{C}h$$
   $$\|u - u_h\|_{L^2} \leq \mathcal{C}h^2.$$

3. From (4.10b) we immediately see that the property of *self-equilibrium* is satisfied within each element:

   $$\forall K \in \mathcal{T}_h \quad \left.\frac{\partial J_h}{\partial x}\right|_K = \widetilde{g} - \widetilde{c}u_K. \tag{4.16}$$

   Relation (4.16) is the discrete counterpart of equation (4.6a).

The DM method also suffers some limitations and drawbacks:

- Dirichlet boundary condition are satisfied only in a weak sense;
- the number of unknowns $N + M$ is far larger than in the corresponding standard piecewise-linear displacement-based FEM method, this inconvenience becoming increasingly more severe in 2 and 3 spatial dimensions.

To overcome these latter problems, we illustrate in the remainder of the chapter the so-called hybridized version of the DM method.

4.4 Dual-Mixed-Hybridized (DMH) method

The DM method uses conforming finite elements in approximating the flux. By doing this, it requires *a-priori* that the global finite element approximation of J_h satisfies continuity at interelement boundaries.

The approach of hybrid methods is different. *Hybrid* finite element methods are special mixed methods obtained by regarding the continuity requirements as constraints and using the method of *Lagrange multipliers* to enforce the constraints in an "average" (variational) sense. The result of such a formulation is that *independent* approximations of the solutions *in the interior of an element* and on *its boundary* of an element can be made.

4.4.1 Finite Element formulation

We introduce a new discrete functional space

$$\Lambda_h := \{\lambda_h : \mathcal{N}_h \to \mathbb{R}\} \tag{4.17}$$

which is the space of functions defined only at the vertices of $\mathcal{T}_h$. The dimension of Λ_h is equal to the number of vertices N. Any function $\lambda_h \in \Lambda_h$ can be written in the form:

$$\lambda_h(x) = \sum_{j=1}^{N} \lambda_j \xi_j(x) \tag{4.18}$$

where the real numbers λ_j are the *degrees of freedom* of λ_h and ξ_j, $j = 1, \ldots, N$ are the basis functions of Λ_h, defined as:

$$\xi_i(x) = \begin{cases} 1 & \text{if } x = x_i \in \mathcal{N}_h \\ 0 & \text{elsewhere} \end{cases} \tag{4.19}$$

Function $\xi_i(x)$ is represented in Figure 4.4.

Figure 4.4: The basis function ξ_i for space Λ_h.

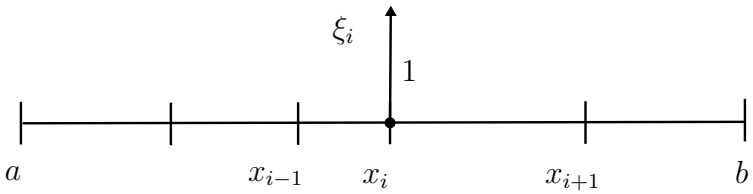

Now, we consider each element $K \in \mathcal{T}_h$ as an individual entity which is "connected" with other elements only through the "interdomain boundary"

$\mathcal{N}_h \cap \partial K$. We introduce the spaces Q_h^* and $\Lambda_{h,\rho}$:

$$Q_h^* := \{q_h \in L^2(\Omega) \text{ s.t. } q_h|_K \in \mathbb{P}_1(K)\, \forall K \in \mathcal{T}_h\} \tag{4.20}$$

$$\Lambda_{h,\rho} := \{\lambda_h \in \Lambda_h \text{ s.t. } \lambda_h(a) = \rho_a, \lambda_h(b) = \rho_b\} \tag{4.21}$$

where ρ_a and ρ_b are two given real numbers. Problem (4.8) is then reformulated as:

Find $(J_h^*, u_h^*, \lambda_h) \in Q_h^* \times V_h \times \Lambda_{h,\bar{u}}$ such that, for all $(q_h, w_h, \xi_h) \in Q_h^* \times V_h \times \Lambda_{h,0}$:

$$\sum_{K\in\mathcal{T}_h} \left[\int_K D^{-1}\,(J_h^* - v u_h^*)\, q_h \, dx - \int_K u_h^* \frac{\partial q_h}{\partial x}\, dx + \int_{\partial K} (q_h \cdot \mathbf{n}|_{\partial K}) \lambda_h \, dx \right] = 0 \tag{4.22a}$$

$$-\sum_{K\in\mathcal{T}_h} \left[\int_K \frac{\partial J_h^*}{\partial x} w_h \, dx - \int_K c u_h^* w_h \, dx \right] = -\sum_{K\in\mathcal{T}_h} \int_K g w_h \, dx \tag{4.22b}$$

$$\sum_{K\in\mathcal{T}_h} \int_{\partial K} (J_h^* \cdot \mathbf{n}|_{\partial K}) \xi_h \, dx = 0 \tag{4.22c}$$

Remark 4.1. According to system (4.22), the request of global continuity for J_h^* has been removed. In fact $Q_h \subset Q_h^*$ and $\dim(Q_h^*) = 2M > \dim(Q_h) = N$ so that, a priori, $J_h^* \neq J_h$. However, the continuity of J_h^* across interdomain boundaries is implied by conditions (4.22c) (as can be checked by definition of $\Lambda_{h,0}$ and by (4.19)) and, as a matter of fact, system (4.22) furnishes $J_h^* = J_h$. As a consequence, replacing J_h^* with J_h in (4.22b) we immediately get that u_h^* coincides with the function u_h computed by the DM method.

Remark 4.2. The equation $J_h^* = J_h$ is an identity between two functions. Clearly the corresponding coefficient arrays on the computer will not be equal to each other (they have different dimensions !).

Remark 4.3. The *hybrid variable* λ_h is the Lagrange multiplier associated with the continuity constraint of $J_h^* \cdot \mathbf{n}$ and it can be regarded as an approximation of u at the grid nodes:

$$\lambda_h \simeq u|_{\mathcal{N}_h}. \tag{4.23}$$

4.4.2 Localization

Thanks to the choice of the space Q_h^*, equations (4.22a) and (4.22b) are constituted of M *local* sub-problems, each of which is related to the others through constraint (4.22c). Before describing each sub-problem, we need to introduce local matrices. We refer to Figure 4.5 for new notation.

Figure 4.5: Generic element $K \in \mathcal{T}_h$ with local numeration and local degrees of freedom for J_h^*, u_h^* and λ_h.

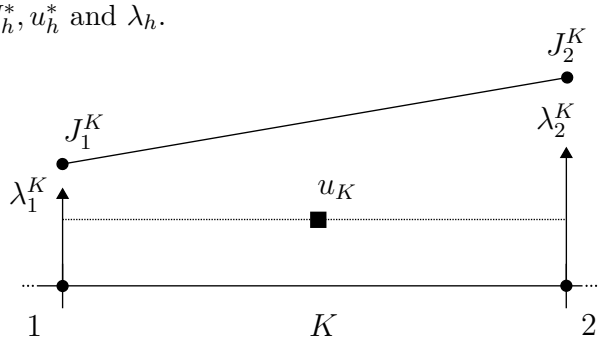

Local matrices We define the matrix

$$(L_K)_{ij} := \int_{\partial K} (\psi_i \cdot \mathbf{n}) \xi_j \quad i, j = 1, 2 \tag{4.24}$$

that is:

- $L_K \in \mathbb{R}^{2\times 2}$:

$$L_K = \begin{bmatrix} -1 & 0 \\ 0 & +1 \end{bmatrix} \tag{4.25a}$$

Other local matrices have the same definition as in (4.12) provided to replace Ω with K in the integrals, and their explicit expressions are:

- $A_K \in \mathbb{R}^{2\times 2}$:

$$A_K = \widetilde{D}_K^{-1} \frac{h_K}{6} \begin{bmatrix} 2 & 1 \\ 1 & 2 \end{bmatrix} \tag{4.25b}$$

- $B_K \in \mathbb{R}^{1\times 2}$:

$$B_K = [+1, -1] \tag{4.25c}$$

- $C_K \in \mathbb{R}^{2\times 1}$:

$$C_K = -\widetilde{D}_K^{-1} \widetilde{v}_K \frac{h_K}{2} \begin{bmatrix} 1 \\ 1 \end{bmatrix} \tag{4.25d}$$

- $E_K \in \mathbb{R}^{1\times 1}$:

$$E_K = -\widetilde{c}_K h_K \tag{4.25e}$$

- $g_K \in \mathbb{R}^{1\times 1}$:

$$g_K = -\widetilde{g}_K h_K \tag{4.25f}$$

Local subproblems Now we can give an equivalent formulation of problem (4.22) in terms of local sub-problems:

$$\begin{cases} A_K \mathbf{J}_K + (B_K^T + C_K) u_K + L_K \boldsymbol{\lambda}_K = \mathbf{0} & \forall\, K \in \mathcal{T}_h \quad (4.26a) \\ B_K \mathbf{J}_K + E_K u_K = g_K & \forall\, K \in \mathcal{T}_h \quad (4.26b) \\ \sum_{K \in \mathcal{T}_h} \int_{\partial K} (J_h^* \cdot \mathbf{n}|_{\partial K}) \xi_h \, dx = 0 & \forall \xi_h \in \Lambda_{h,0} \quad (4.26c) \end{cases}$$

where $\mathbf{J}_K = [J_1^K, J_2^K]^T$ and $\boldsymbol{\lambda}_K = [\lambda_1^K, \lambda_2^K]^T$.

Remark 4.4. The unknowns of system (4.26) are $\mathbf{J} = \{J_i^*\}_{i=1}^{2M}$ (J_h^* has two distinct values for each interior node, in principle), $\mathbf{U} = \{u_k^*\}_{k=1}^{M}$ and $\boldsymbol{\lambda} = \{\lambda_j\}_{j=2}^{N-1}$ ($\lambda_1 = \overline{u_0}, \lambda_N = \overline{u_L}$). The total number of unknowns is then equal to $2M + M + (N-2)$, which is about twice larger than that of DM method. However, using the static condensation procedure illustrated in Section 4.4.3, the dimension of the linear algebraic system to be solved is the *same* as that of the standard piecewise-linear displacement-based FEM method, see Section 4.4.4.

4.4.3 Static condensation

Consider a generic element $K \in \mathcal{T}_h$. From the first equation of system (4.26), we can obtain $\mathbf{J}_K$ by inverting matrix A_K:

$$\mathbf{J}_K = -A_K^{-1} \left[(B_K^T + C_K) u_K + L_K \boldsymbol{\lambda}_K \right] \quad (4.27)$$

and substituting it into the second equation of (4.26), we get u_K:

$$u_K = H_K^{-1} \left[g_K + B_K A_K^{-1} L_K \boldsymbol{\lambda}_K \right] \quad (4.28)$$

where

$$H_K := -B_K A_K^{-1} (B_K^T + C_K) + E_K \in \mathbb{R}. \quad (4.29)$$

Now, using (4.28) into (4.27), we can express $\mathbf{J}_K$ in terms of the sole hybrid variable $\boldsymbol{\lambda}_K$ and of g_K:

$$\mathbf{J}_K = -\left[A_K^{-1} (B_K^T + C_K) H_K^{-1} B_K A_K^{-1} L_K^T + A_K^{-1} L_K \right] \boldsymbol{\lambda}_K - A_K^{-1} (B_K^T + C_K) H_K^{-1} g_K \quad (4.30)$$

This way of proceeding is known as *static condensation* and corresponds to Gaussian elimination at the level of the element $K \in \mathcal{T}_h$.
To make notation more compact, we define

$$M_K := -\left[A_K^{-1}(B_K^T + C_K)H_K^{-1}B_K A_K^{-1}L_K^T + A_K^{-1}L_K\right] \in \mathbb{R}^{2\times 2} \tag{4.31}$$

and

$$\mathbf{b}_K := -A_K^{-1}(B_K^T + C_K)H_K^{-1}g_K \in \mathbb{R}^{2\times 1} \tag{4.32}$$

so that

$$\mathbf{J}_K = M_K\boldsymbol{\lambda}_K + \mathbf{b}_K. \tag{4.33}$$

4.4.4 Algebraic system

Equation (4.26c), which expresses the continuity constraint for J_h^* at internal nodes, results into the following $M-1$ conditions

$$J_2^{K_{i-1}} = J_1^{K_i} \quad i = 1, \dots, M-1. \tag{4.34}$$

Since

$$J_2^{K_{i-1}} = J_2^{K_{i-1}}(\lambda_{i-1}, \lambda_i) \tag{4.35}$$

$$J_1^{K_i} = J_1^{K_i}(\lambda_i, \lambda_{i+1}) \tag{4.36}$$

conditions (4.34) lead to a linear *tridiagonal* system for $\boldsymbol{\lambda}$. In particular, using (4.33), we have ($i = 1, \dots, M-1$):

$$\begin{cases} M_{21}^{K_i}\lambda_{i-1} + (M_{22}^{K_i} - M_{11}^{K_{i+1}})\lambda_i - M_{12}^{K_{i+1}}\lambda_{i+1} = b_1^{K_{i+1}} - b_2^{K_i} & \text{(4.37a)} \\ \lambda_1 = \overline{u_0}, \quad \lambda_N = \overline{u_L} & \text{(4.37b)} \end{cases}$$

which is a system of the form

$$\mathcal{M}\boldsymbol{\lambda} = \mathbf{f}^* \tag{4.38}$$

where matrix $\mathcal{M} \in \mathbb{R}^{M-1\times M-1}$ has elements

$$\begin{cases} \mathcal{M}_{i,i-1} = M_{21}^{K_i} & \text{(4.39a)} \\ \mathcal{M}_{i,i} = M_{22}^{K_i} - M_{11}^{K_{i+1}} & \text{(4.39b)} \\ \mathcal{M}_{i,i+1} = -M_{12}^{K_{i+1}} & \text{(4.39c)} \end{cases}$$

and vector $\mathbf{f}^* \in \mathbb{R}^{M-1}$ has elements $f_i^* = b_1^{K_{i+1}} - b_2^{K_i}$.

4.4.5 Properties of the DMH method

Once $\boldsymbol{\lambda}$ is obtained from system (4.38), we can compute $\mathbf{J}$ from (4.33) and $\mathbf{U}$ from (4.28). We have already checked that the pair (J_h^*, u_h^*) of the DMH method coincides with the pair (J_h, u_h) of the DM method. As a consequence, the DMH method shares the properties 1.–3. of the DM method (see Section 4.3.3). In addition, the DMH method, thanks to the introduction of the hybrid variable λ_h, alleviates all the limitations of DM method:

- Dirichlet boundary conditions are satisfied in a strong sense;
- the linear system has dimension equal to $M - 1$, which is the same as the standard displacement-based FEM method.

Finally, it can be proved that the hybrid variable enjoys the following super-convergence property [4]:

$$\|u - \lambda_h^*\|_{L^2} \leq \mathcal{C} h^2 \tag{4.40}$$

where $\lambda_h^* \in \mathbb{P}_1(\mathcal{T}_h)$ is the piecewise-linear continuous interpolate of λ_h on $\mathcal{T}_h$.

Remark 4.5. It is interesting to notice that all the convergence estimates and the properties enjoyed by the DMH method, which have been illustrated here in the one-dimensional setting, continue to hold in 2 and 3 spatial dimensions. This makes the DMH approximation scheme an attractive alternative approach to standard displacement-based methods when an accurate evaluation of the flux variable is demanded.

Chapter 5

Continuous and Discrete Maximum Principles

In this chapter we deal with the issue of ensuring stable numerical solutions in the presence of dominating convection and/or reaction terms. This property is related to the fact that the adopted discretization scheme enjoys a discrete maximum principle (DMP). This latter is the discrete counterpart of the continuous *maximum principle* (CMP) that is satisifed by the solution of boundary value problem (3.32).

In Section 5.1 we review the basic concepts of the CMP, while in Section 5.2 we address the numerical counterpart, the DMP. Then, Section 5.3 illustrates the stabilization approaches that are used to ensure that the DMH method satisfies the DMP even in the case where (3.32) is dominated by advection and/or reaction terms.

In Section 5.5 we numerically verify the theoretical convergence estimates of the DMH method reported in Chapter 4.

5.1 Continuous Maximum Principle

We illustrate the concept of 'maximum principle' for the following second order elliptic differential operator

$$\mathcal{L}u := \frac{\partial J}{\partial x} + cu = \frac{\partial}{\partial x}\left(-D\frac{\partial u}{\partial x} + vu\right) + cu : \Omega \to \mathbb{R}. \tag{5.1}$$

Definition 5.1 (Inverse monotonicity)**.** *Let $w \in C^2(\Omega) \cap C^0(\overline{\Omega})$. We say that*

$\mathcal{L}$ is inverse-monotone if the inequalities

$$\mathcal{L}w(x) \geq 0 \qquad \forall\, x \in \Omega \tag{5.2}$$

$$w(x) \geq 0 \qquad \forall\, x \in \partial\Omega \tag{5.3}$$

together imply that

$$w(x) \geq 0 \qquad \forall\, x \in \overline{\Omega}. \tag{5.4}$$

Remark 5.1. Inverse monotonicity has an important physical interpretation, because it mathematically expresses the fact that the dependent variable of the problem, say, a concentration, a temperature or a mass density, cannot take negative values.

Theorem 5.2 (Comparison principle)**.** *Suppose that there exists a function $\phi \in C^2(\Omega) \cap C^0(\overline{\Omega})$ such that*

$$\mathcal{L}u(x) \leq \mathcal{L}\phi(x) \qquad \forall\, x \in \Omega \tag{5.5}$$

$$u(x) \leq \phi(x) \qquad \forall\, x \in \partial\Omega. \tag{5.6}$$

Then, we have

$$u(x) \leq \phi(x) \qquad \forall\, x \in \Omega \tag{5.7}$$

and we say that ϕ is a barrier function *for u.*

Combining (5.4) and (5.7), we obtain the following result which is a very useful tool in the approximation process of the BVP (4.6).

Theorem 5.3 (Continuous Maximum Principle)**.** *Suppose that $\mathcal{L}$ is inverse-monotone and that the comparison principle holds for a suitable barrier function ϕ. Then, setting $M_\phi := \max_{x\in\Omega} \phi(x)$, we have*

$$0 \leq u(x) \leq M_\phi \qquad \forall\, x \in \overline{\Omega} \tag{5.8}$$

and we say that u satisifies a continuous maximum principle (CMP).

5.2 Discrete Maximum Principle

If the solution of a given boundary value problem satisifies a CMP, then a properly designed approximation should behave in the same way. A numerical scheme that does not generate spurious global extrema in the interior of the computational domain is said to satisfy a *discrete maximum principle* (DMP).

We assume that the solution u of the BVP (4.6) satisfies the a priori estimate (5.8) and we characterize the conditions under which the same estimate is satisfied also by the DMH approximation λ_h^* computed by solving the linear algebraic system (4.38) associated with the problem.

The following definitions turn out to be useful.

Definition 5.4 (Inverse monotone matrix)**.** *An invertible square matrix A of size n is said to be inverse monotone if*

$$A^{-1} \geq 0 \tag{5.9}$$

the inequality being understood in the element-wise sense.

The following result is a consequence of the above definition.

Proposition 5.5. *Assume that A is inverse-monotone and let $\mathbf{w}, \mathbf{z} \in \mathbb{R}^n$. Then*

$$A\mathbf{w} \leq A\mathbf{z} \Rightarrow \mathbf{w} \leq \mathbf{z} \tag{5.10}$$

the inequalities being understood in the element-wise sense.

A special class of monotone matrices is that introduced below.

Definition 5.6 (M-matrix)**.** *An invertible square matrix A is an M-matrix if:*

- *$A_{ij} \leq 0$ for $i \neq j$;*
- *A is inverse-monotone.*

Theorem 5.7 (Sufficient condition for DMP)**.** *Assume that matrix $\mathcal{M}$ is an M-matrix. Then λ_h^* satisfies the DMP, i.e.*

$$0 \leq \lambda_h^*(x) \leq M_\phi \qquad \forall\, x \in \overline{\Omega}. \tag{5.11}$$

The following (necessary and sufficient) condition is useful to verify the property of being an M-matrix.

Theorem 5.8 (Discrete comparison principle)**.** *Let A be an invertible matrix with non-positive off diagonal entries ($A_{ij} \leq 0$ for $i \neq j$). Then, A is an M-matrix if and only if there exists a positive vector $\mathbf{e}$ such that $A\mathbf{e} \geq 0$ (in the component-wise sense), with at least one row index i^* such that $(A\mathbf{e})_{i^*} > 0$.*

5.3 Stabilization Techniques for the DMH method

Numerical stability can be obtained by decreasing the mesh size h. However, a smaller value of h means a larger size of the linear algebraic system and thus an increased computational effort. To avoid this inconvenience, we introduce two specific approaches that ensure numerical stability without necessarily resorting to a small value of h:

1. diagonal *lumping* of the local mass flux matrix A_K (for dominant reaction);

2. addiction of an *artificial diffusion* (for dominant convection).

We show the efficacy of these techniques in the study of two model problems, special instances of the BVP (4.6). For ease of presentation, we set $L = 1$ and we subdivide the computational domain into $M = 10$ uniform intervals of size $h = 1/M = 0.1$. We also assume that the coefficients D, v, c and g are constant, with $g = 1$ and we take homogeneous boundary conditions, $u(0) = 0$, $u(1) = 0$.

5.3.1 Diffusion-reaction BVP: mass-lumping

In this case we have $v = 0$. The BVP problem is

$$\begin{cases} -D\dfrac{\partial^2 u}{\partial x^2} + cu = 1 \qquad \text{in } (0,1) \\ \\ u(0) = u(1) = 0. \end{cases} \tag{5.12}$$

A barrier function for u is $\phi(x) = 1/c$. If the diffusion coefficient is small compared to the reaction term, e.g $D = 10^{-3}$, $c = 1$, spurious (unphysical) oscillations arise near the boundaries, see Figure 5.1a. In order to eliminate such oscillations, we adopt the *mass-lumping* stabilization procedure which consists in substituting matrix A_K with the diagonal matrix $\widehat{A}_K$ obtained by summing by row the matrix A_K. This is equivalent to computing the integral (4.25b) with the trapezoidal quadrature rule. The numerical solution λ_h^* obtained with mass-lumping is illustrated in Figure 5.1b.

5.3.2 Diffusion-advection BVP: artificial diffusion

In this case we have $c = 0$. The BVP problem is

$$\begin{cases} -D\dfrac{\partial^2 u}{\partial x^2} + v\dfrac{\partial u}{\partial x} = 1 \qquad \text{in } (0,1) \\ \\ u(0) = u(1) = 0. \end{cases} \tag{5.13}$$

A barrier function for u is $\phi(x) = x/v$. If the diffusion coefficient is small compared to the advective term, e.g $D = 5 \cdot 10^{-3}$, $v = 1$, spurious (unphysical) oscillations arise in the neighbourhood of $x = 1$ and propagate throughout the entire domain polluting the overall quality of the computed solution, see

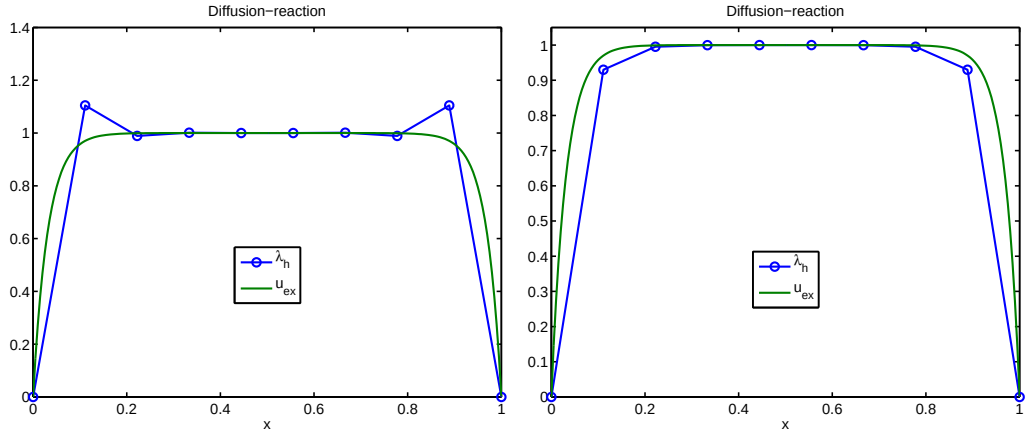

(a) No lumping **(b)** Lumping

Figure 5.1: Exact (green, solid line) and numerical solutions λ_h^* (blue line with bullets) of problem (5.12).

Figure 5.2a. The stabilization approach named *artificial diffusion* consists of replacing the diffusion coefficient D with the following modified expression

$$\widehat{D} := D\,(1 + \Phi(\mathcal{P}e_{loc})) \tag{5.14}$$

where $\mathcal{P}e_{loc} := \dfrac{|v|h}{2D}$ is the local Péclet number and $\Phi : \mathbb{R}^+ \to \mathbb{R}^+$ is a suitable stabilization function to be chosen in such a way that

$$\Phi(t) \geq 0 \tag{5.15a}$$

$$\lim_{t \to 0^+} \Phi(t) = 0. \tag{5.15b}$$

Two special choices of Φ are:

- Upwind (UP) stabilization function

$$\Phi^{UP}(t) := t \tag{5.16}$$

- Scharfetter-Gummel (SG) stabilization function

$$\Phi^{SG}(t) := t - 1 + \mathcal{B}(2t) \tag{5.17}$$

where

$$\mathcal{B}(t) := \frac{t}{e^t - 1} \tag{5.18}$$

is the Bernoulli function. In the case where (5.17) is adopted, the resulting stabilized DMH (applied to the solution of (5.13)) coincides with the standard SG exponentially fitted difference scheme [85].

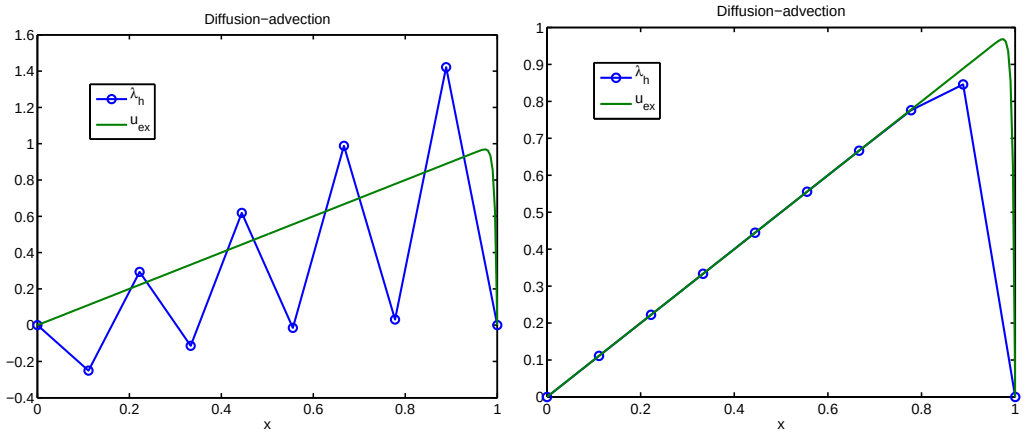

(a) No artificial diffusion **(b)** $\Phi = \Phi^{UP}$

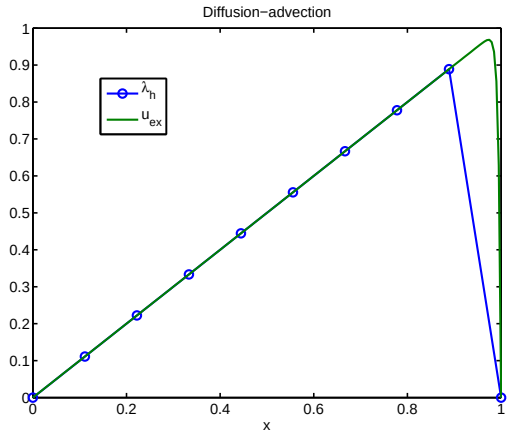

(c) $\Phi = \Phi^{SG}$

Figure 5.2: Exact (green, solid line) and numerical solutions λ_h^* (blue line with bullets) of problem (5.13).

Numerical solutions λ_h^* obtained with UP and SG stabilization functions are illustrated in Figures 5.2b and 5.2c, respectively. In the case of the SG stabilization function, the computed λ_h^* is *nodally exact*.

5.4 Why lumping and artificial diffusion work

In this section we show that, when diagonal-lumping and artificial diffusion techniques are adopted, the stiffness matrix $\mathcal{M}$ (4.39) is an M-matrix. This property guarantees that the solution λ_h^* is stable since it satisfies the DMP due to Theorem 5.7.

We assume throughout the section that problem coefficients D, v, c and g are positive and that the mesh size is uniform and given by $h = 1/M$. Consider a generic element K (see Figure (4.5) for notation). We have that

$$J_{h|_K} = J_1\psi_1 + J_2\psi_2 \tag{5.19}$$

and consequently

$$\frac{\partial J_{h|_K}}{\partial x} = J_1\frac{\partial \psi_1}{\partial x} + J_2\frac{\partial \psi_2}{\partial x} = \frac{J_2 - J_1}{h}. \tag{5.20}$$

From equation (4.22a), when $q_h = \psi_1$

$$D^{-1}\int_{x_1}^{x_2}(J_1\psi_1 + J_2\psi_2)\psi_1\,dx - D^{-1}vu\int_{x_1}^{x_2}\psi_1\,dx \\ - u\int_{x_1}^{x_2}\frac{\partial \psi_1}{\partial x}\,dx + \int_{\partial K}\psi_1(\lambda_1\xi_1 + \lambda_2\xi_2)\cdot n_{\partial K} = 0 \tag{5.21}$$

Using the diagonal-lumping on matrix A_K, which is equivalent to using the trapezoidal quadrature rule, the first integral is approximated with

$$D^{-1}\int_{x_1}^{x_2}(J_1\psi_1 + J_2\psi_2)\psi_1\,dx \simeq D^{-1}J_1\frac{h}{2} \tag{5.22}$$

so that from (5.21) we get

$$J_1 - vu + D\frac{u}{h/2} - \lambda_1\frac{D}{h/2} = 0. \tag{5.23}$$

When $q_h = \psi_2$, we similarly get

$$J_2 - vu - D\frac{u}{h/2} + \lambda_2\frac{D}{h/2} = 0. \tag{5.24}$$

Thus, using the trapezoidal rule to compute flux mass matrix, $\forall\, K \in \mathcal{T}_h$ equations (4.22a) and (4.22b) read

$$J_1 - vu + D\frac{u}{h/2} - \lambda_1\frac{D}{h/2} = 0 \tag{5.25a}$$

$$J_2 - vu - D\frac{u}{h/2} + \lambda_2\frac{D}{h/2} = 0 \tag{5.25b}$$

$$J_2 - J_1 + cuh = gh \tag{5.25c}$$

where (5.25c) follows from (4.22b) and (5.20).

Now, we impose continuity for J_h at every interior node x_i ($i = 2, \ldots, N-1$)

$$J_2^- = J_1^+ \tag{5.26}$$

Here and in the remainder of this section, superscripts $-$ and $+$ refer to quantities on the interval $K_i^- = [x_{i-1}, x_i]$ and $K_i^+ = [x_i, x_{i+1}]$, respectively. Combining equations (5.25) with condition (5.26), we get

$$\begin{aligned} -\lambda_i \frac{2D^-}{h} + \frac{(v^- + \frac{2D^-}{h})(g^- h^2 + 2\lambda_{i-1} D^- + 2\lambda_i D^-)}{4D^- + c^- h^2} \\ = \lambda_i \frac{2D^+}{h} + \frac{(v^+ - \frac{2D^+}{h})(g^+ h^2 + 2\lambda_i D^+ + 2\lambda_{i+1} D^+)}{4D^+ + c^+ h^2}. \end{aligned} \tag{5.27}$$

Reordering, we get

$$\mathcal{M}_{i,i-1}\lambda_{i-1} + \mathcal{M}_{i,i}\lambda_i + \mathcal{M}_{i,i+1}\lambda_{i+1} = f_i \tag{5.28}$$

where

$$\mathcal{M}_{i,i-1} = -\left(v^- + \frac{2D^-}{h}\right)\frac{2D^-}{4D^- + c^- h^2} \tag{5.29a}$$

$$\mathcal{M}_{i,i} = 2\frac{D^- + D^+}{h} - \left(v^- + \frac{2D^-}{h}\right)\frac{2D^-}{4D^- + c^- h^2} + \left(v^+ - \frac{2D^+}{h}\right)\frac{2D^+}{4D^+ + c^+ h^2} \tag{5.29b}$$

$$\mathcal{M}_{i,i+1} = +\left(v^+ - \frac{2D^+}{h}\right)\frac{2D^+}{4D^+ + c^+ h^2} \tag{5.29c}$$

$$f_i = \frac{g^- h^2 \left(v^- + \frac{2D^-}{h}\right)}{4D^- + c^- h^2} - \frac{g^+ h^2 \left(v^+ - \frac{2D^+}{h}\right)}{4D^+ + c^+ h^2} \tag{5.29d}$$

Assuming for sake of simplicity that problem coefficients $D(x), v(x), c(x)$, and

$g(x)$ are constant quantities over Ω, relations (5.29) become

$$\mathcal{M}_{i,i-1} = -\left(v + \frac{2D(1+\Phi)}{h}\right)\frac{1}{2+\dfrac{ch^2}{2D}} \tag{5.30a}$$

$$\mathcal{M}_{i,i} = \frac{4D(1+\Phi)}{h}\left(\frac{1+\frac{ch^2}{2D}}{2+\frac{ch^2}{2D}}\right) \tag{5.30b}$$

$$\mathcal{M}_{i,i+1} = \left(v - \frac{2D(1+\Phi)}{h}\right)\frac{1}{2+\dfrac{ch^2}{2D}} \tag{5.30c}$$

$$f_i = \frac{gh}{2+\dfrac{ch^2}{2D}} \tag{5.30d}$$

where the original diffusion coefficient D has been replaced by the stabilized counterpart $D(1+\Phi)$.

Recalling that $v > 0$, it turns out that $\mathcal{M}_{i,i-1}$ is < 0. Moreover, we have $\mathcal{M}_{i,i} > 0$ and $f_i > 0$. In the case where $\Phi \equiv 0$ (no stabilization) if we assume that

$$v - \frac{2D}{h} < 0 \tag{5.31}$$

that is

$$\mathcal{P}e_{loc} = \frac{|v|h}{2D} < 1, \tag{5.32}$$

then $\mathcal{M}$ is an M-matrix.
If we choose $\Phi = \Phi^{UP}$ or $\Phi = \Phi^{SG}$, it is easy to verify that

$$\sum_{j=1,\ldots,N} \mathcal{M}_{i,j} > 0 \tag{5.33}$$

for every interior node ($i = 2, \ldots, N-1$), and

$$\mathcal{M}_{1,1} + \mathcal{M}_{1,2} > 0 \tag{5.34}$$

$$\mathcal{M}_{N-1,N-1} + \mathcal{M}_{N,N} > 0 \tag{5.35}$$

at boundary nodes. From Theorem (5.8), matrix $\mathcal{M}$ (5.30) is then an M-matrix irrespective of the value of $\mathcal{P}e_{loc}$ and the corresponding stabilized DMH method satisfies the DMP.

Table 5.1: Various error norms for numerical solutions u_h and λ_h^* as a function of the number of intervals M. No stabilization is adopted.

M	$\|u-u_h\|_{L^2}$	$\|\Pi_0 u-u_h\|_{L^2}$	$\|u-\lambda_h^*\|_{L^2}$	$\|u-\lambda_h^*\|_{\infty,h}$
10	4.77887e-01	2.21777e-01	1.30666e-01	8.64963e-02
20	1.91869e-01	6.25684e-02	3.38644e-02	2.22424e-02
40	8.63963e-02	1.61248e-02	8.54321e-03	5.60052e-03
80	4.18183e-02	4.06198e-03	2.14066e-03	1.40542e-03
160	2.07297e-02	1.01743e-03	5.35468e-04	3.51510e-04
320	1.03422e-02	2.54479e-04	1.33886e-04	8.78873e-05
640	5.16826e-03	6.36272e-05	3.34727e-05	2.19724e-05
1280	2.58377e-03	1.59073e-05	8.36820e-06	5.49311e-06
2560	1.29184e-03	3.97683e-06	2.09202e-06	1.37325e-06

5.5 Experimental Convergence Analysis of the DMH method

In this section we numerically verify the convergence estimates of the DMH method. We consider the model BVP (3.32) with with homogeneous BCs, $u(0) = u(L) = 0$, $L = 5$, coefficients $D = v = c = 1$, and $g(x) = e^{-x}\left[x^2 - (6+L)x + 3L - 2\right]$ in such a way that the exact solution is the pair

$$u(x) = xe^{-x}(L-x), \qquad J(x) = -e^{-x}\left[2x^2 + 2x(L-1) + L\right].$$

In the numerical approximation of the problem, the mesh size is uniform and equal to $h = L/M$, with $M = [10, 20, 40, 80, 160, 320, 640, 1280, 2560]^T$. Table 5.1 illustrates the convergence history of the DMH method by reporting various error norms for $u - u_h$ and $u - \lambda_h^*$. The discrete maximum norm $\|\cdot\|_{\infty,h}$ associated with the triangulation $\mathcal{T}_h$ is defined for each continuous function $\eta(x) : [0, L] \to \mathbb{R}$ as

$$\|\eta(x)\|_{\infty,h} := \max_{x_i \in \mathcal{N}_h} |\eta(x_i)|. \tag{5.36}$$

Table 5.2 reports the error $J - J_h$ in the L^2-norm and in the $H_{\text{div}} \equiv H^1$-norm.

The analysis of the asymptotic convergence orders that are predicted by Tables 5.1 and 5.2 show that the computed numerical solutions verify the following error estimates

- $\|u - u_h\|_{L^2} \leq \mathcal{C}h$
- $\|\Pi_0 u - u_h\|_{L^2} \leq \mathcal{C}h^2$

Table 5.2: Error norms H^1 and L^2 for numerical solution J_h as a function of the number of intervals M. No stabilization is adopted.

M	$\|J - J_h\|_{L^2}$	$\|J - J_h\|_{H^1}$
10	3.28036e-01	2.60239e+00
20	8.75295e-02	1.30056e+00
40	2.16140e-02	6.47536e-01
80	5.29217e-03	3.23222e-01
160	1.30365e-03	1.61529e-01
320	3.23124e-04	8.07533e-02
640	8.04091e-05	4.03752e-02
1280	2.00543e-05	2.01874e-02
2560	5.00749e-06	1.00937e-02

- $\|u - \lambda_h^*\|_{L^2} \leq \mathcal{C}h^2$
- $\|u - \lambda_h^*\|_{\infty,h} \leq \mathcal{C}h^2$
- $\|J - J_h\|_{H^1} \leq \mathcal{C}h$
- $\|J - J_h\|_{L^2} \leq \mathcal{C}h^2$

The above results are in excellent agreement with the expected theoretical convergence rates illustrated in Chapter 4.

5.5.1 Error estimates in presence of numerical stabilization

The error estimates just illustrated were obtained without any stabilization technique since the problem is neither advection nor reaction dominated. Stabilization techniques usually introduce additional approximation errors that may reduce the accuracy of the computed numerical solution. We repeat the previous experimental analysis by introducing lumping and/or artificial diffusion stabilizations in order to investigate whether such stabilizations decrease the convergence order predicted by the theory valid for the non-stabilized method.

Lumping Numerical results (not reported here) show that when the lumping stabilization technique is adopted, the numerical solution does not lose accuracy, and the error estimates listed above are still fulfilled.

Artificial diffusion When adding artificial diffusion, results (again not reported here) depend on the stabilization function used. If $\Phi = \Phi^{UP}$, the extra diffusion introduced is excessive and all error estimates become of order $\mathcal{O}(h)$.

Instead, when $\Phi = \Phi^{SG}$ the error estimates remain optimal. This different behaviour is due to the fact that the SG stabilization is second order accurate with respect to $\mathcal{P}e_{loc}$ ($\Phi^{SG} = \mathcal{O}(h^2)$ as $\mathcal{P}e_{loc} \to 0^+$), while the upwind stabilization is only first order accurate ($\Phi^{UP} = \mathcal{O}(h)$ as $\mathcal{P}e_{loc} \to 0^+$). The obtained numerical error estimates for SG and Upwind stabilizations are compared in Figure 5.3.

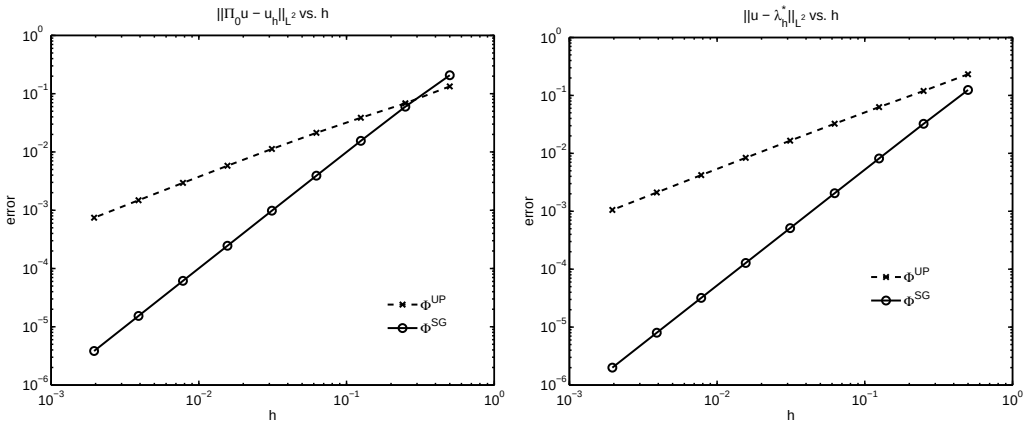

(a) $\|\Pi_0 u - u_h\|_{L^2}$

(b) $\|u - \lambda_h^*\|_{L^2}$

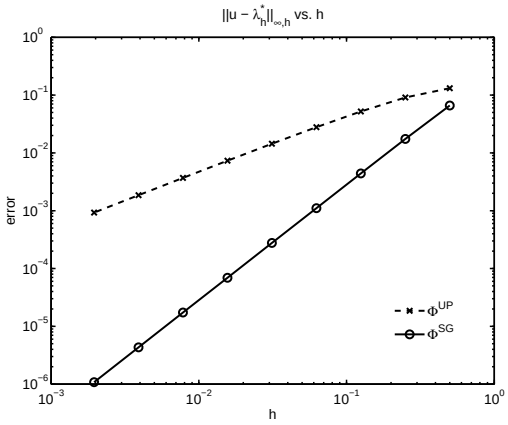

(c) $\|u - \lambda_h^*\|_{\infty,h}$

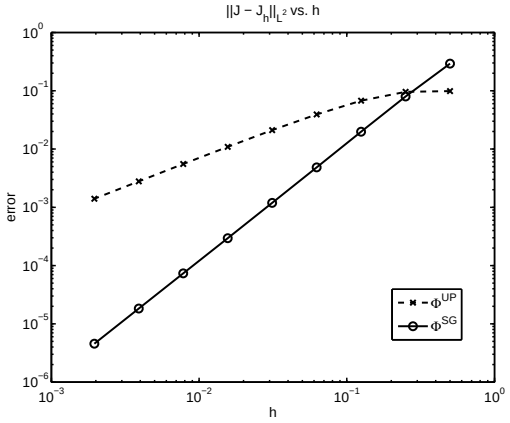

(d) $\|J - J_h\|_{L^2}$

Figure 5.3: Comparison among error estimates as a function of mesh size h in the case of Φ^{UP} (dashed lines with $\times$) and Φ^{SG} (solid lines with $\circ$).

Chapter 6

Simulation Results

In this chapter we report and discuss extensive numerical results obtained by simulating several types of biological and synthetic nanochannels. The main purpose is to compare the different models illustrated in Chapter 2 (THD, HD, ET and DD) and to investigate their impact on channel system behaviour.

In Section 6.1 we highlight the fundamental aspects of mathematical modeling of a nanochannel in one spatial dimension.

The input parameters and the output solutions on which we mainly focus are listed in Section 6.2 and 6.3, respectively.

In Section 6.4 we study the gramicidin-A channel, which due to its permanent charge profile can be regarded as a ballistic diode.

Section 6.5 deals with another biological channel, the calcium release channel (CRC) of sarcoplasmic reticulum, which regulates the activation of contraction in the cardiac muscle.

In Section 6.6 we study a synthetic bipolar nanochannel which acts as a semiconductor *pn* junction diode.

In Section 6.7 we address the study of another important channel in biological applications, the K-channel, in which a more realistic representation of the computational geometry of the domain is performed by including also the presence of the ending baths.

6.1 Preliminary considerations and experimental setup

In this section we focus on the geometrical and mathematical description of a nanochannel in one spatial dimension.

6.1.1 Structure and geometry

A typical nanofluidic device is based on a single nanochannel with conical or cylidrical shape, length L and radius $a(x)$ (which may vary with position x along the channel, $x \in [0, L]$). The nanochannel in Figure 6.1 is connected to reservoirs (also called baths) $\mathtt{L}$ and $\mathtt{R}$ with specified bulk concentrations $C_{\mathtt{L}}, C_{\mathtt{R}}$. Each of the baths is held at an externally applied voltage $\overline{V}_{\mathtt{L}}$, $\overline{V}_{\mathtt{R}}$ by means of a voltage clamp apparatus. The channel experiences an external applied bias equal to $V_{app} := \overline{V}_{\mathtt{L}} - \overline{V}_{\mathtt{R}}$.

Figure 6.1: Schematic representation of a synthetic conical nanochannel with radius $a(x)$ and length L. Part of the channel is positively charged, $+\sigma$, the remaining part is negatively charged, $-\sigma$. The channel connects two reservoirs, one held at $\overline{V}_{\mathtt{L}}$, the other held at $\overline{V}_{\mathtt{R}}$. Ions have equal concentrations $C_{\mathtt{L}}$,$C_{\mathtt{R}}$ in the reservoirs.

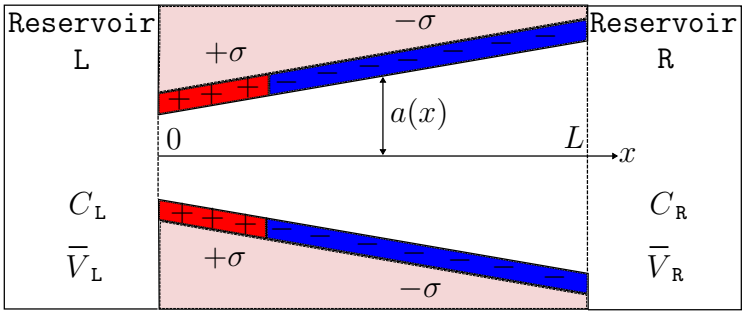

One conformation We assume that open ionic channels are *fixed structures*, i.e., we do not account for conformation changes or changes in chemical bonds.

Channel size The motion of ions through a channel depends on the geometry of the hole in the protein. Atoms cannot long exist in the same place at the same time, and so a hole of larger *diameter* will let through more ions in a given time (with a given driving force) than a hole of smaller diameter. A channel of longer *length* is likely to expose the permeating ion to greater friction, and thus to allow less flow of ions in a given time (with a given driving force) than a shorter channel. The geometry of the open channel is thus an important feature of the protein.

6.1.2 Permanent charge

Proteins and channels have static electric charge, determined by their chemical structure. Different types of channels have different pores made with linings

of different charge, which arise from the sequences of amino acids. This structural charge (which we suppose to be *fixed*, i.e.: we do not deal with ionization effects) is likely to determine the conductive properties of proteins. We assume that the only difference between different types of open channels is their different distributions of fixed charge $N_{dop}(x)$. The function $N_{dop}(x)$ is a one dimensional representation of the full three dimensional distribution of (fixed) charge in the protein.

One-dimensional geometry Synthetic nanopores are usually built with conical or cylindrical shape. A properly radial symmetry approximation is adopted, in such a way that the problem reduces to two spatial dimensions. A surface charge density function $\sigma(x)$ is prescribed on the pore walls, see Figure 6.1.

In this work we carry out numerical simulations in one spatial dimension only, and so we need to convert the surface charge density $\sigma(x)$ into an equivalent volumetric charge distribution $N_{dop}(x)$ that enters the spatial charge density in the Poisson equation (see Section 6.1.3). In the case of a channel with radius $a(x)$ and surface charge $\pm\sigma(x)$, both depending on position x, we proceed as follows.

In a channel section within in the interval $[x, x + dx]$, the total charge Q_{tot} is

$$Q_{tot} = \pm 2\pi \int_x^{x+dx} a(z)\sigma(z)\, dz. \tag{6.1}$$

Dividing by the volume $V_{tot} = \frac{\pi}{3} dx(a(x)^2 + a(x + dx)^2 + a(x)a(x + dx))$ of the section and taking the limit as $dx \to 0$, one gets the volumetric charge density $N_{dop}(x)$:

$$N_{dop}(x) = \frac{1}{q} \lim_{dx\to 0} \frac{Q_{tot}}{V_{tot}} = \pm \frac{2\sigma(x)}{qa(x)}. \tag{6.2}$$

6.1.3 Poisson equation

The Poisson equation

$$\begin{cases} \operatorname{div}(\epsilon \mathbf{E}) = \rho \\ \mathbf{E} = -\nabla\phi \end{cases} \tag{6.3}$$

describes the electric field distribution in the channel due to the space charge density ρ. This latter consists of:

1. the charge density $q\sum_{i=1,\dots,M} z_i c_i$ of M ions species that can diffuse in the channel, each with charge $z_i q$ and concentration c_i. In the case of a mixture of monovalent ions, e.g. K^+ and Cl^-, we have $\rho = q(p-n)$;

2. the fixed charge density qN_{dop}. It is independent of the strength of the electric field and does not depend on the concentration of ions;

3. the dielectric charge (induced by the local electric field), which is generally very small compared to the structural charge and so it is *not directly included* in ρ but it is implicitly described by ϵ.

6.1.4 Boundary Conditions

Potential The boundary conditions for the potential in the real nanochannel applications are set by the experimental conditions. A special apparatus is used to control the potentials in the baths surrounding the channel: the potential on the right is held at zero ($\overline{V}_{\mathtt{R}} = 0$) and that on the left is maintained at $\overline{V}_{\mathtt{L}} = V_{app}$. As explained in Section 3.2.1, the resulting boundary conditions for the potential are:

$$\phi(0) = V_{app} + V_{bi}(0), \qquad \phi(L) = V_{bi}(L). \tag{6.4}$$

These boundary conditions are maintained by charge supplied to the system at its boundaries (i.e., by electrodes placed in the bath and/or inside a cell or pipette). This is the charge supplied by the voltage clamp apparatus (e.g., the patch clamp [83, 63]) used in measurements of ionic currents.

Concentrations The concentrations of ions must also be controlled if the properties of channels are to be easily understood. The boundary conditions for ion concentrations are the same as in Section 3.2.1:

$$n(0) = \frac{\sqrt{N_{dop}^2(0) + 4C_{\mathtt{L}}^2} + N_{dop}(0)}{2} \quad n(L) = \frac{\sqrt{N_{dop}^2(L) + 4C_{\mathtt{R}}^2} + N_{dop}(L)}{2} \tag{6.5a}$$

$$p(0) = \frac{\sqrt{N_{dop}(0)^2 + 4C_{\mathtt{L}}^2} - N_{dop}(0)}{2} \quad p(L) = \frac{\sqrt{N_{dop}(L)^2 + 4C_{\mathtt{R}}^2} - N_{dop}(L)}{2} \tag{6.5b}$$

If not otherwise stated, we suppose that reservoirs have identical bulk concentrations C_{bulk} of the specific salt solution, that is

$$C_{\mathtt{L}} = C_{\mathtt{R}} =: C_{bulk} \tag{6.6}$$

Table 6.1: Diffusion coefficient of some ions in water at infinite dilution at 298.15 K. Data from [66].

Ion	D ($\times 10^{-9}\,\mathrm{m^2 s^{-1}}$)
K^+	1.957
Cl^-	2.032
Na^+	1.334

Temperature If not otherwise stated, temperatures $\overline{T}_{\mathtt{L}}, \overline{T}_{\mathtt{R}}$ are equal and set to room temperature $T_0 = 300\,\mathrm{K}$:

$$\overline{T}_{\mathtt{L}} = \overline{T}_{\mathtt{R}} = T_0. \tag{6.7}$$

6.1.5 Physical coefficients

Diffusion Different types of ions experience a different amount of friction and so have different diffusion coefficients. The value of the diffusion coefficient inside the channel can be determined by estimation from experimental data or by Molecular Dynamics simulations. Furthermore, the diffusion coefficients of all ions are smaller inside the channel than in bulk solution because of the higher friction produced by geometrical constraints and special chemical and physical conditions inside the narrow channel.

The values of diffusion coefficients for typical monovalent ions in water are listed in Table 6.1.

Mobility The mobility coefficient of ions is related to the diffusion coefficient via Einstein relation

$$D_\nu = \mu_\nu \frac{k_B T_\nu}{q}. \tag{6.8}$$

In our computations, we first prescribe the value of D_ν and then obtain the value for μ_ν through equation (6.8).

Relaxation times Literature lacks information on the precise values for the relaxation times τ_p and τ_w in the context of biological channels, so we use empirical formulas from solid-state physics as done in [24], and set [6]:

$$\tau_{p_\nu} = \frac{m_\nu \mu_{0\nu} T_L}{q T_\nu}, \tag{6.9a}$$

$$\tau_{w_\nu} = \frac{3}{2} \frac{\mu_{0\nu} k_B T_\nu T_L}{q v_{sat}^2 (T_\nu + T_L)} + \frac{\tau_{p_\nu}}{2}, \tag{6.9b}$$

where μ_{0_ν} is the low-field mobility and v_{sat} is the *saturation velocity* (see the next paragraph). The same approach is used for ion *heat conductivity* in the channel:

$$\kappa_\nu = \frac{3}{2}\frac{\mu_{0_\nu} k_B^2 T_L}{q}\nu. \tag{6.10}$$

Saturation velocity The saturation velocity v_{sat} of the ion is the maximum drift velocity that ions can reach in their translational motion. The saturation velocity describes collisions, since it is related to the energy relaxation time τ_w (see equation (6.9b)). The larger the saturation velocity, the more frequent the collisions. Frequent collisions mean small temperature rise, because the medium relaxes faster and consequently there is less accumulation of thermal energy. In the limit of infinite frequency of collision ($\tau_w \to 0$), we recover the overdamped case of the DD model, see Section 2.4.4. In our simulations, the saturation velocity is treated as a parameter: a small value lies in the full hydrodynamic regime, while a large value corresponds to the overdamped case of the DD model, where temperature change is very small. An intermediate value belongs to the so-called 'adiabatic' regime. Specific values of v_{sat} that define overdamped, adiabatic and full hydrodynamic regimes depend on channel type and conditions.

6.2 Inputs

When running a numerical simulation we have to set the values of several parameters, each of which somehow affects the computed solution. These parameters are:

- externally applied bias V_{app};
- ion concentrations in the baths $C_{\mathtt{L}}$, $C_{\mathtt{R}}$;
- permanent charge profile $N_{dop}(x)$;
- channel geometry: length L and radius $a(x)$;
- saturation velocity v_{sat} (only for THD and HD models).

6.3 Outputs

The main purpose of this work is the study of temperature changes and how much these changes can affect current flow into the channel. We compare the

Table 6.2: Gramicidin-A channel data. Diffusion coefficients are in $\times 10^{-9}\,\mathrm{m^2 s^{-1}}$.

L [nm]	a [nm]	C_{bulk} [mM]	D_{K^+}	D_{Cl^-}	V_{app} [V]
2.5	0.2	100	1	2.03	± 0.1

results obtained from the DD model (which assumes constant temperature of ions and electrolyte channel) with those obtained from the THD, HD or ET models. The output current I is calculated as:

$$I = JA \tag{6.11}$$

where A is the average channel area and J is the total current density given by the sum of J_n and J_p. Temperature profiles for ions and lattice, as well as the various thermo-electric contributions to current flow, will also be investigated.

6.4 Gramicidin-A ("Ballistic diode")

In this section we aim to carry out a complete validation of the hierarchy of models presented in Chapter 2 and of the corresponding numerical schemes discussed in Chapters 3, 4 and 5 in the study of a biologically relevant application considered in [24]. The problem is represented by the gramicidin-A channel in which a $NaCl$ solution is flowing. Channel geometry and physical coefficients are listed in Table 6.2.

This channel is highly selective due to the negative profile of permanent charge, shown in Figure 6.2. Na^+ ions are attracted by the negative fixed charge and so they are the majority carriers while Cl^- are minority carriers so that their concentration is far lower than that of Na^+ ions, see Figure 6.4. In this sense, this channel can be regarded as a "ballistic diode" of type $p^+ - p - p^+$.

Remark 6.1. We carried out simulations with both ions Na^+ and Cl^-. However, the concentration of counterions is so small that it does not influence appreciably the system. So, for ease of presentation, we plot and discuss only physical quantities referred to ion Na^+.

6.4.1 HD model

In this section we compare the HD model with the DD/PNP model to see if and how the two models predict different behaviour in channel properties. Electric potential profiles, concentration profiles and electric field profile are almost the same between HD and DD models, see Figures 6.3, 6.4 and 6.5, respectively.

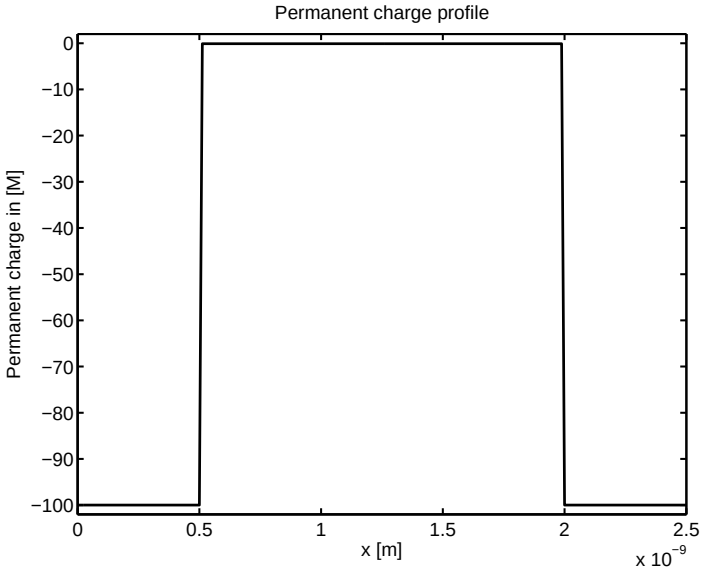

Figure 6.2: Permanent charge profile $N_{dop}(x)$. The value at left and right is $-100\,\mathrm{M}$, in the center $-0.1\,\mathrm{M}$. Discontinuities are located at $x = \frac{1}{5}L$ and $x = \frac{4}{5}L$.

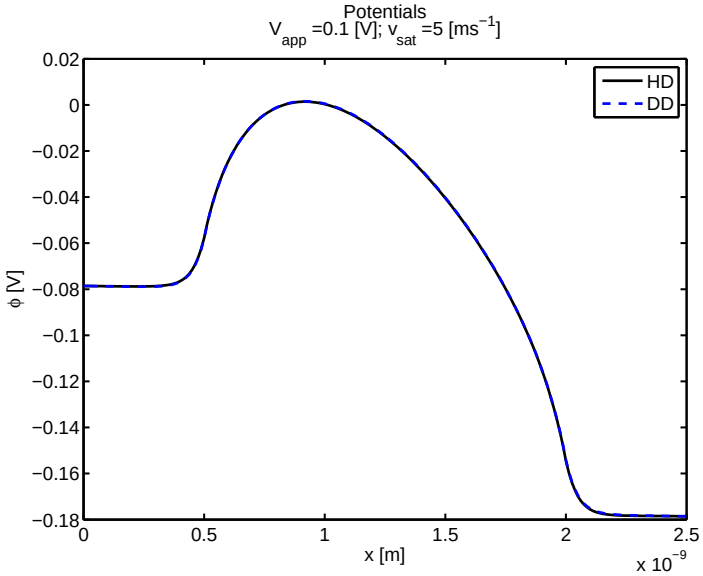

Figure 6.3: Electric potential profiles $\phi(x)$ for the HD model (black, solid line) and the DD model (blue, dashed line).

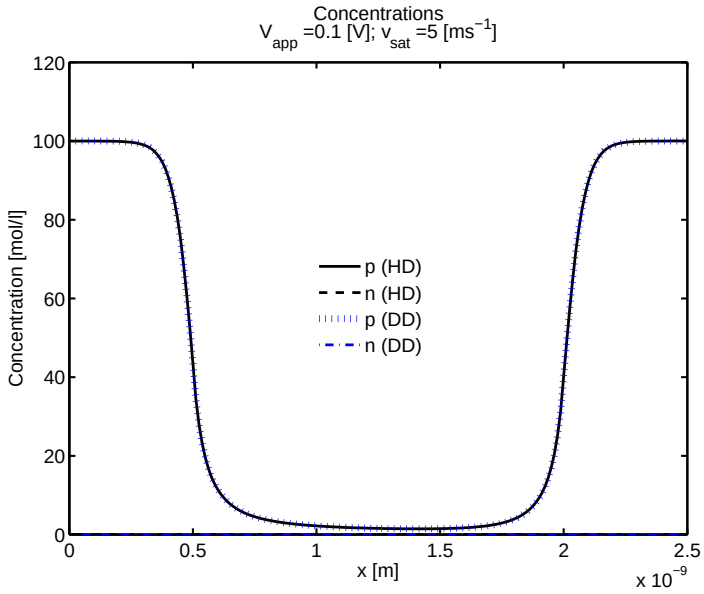

Figure 6.4: Concentration profiles $p(x), n(x)$ for the HD model (black lines) and the DD model (blue lines) The ion Na^+ is the majority carrier.

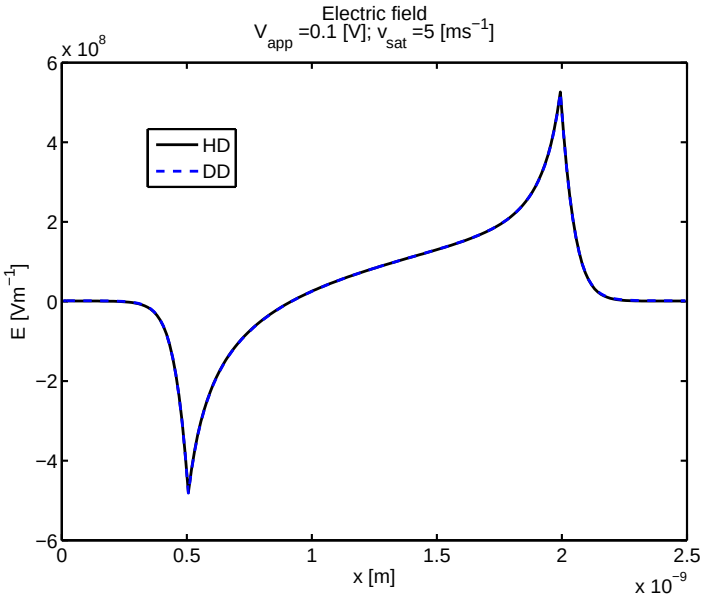

Figure 6.5: Electric field profile $E(x)$ for the HD model (black, solid line) and the DD model (blue, dashed line).

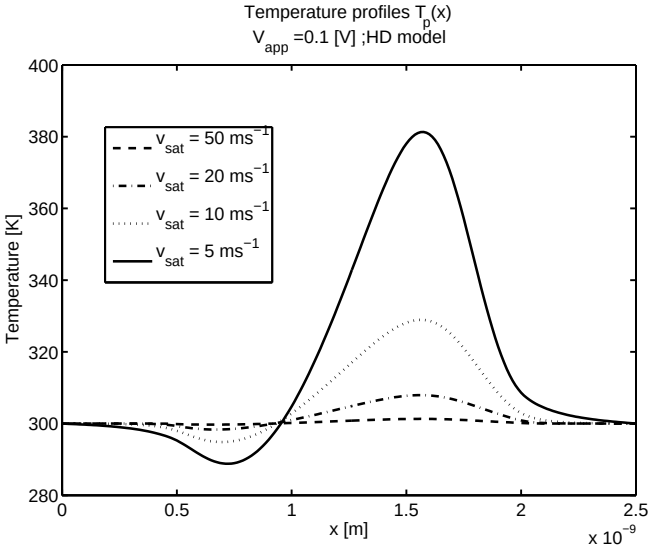

Figure 6.6: Temperature profiles $T_p(x)$ for different values of saturation velocity. The rise of temperature is reduced when the value of saturation velocity is increased, corresponding to the case with frequent collisions and an efficient damping of energy exchanges.

Temperature profiles In Figure 6.6 temperature profiles for different values of v_{sat} are illustrated. Temperature T_p rises some tens of degree with respect to the environment temperature $T_0 = 300\,\mathrm{K}$. The magnitude of temperature change reaches hundreds or thousands of degree if we apply an extremely high voltage, say $V_{app} = 0.5\,\mathrm{V}$ or higher, see Figure 6.7. It is thus clear that temperature changes may occur in this type of channel. Results are in very good agreement with those predicted in [24] where the simulation was carried out using appropriate solvers for hyperbolic systems (see Section 2.3.1). Temperature profiles of Figure 6.6 are greatly influenced by the value of v_{sat}. If v_{sat} has a small value ($v_{sat} = 5\,\mathrm{ms}^{-1}$), we are imposing that few thermal collisions occur and so few ions are transported. In this situation, a significant quantity of electrical energy (supplied by V_{app}) is converted into random kinetic energy, that is why temperature increases. Viceversa, for high values of saturation velocity ($v_{sat} = 50\,\mathrm{ms}^{-1}$) the temperature rise is greatly lowered. In fact, collisions are of such a short duration that ions do not have enough time to accumulate thermal energy. The transport process in enhanced, and ions have a higher translational velocity. The highest translational velocity occurs in the limiting case of the DD/PNP model, which corresponds to the case of infinite thermal collisions ($v_{sat} \to +\infty$), see velocity profiles for

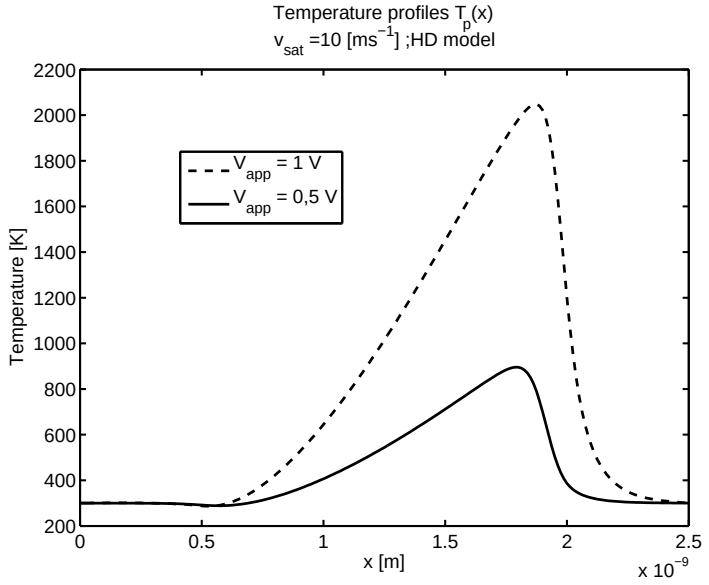

Figure 6.7: Extreme tempreature $T_p(x)$ rise when 0.5 V (solid) and 1 V (dashed) transmembrane potentials are applied.

different values of v_{sat} in Figure 6.8.

I-V curves From these latter observations, we deduce that an increase in temperature profile is accompanied by a slower transport process of ions crossing the channel. As a consequence, the overall current that flows through the channel is reduced. Figure 6.9 shows the I-V curve obtained from different values of v_{sat}. The DD/PNP model predicts the highest current, while the current computed from the HD model becomes smaller for decreasing values of v_{sat} due to temperature rise.

Another fundamental aspect to be considered, is that temperature rise is an electrically dominated process. In fact, if we use a *uniform* permanent charge profile, the variation of electric field is much reduced. Consequentely, the acceleration of ions is greatly reduced, and so is the temperature rise, see Figure 6.10.

Convective terms We now investigate the contribution of the convective terms by studying the influence of λ_ν (see (3.27)) in computing the current denisty J_ν, and by studying whether the kinetic energy $W_{kin} = \frac{1}{2} m_\nu^* v_\nu^2$ is a substantial part of the total energy $W_{tot} = W_{kin} + \frac{3}{2} k_B T_\nu$ or not.

In all our computations, under a wide range of conditions, we have

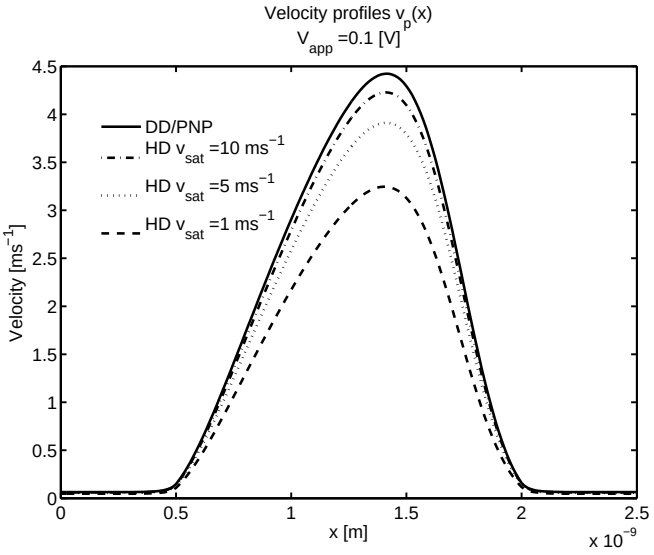

Figure 6.8: Velocity profiles $v_p(x)$ of sodium ions along the channel when $V_{app} = 0.1\,\mathrm{V}$. The solid curve is from DD model; the others are the results of the HD model with different values of v_{sat}.

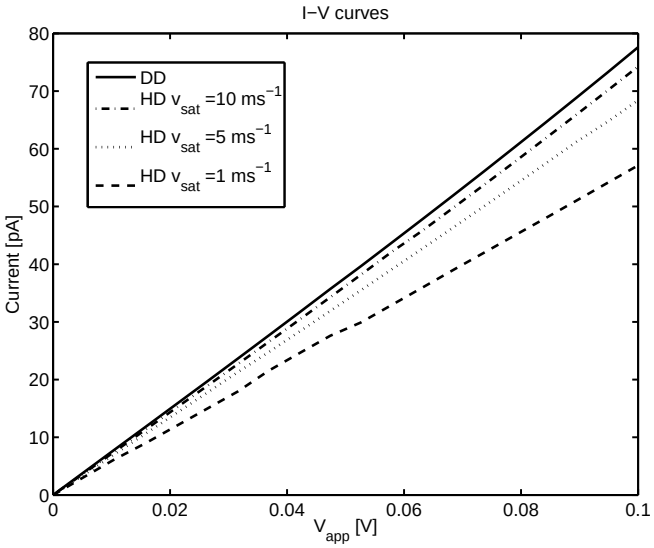

Figure 6.9: Comparison of IV curves from DD model (solid) and HD model (others). With the increase of the value of v_{sat} IV curves moves from the underdamped limit, passing through the intermediate regime, to the overdamped limit predicted by DD model. The current I is in pA.

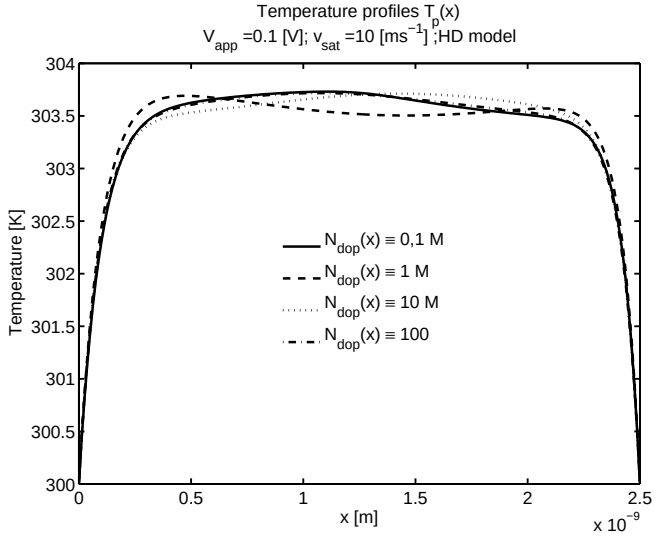

Figure 6.10: Temperature profiles $T_p(x)$ with *uniform* permanent charge profile of 0.1 M, 1 M, 10 M and 100 M.

numerically verified that, at the end of the iterative procedure, the coefficient λ_p is quite small, about 10^{-5} and also the ratio W_{kin}/W_{tot} resulted to be very small, around 10^{-4}. Altogether, these observations allow us to conclude that the convective terms play a minor role in affecting the system dynamics, and they may be neglected without substantial loss of modeling accuracy.

6.4.2 THD model

In this section we investigate if the addition of an explicit equation for water temperature T_L gives different results with respect to the HD model, in which T_L is assumed to be constant.

Computations with the THD model showed potential, electric field, and concentrations profiles very similar to those of HD and DD/PNP models, so that they are not reported below.

Temperature profiles From our calculations we can see that, under similar range of conditions as in Section 6.4.1, water temperature T_L varies usually less than 1 degree, as can be seen Figure 6.11. This is due to the fact that, in the case of water, the sole source term is the thermal energy of ions, and this energy is dominated by the diffusive flux. In fact, the thermal conductivity of water κ_L, whose value is much larger than the thermal

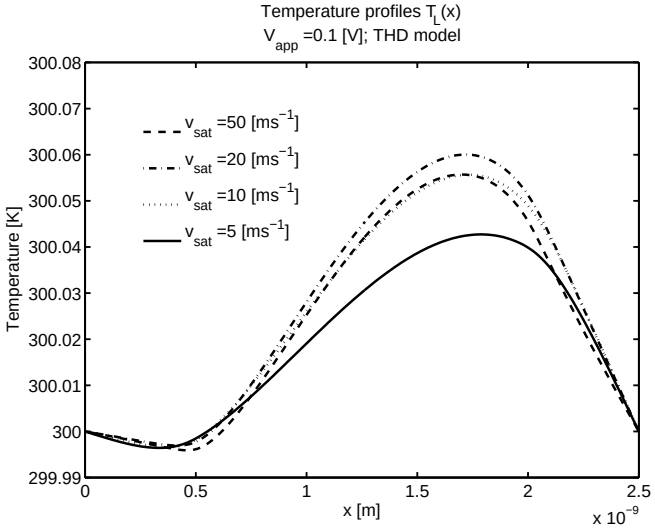

Figure 6.11: Water temperature profiles $T_L(x)$ for differente values of v_{sat}. Variations are less than 1 degree.

conductivity of ions κ_ν ($\kappa_L = 0.6\,\mathrm{Wm^{-1}K^{-1}}$, $\kappa_p \simeq 0.0012\,\mathrm{Wm^{-1}K^{-1}}$, $\kappa_n \simeq 10^{-7}\,\mathrm{Wm^{-1}K^{-1}}$), attenuates temperature changes. To confirm this conclusion, we plot temperature profiles for different values of κ_L in Figure 6.12 and we see that smaller values of κ_L are accompanied by higher variations of T_L. When $\kappa_L = 0.6\,\mathrm{Wm^{-1}K^{-1}}$, it seems that remarkable temperature changes occur only at large bias V_{app}, see Figure 6.13. In this case, the extreme increment of thermal energy of ions due to high electrical forces is enough to increase T_L of some degrees.

I-V curves From these latter observations, we do no expect significant variations in the I-V curves with respect to the HD case. In Figure 6.14, we plot the absolute percentage variation of current $I_{\%}$ in the range $V_{app} = [0, 0.5]\,\mathrm{V}$

$$I_{\%} := \frac{|I_{THD} - I_{HD}|}{I_{HD}} * 100. \tag{6.12}$$

where I_{THD}, I_{HD} are the currents computed by the THD model and the HD model respectively, at the same potential V_{app}. Variations are completely negligible.

We conclude that, in the case of water, the diffusive flux dominates over reacting terms and that the small variations in temperature T_L do not affect the system behaviour appreciably with respect to the HD case.

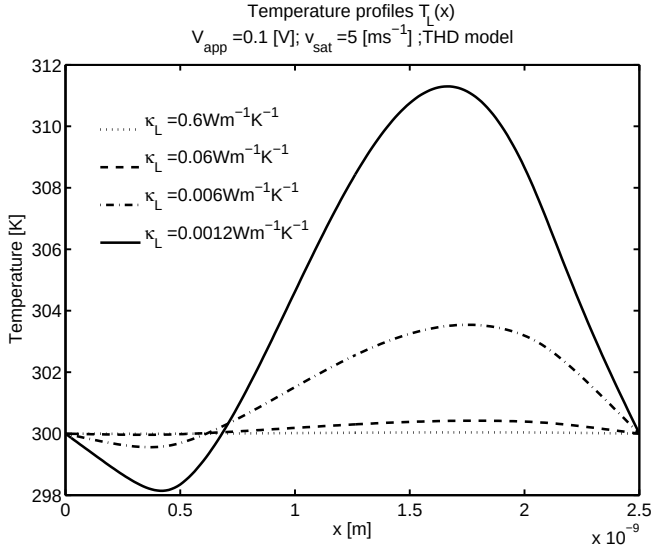

Figure 6.12: Water temperature profile $T_L(x)$ for different values of κ_L. Dotted line is the value in bulk solution ($\kappa_L = 0.6\,\mathrm{Wm^{-1}K^{-1}}$). For smaller values, the temperature rise reaches some degrees.

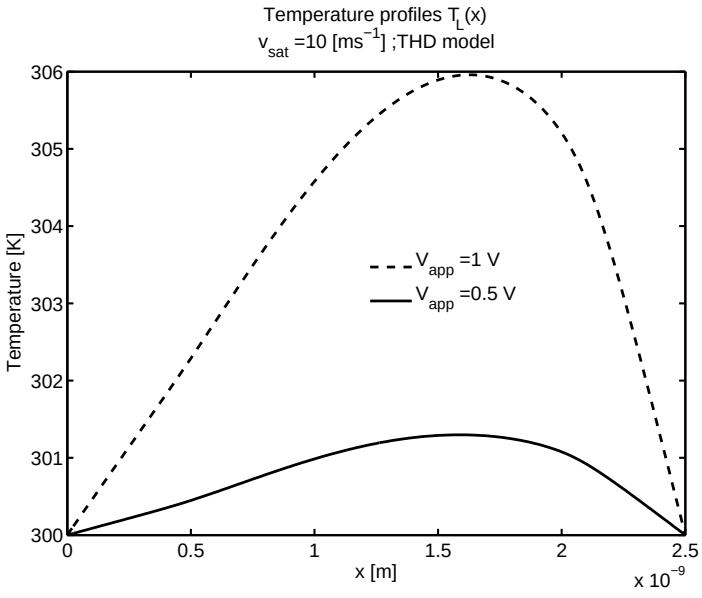

Figure 6.13: Water temperature profile $T_L(x)$ for extreme biases when $\kappa_L = 0.6\,\mathrm{Wm^{-1}K^{-1}}$.

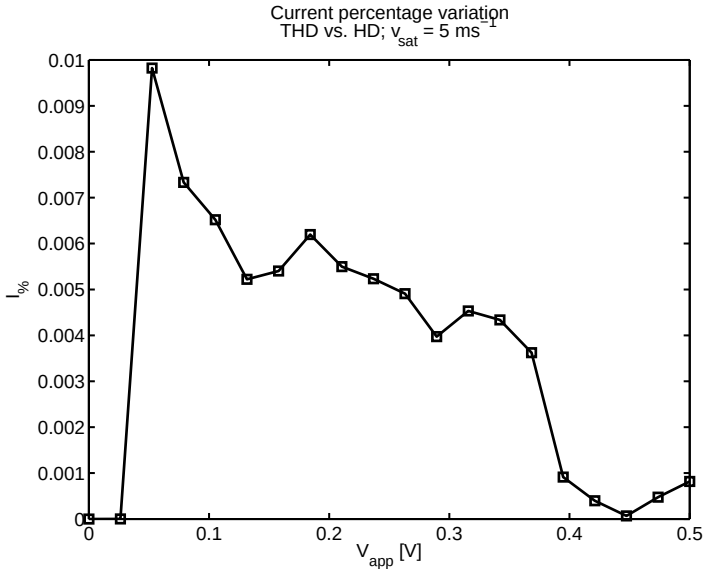

Figure 6.14: Percentage variation of current computed by the THD model with respect to that computed by the HD model. Applied biases range in the interval $[0, 0.5]$ V.

6.4.3 ET model

The ET model is an extension of the DD/PNP model that prescribes a unique temperature $T = T(x)$ for ions and water. Figure 6.15 shows temperature profile for different values of V_{app}. The Joule heating term $\mathbf{E}\cdot\mathbf{J}_{tot}$ may substantially modify the temperature profile T in the case of large external potential V_{app}. However, in the range of realistic operating biases $[-0.1, +0.1]$ V, similar arguments as in Section 6.4.2 about the diffusion coefficient $\kappa_{tot} \simeq \kappa_L$, lead to the conclusion that temperature rise is attenuated by the diffusive process.

As a consequence, the I-V curves of the ET model resemble those predicted by the DD/PNP model. The percentage variation of current between the ET and DD/PNP models is shown in Figure 6.16, and it is always less than 1% in all the considered range of V_{app}.

6.4.4 Conclusions

The results obtained in the extensive simulations performed in this section demonstrate that model and methodologies proposed in the present thesis are in very good agreement with those reported in [24]. More specifically, we observe that in the gramicidin-A channel, it is possible that substantial

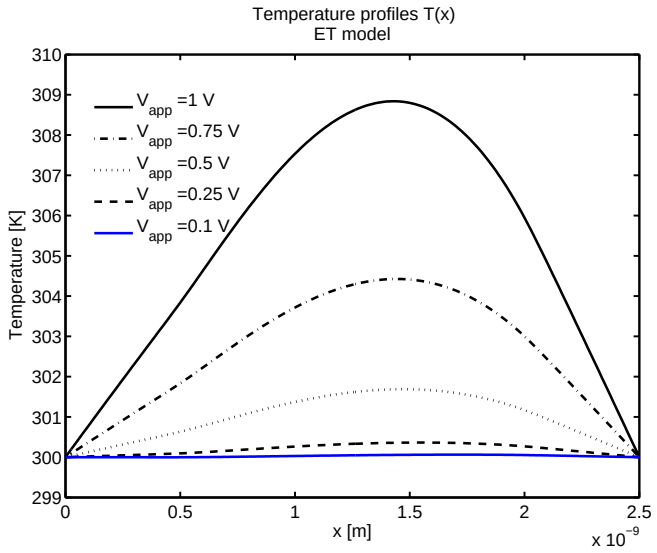

Figure 6.15: Temperature profile $T(x)$ from the ET model for different V_{app}.

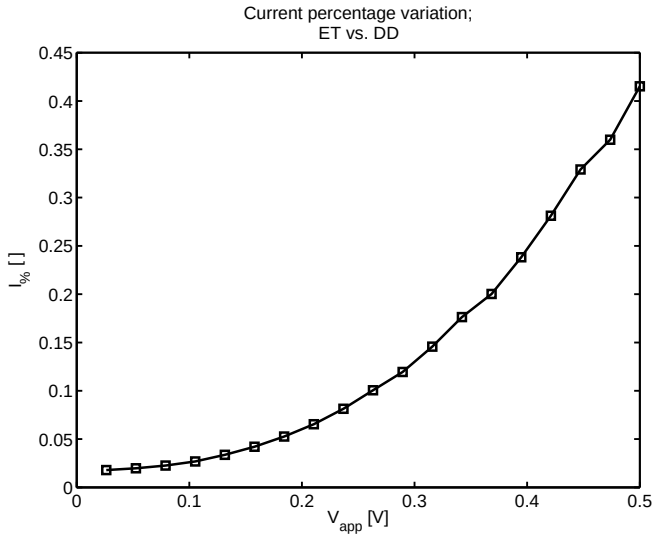

Figure 6.16: Percentage variation of current computed by the ET model with respect to that computed by DD model. Applied biases range in the interval $[0, 0.5]$ V.

Table 6.3: CRC channel data. Diffusion coefficients are in $\times 10^{-9}\,\mathrm{m^2 s^{-1}}$

L [nm]	a [nm]	$C_{\mathtt{L}}, C_{\mathtt{R}}$ [mM]	D_{K^+}	D_{Cl^-}	V_{app} [V]
1	0.35	$25 \div 2000$	0.125	0.387	± 0.15

temperature changes accompany ion permeation, under a wide range of conditions. If ion temperature rise is large enough, the current through the channel is significately reduced. Such results depend strongly on the parameter saturation velocity v_{sat}.

Water temperature variations are very small both in the THD and in the ET model, and thus T_L can be held to a constant value without significantly affecting simulation results.

6.5 Calcium Release Channel (CRC)

The calcium release channel (CRC) of the sarcoplasmic reticulum is a high-conductance channel that selects cations over anions (the conductance is the slope of the current-voltage relation). The CRC has been the object of extensive experimentation (see [21, 23, 22] and references therein) due to its central role in the activation of contraction in the cardiac muscle. The CRC channel is permeable to the monovalent cations Li^+, K^+, Na^+, Rb^+, and Cs^+. Our computations were executed in KCl solutions. Although Ca^{2+} movement through CRC is of the greatest importance, we choose to use K^+ as the main current carrier (as done in [21]) because calcium ions have complex effects on both ion permeation and membrane voltage gating.

In this section we aim to compare temperature changes and I-V relations from the THD model and the DD model, measured in symmetrical and asymmetrical bulk solutions. Our goal is to investigate if the THD model predicts a different behaviour of the system with respect to the DD model.

The CRC channel is simply described by a constant fixed charge profile $N_{dop}(x) \equiv -4.2\,\mathrm{M}$, which is reported in Figure 6.17. In Table 6.3 we summarize channel geometry, coefficient values and the typical ranges of working conditions.

Remark 6.2. We carried out simulations with both ions K^+ and Cl^-. However, the concentration of counterions is so small that it does not influence appreciably the system. So, for ease of presentation, we plot and discuss only physical quantities referred to ion K^+.

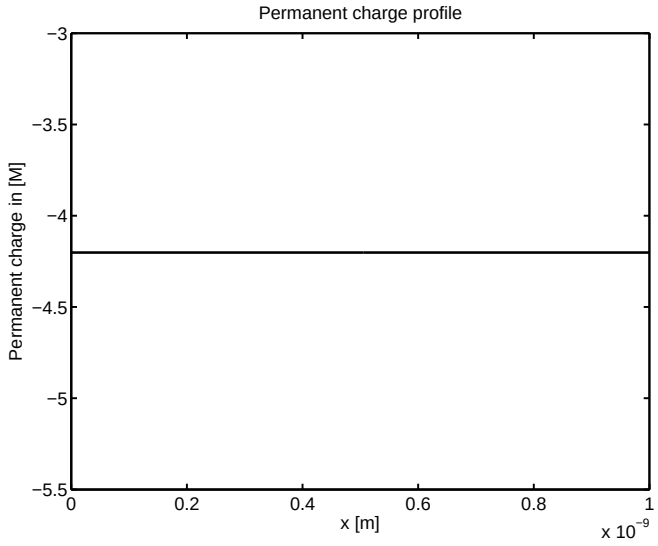

Figure 6.17: The permanent charge profile is uniform and equal to $-4.2\,\mathrm{M}$.

6.5.1 THD model

Temperature profiles The temperature profile $T_p(x)$ is influenced by the value of saturation velocity, as can be seen in Figure 6.18.

The temperature profile is also influenced by different bulk concentrations. In Figure 6.19, we show temperature profiles with the same values of v_{sat} as in Figure 6.18, but with $C_{\mathtt{L}} = 2\,\mathrm{M}$ and $C_{\mathtt{R}} = 0.25\,\mathrm{M}$. The different concentrations among the two baths ($C_{\mathtt{L}} > C_{\mathtt{R}}$) enhances the diffusion process of K^+ ions from left to right and so current J_p is increased (when $V_{app} > 0$). The higher value of electrical energy EJ_p (Joule heating) causes higher temperature rise. Conversely, when $C_{\mathtt{L}} < C_{\mathtt{R}}$, K^+ ions tend to diffuse from right to left, in opposition to the external bias $V_{app} > 0$, so that temperature rise is more modest, see Figure 6.20.

I-V curves I-V curves comparison between DD and THD model for different values of v_{sat} are shown in Figure 6.21. For small values of v_{sat}, the transport process of ions K^+ is reduced because part of the electrical energy is converted into ion thermal energy. The current that passes through the channel is then reduced. In order to quantify these changes, in Figure 6.22 we report current percentage variation $I_{\%}$. The maximum variation is about 10% and it occurs at $v_{sat} = 1\,\mathrm{ms}^{-1}$ and $V_{app} = 0.15\,\mathrm{V}$.

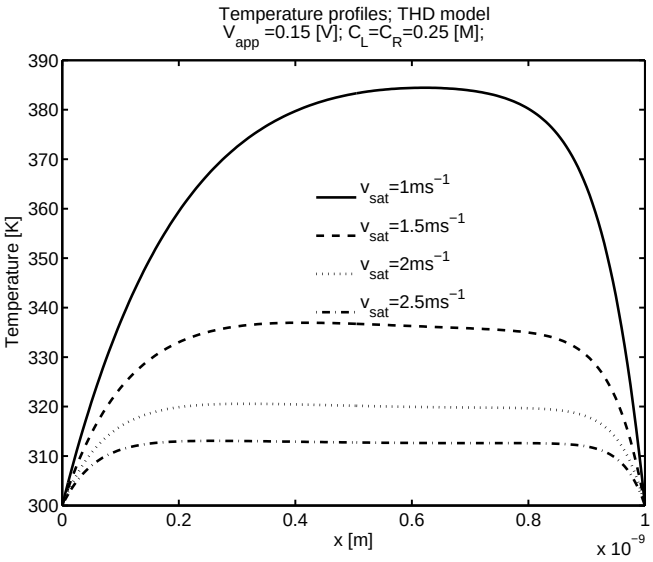

Figure 6.18: Temperature profile $T_p(x)$ for different values of v_{sat}, equal bulk concentrations $C_{\mathtt{L}} = C_{\mathtt{R}} = 0.25\,\mathrm{M}$ and $V_{app} = 0.15\,\mathrm{V}$. As v_{sat} decreases, temperature rise increases.

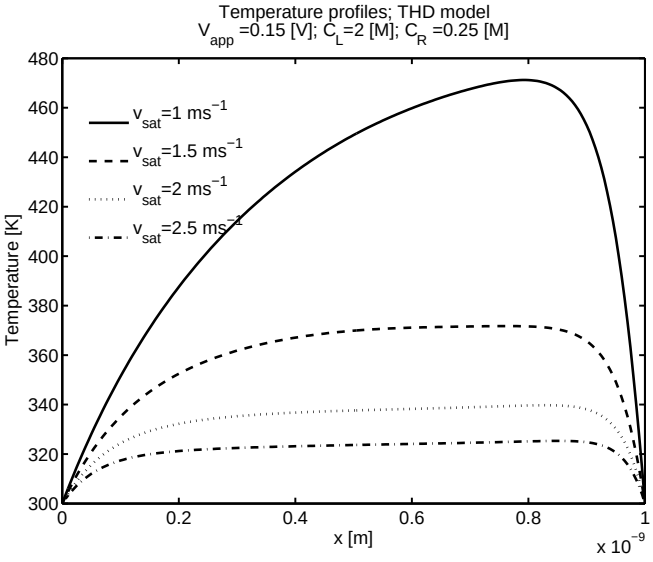

Figure 6.19: Temperature profile $T_p(x)$ for different values of v_{sat}, with bulk concentrations $C_{\mathtt{L}} = 2\,\mathrm{M}, C_{\mathtt{R}} = 0.25\,\mathrm{M}$ and $V_{app} = 0.15\,\mathrm{V}$. As v_{sat} decreases, temperature rise is becomes larger.

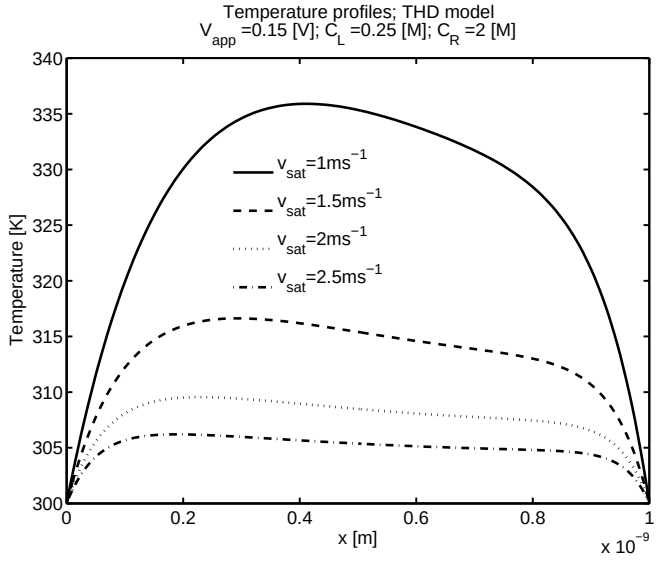

Figure 6.20: Temperature profile $T_p(x)$ for different values of v_{sat}, with bulk concentrations $C_{\mathtt{L}} = 0.25\,\mathrm{M}, C_{\mathtt{R}} = 2\,\mathrm{M}$ and $V_{app} = 0.15\,\mathrm{V}$. As v_{sat} decreases, temperature rise is becomes larger.

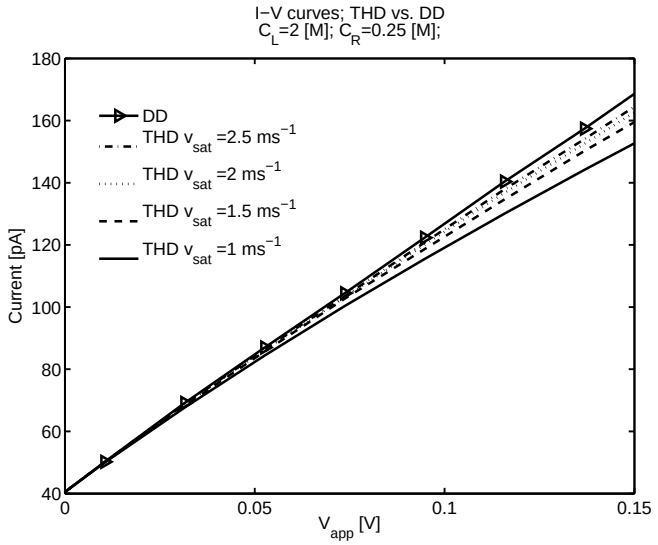

Figure 6.21: Comparison of IV curves from DD model (solid line with ▷) and THD model (other lines) for different values of v_{sat}. $C_{\mathtt{L}} = 2\,\mathrm{M}, C_{\mathtt{R}} = 0.25\,\mathrm{M}$. The current I is measured in pA.

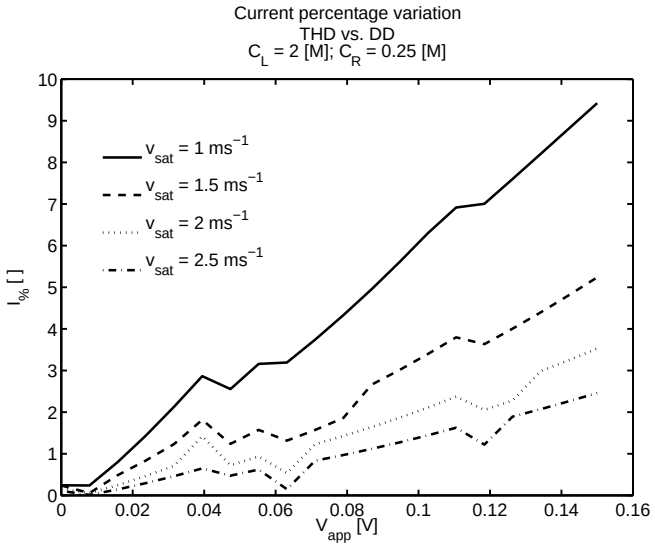

Figure 6.22: Percentage variation of current I_{THD} with respect to I_{DD} for different values of v_{sat}.

Water temperature In all our numerical simulations, water temperature $T_L(x)$ resulted to be almost constant. Variations with respect to reference temperature T_0 are very small (about 0.1 K or less). Even with extreme external bias of 1 V or more, variations do not exceed 1 K.

Convective terms and kinetic energy Even in this type of channel, convective terms are negligible. In fact coefficients λ_ν and the ratio W_{kin}/W_{tot} are very small, around $10^{-5} \div 10^{-6}$.

6.5.2 Conclusions

The THD model may predict smaller current flowing through the CRC channel than the DD model. The reduction of current is due to the increment in ion temperature: part of electrical energy supplied to the system is converted into disordered kinetic energy (i.e.: temperature), and consequently the ion translational velocity is reduced. This reduction is more evident for small values of saturation velocity ($v_{sat} = 1 \div 1.5\,\mathrm{ms}^{-1}$), but becomes negligible for greater values ($v_{sat} = 2 \div 2.5\,\mathrm{ms}^{-1}$). In this latter case the THD model gives almost the same results as the DD model. Unfortunately, literature lacks of precise values of v_{sat} in the case of biological channels and so, the necessity of a manual tuning of v_{sat} limits conclusions we can reach.

Table 6.4: Bipolar nanofluidic diode data. Diffusion coefficients are in $\times 10^{-9}\,\mathrm{m^2 s^{-1}}$

L [nm]	a [nm]	$C_{\mathtt{L}}, C_{\mathtt{R}}$ [M]	D_{K^+}	D_{Cl^-}	V_{app} [V]
1000	4	0.1	2	2	± 1

Water temperature changes predicted from THD model do not appreciably affect current measurements or any other physical quantity and so the water heat flow equation may be dropped, thus reducing the THD model to the simpler HD model without significant loss of information.

6.6 Bipolar nanofluidic diode

In this section we aim to study the performance of our computational model for ion transport in the simulation of a *bipolar synthetic nanochannel* with cylindrical shape, see e.g. [101, 102]. The nanochannel is bathed in KCl solution. Channel size and other input data are listed in Table 6.4. If not otherwise stated, those are the values used in the numerical computations.

The bipolar diode has two segments in the nanochannel with surface charges of the opposite sign and the same charge density, which is equal to $\sigma = 0.5q$ (units $\mathrm{C\,nm^{-2}}$). The first half of the channel is negatively charged $(-\sigma)$, the second half is positively charged $(+\sigma)$. Using relation (6.2), we get the profile $N_{dop}(x)$ of Figure 6.23. The asymmetrical surface charge distribution form a junction similar to the *pn* semiconductor diode. In fact, depending on the sign of the applied bias, the device allows the flow of ionic current in one direction, blocking the flow of ions in the other:

- $V_{app} > 0$ is the open state of the diode, or the forward (FWD) bias;
- $V_{app} < 0$ is the closed state of the diode, or the reverse (REV) bias.

Figures 6.24 and 6.25 show the ionic concentration for FWD and REV bias, respectively (calculations were performed by solving the DD model. Other models give very similar output). As expected, the FWD bias causes an enhancement of K^+ and Cl^- concentrations inside the pore, while the REV bias produces very low ionic concentrations near $x = L/2$, effectively leading to the formation of a depletion zone. The electric potential profile for FWD an REV bias is shown in Figure 6.26.

Rectification factor The quality of an ionic diode performance can be described by the *rectification factor* Q, calculated as the ratio of current

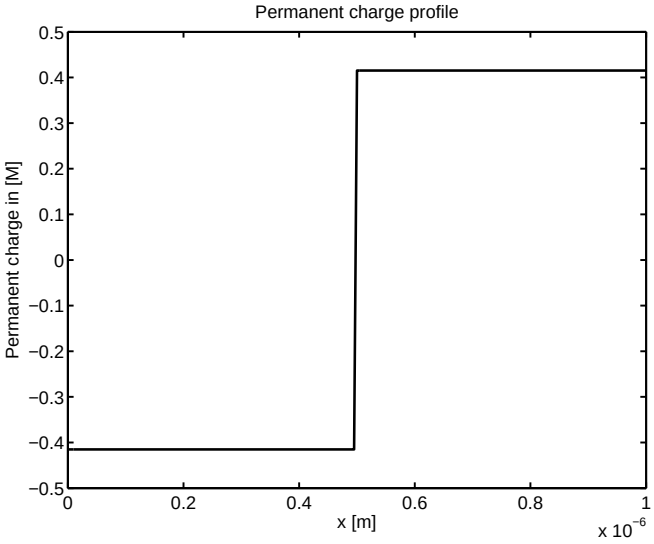

Figure 6.23: Permanent charge profile $N_{dop}(x)$. The value on the left is $-0.41\,\mathrm{M}$, that on the right $+0.41\,\mathrm{M}$. The junction between the two parts is located at mid channel $L/2$.

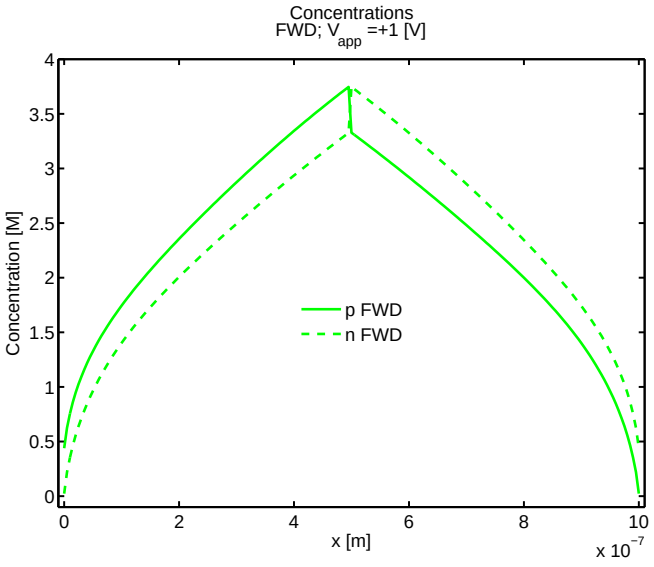

Figure 6.24: Profiles of ion concentrations at FWD bias ($V_{app} = 1\,\mathrm{V}$). Solid line is K^+, dashed line is Cl^-.

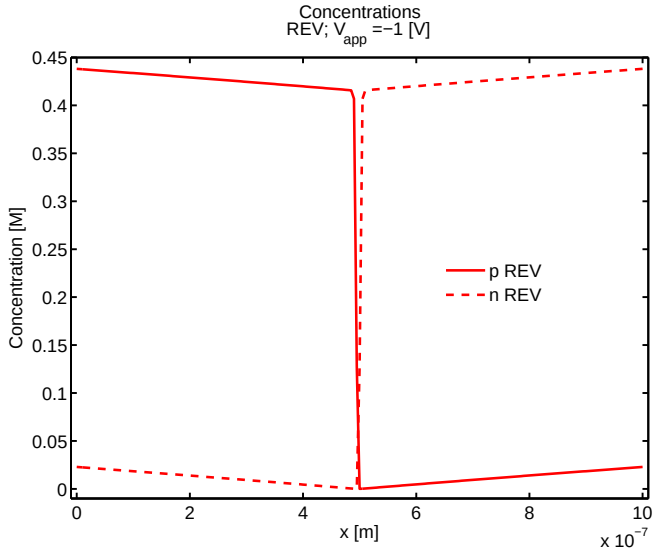

Figure 6.25: Profiles of ion concentrations at REV bias ($V_{app} = -1\,\mathrm{V}$). Solid line is K^+, dashed line is Cl^-.

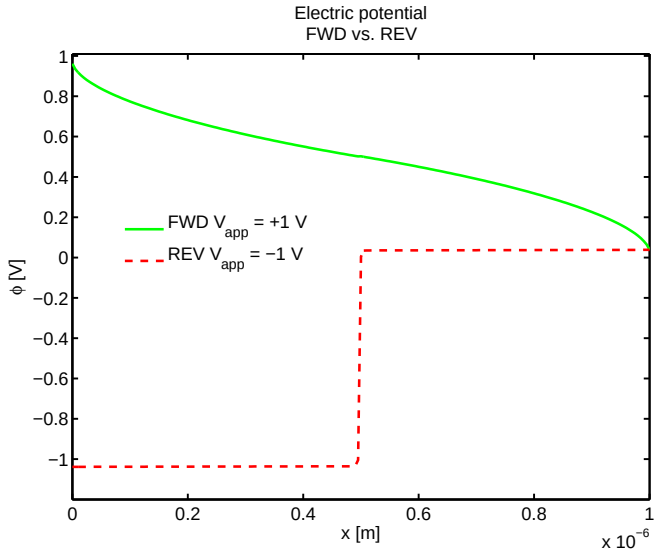

Figure 6.26: Electric potential profile $\phi(x)$ for FWD (green solid) and REV (red dashed) state.

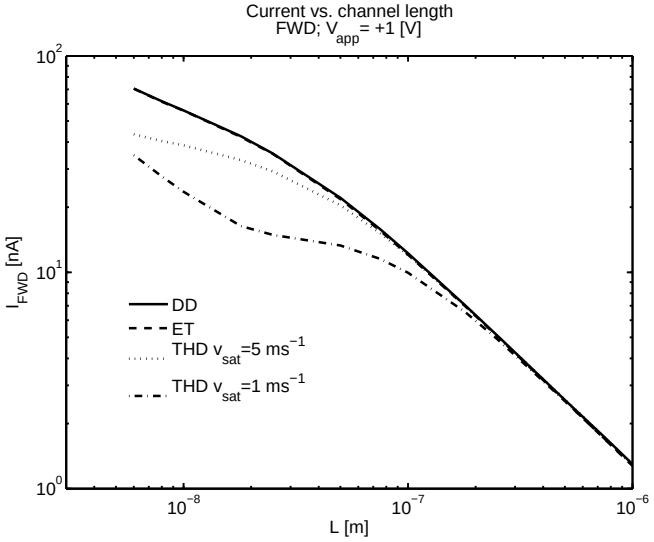

Figure 6.27: Current I_{FWD} (in [nA]) at open state ($V_{app} = 1\,\mathrm{V}$) as a function of nanochannel length. Different lines are from different models: DD, ET and THD.

measured at opposite voltages of the same magnitude

$$Q := \frac{I_{FWD}(V_{app})}{|I_{REV}(-V_{app})|}. \tag{6.13}$$

Higher values of $Q(V_{app})$ correspond to better diode performance.

6.6.1 Current vs. channel length

We compute currents I_{FWD} and I_{REV} at $|V_{app}| = 1\,\mathrm{V}$ varying channel length from 6 to 1000 nm, with DD, ET and THD model (for $v_{sat} = 1\,\mathrm{ms}^{-1}$ and $v_{sat} = 5\,\mathrm{ms}^{-1}$). Results are shown in Figures 6.27 and 6.28, respectively. The associated rectification factor Q is reported in Figure 6.29.

From those figures, we can see that the ET model does not vary with respect to the DD model. Instead, transport properties of ionic diode are slightly different among DD and THD model, especially when $v_{sat} = 1\,\mathrm{ms}^{-1}$ and channel length L is small. This result is not surprising, since in shorter channel the electrical energy is higher, at the same V_{app}.

6.6.2 Current vs. channel radius

We have computed I_{FWD}, I_{REV} adn $Q(V_{app})$ for $|V_{app}| = 1\mathrm{V}$ varying channel radius from 1 to 13 nm, with DD, ET and THD model (for $v_{sat} = 1\,\mathrm{ms}^{-1}$ and

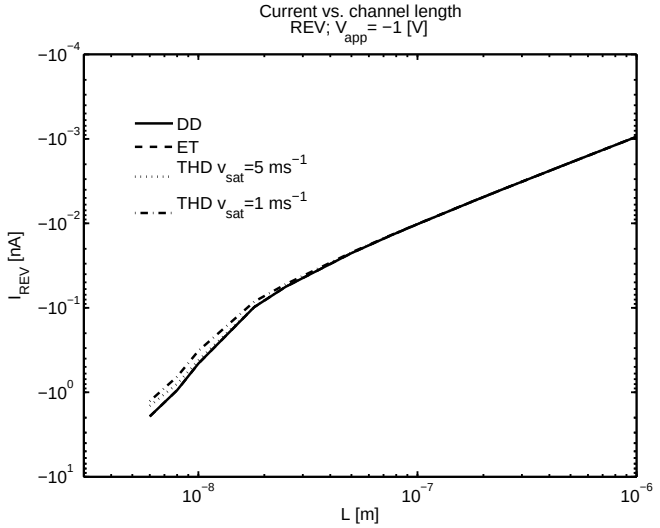

Figure 6.28: Current I_{REV} (in [nA]) at closed state ($V_{app} = -1\,\mathrm{V}$) as a function of nanochannel length. Different lines are from different models: DD, ET and THD.

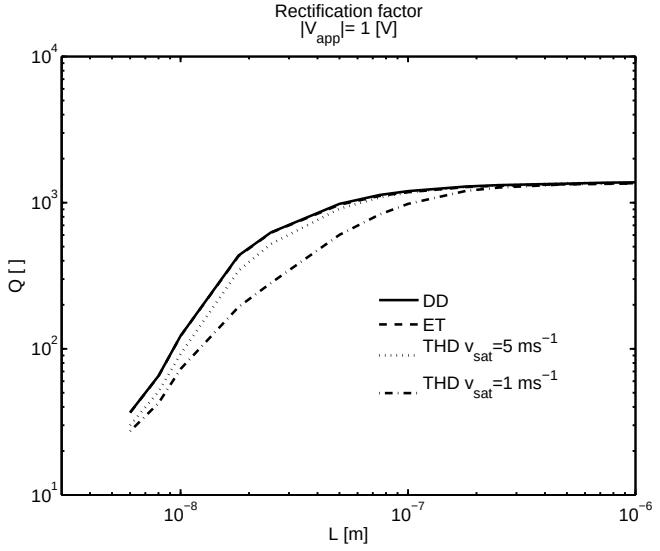

Figure 6.29: Rectification factor $Q(V_{app})$ ($|V_{app}| = 1\,\mathrm{V}$) as a function of nanochannel length. Different lines are from different models: DD, ET and THD.

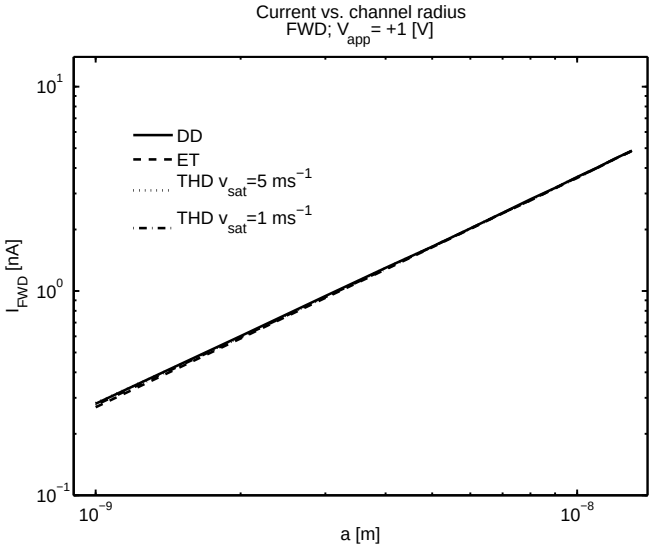

Figure 6.30: Current I_{FWD} (in [nA]) at open state ($V_{app} = 1\,\mathrm{V}$) as a function of nanochannel radius. Different lines are from different models: DD, ET and THD.

$v_{sat} = 5\,\mathrm{ms}^{-1}$). Results are shown in Figures 6.30, 6.31 and 6.32, respectively. All the models studied give very similar outputs.

At open state ($V_{app} > 0$), we can see that current I_{FWD} increases with radius a. The enhancement in current is due to the larger area of the channel. As can be seen in in Figure 6.30, current I_{FWD} increases linearly with respect to a. Since $I_{FWD} = J_{FWD}A$, there must be an inverse proportionality relation between J and a. From numerical results we have indeed verified that $J_{FWD}(a) \sim a^{-0.88}$. This latter dependece can be explained considering that the permanent charge is less effective in attracting ion when radius increases, see (6.2).

An increased channel radius a causes higher current also at closed state ($V_{app} < 0$). However, in this case there is a direct proportionality relation between J_{REV} and a. From numerical results, we have obtained $J_{REV}(a) \sim a^{1.002}$. This different behaviour is explained by noticing that K^+ ions enter more easily into the channel when a is increased because the repulsion exherted by the the positive permanent charge is less strong. A similar reasoning holds for Cl^- ions.

Obviously, the rectification factor decreases as $Q(a) \sim a^{-1.882}$.

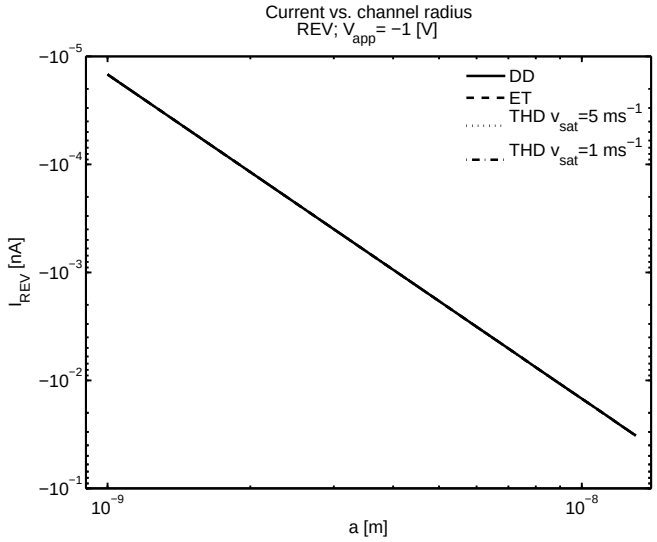

Figure 6.31: Current I_{REV} (in [nA]) at closed state ($V_{app} = -1\,\mathrm{V}$) as a function of nanochannel radius. Different lines are from different models: DD, ET and THD.

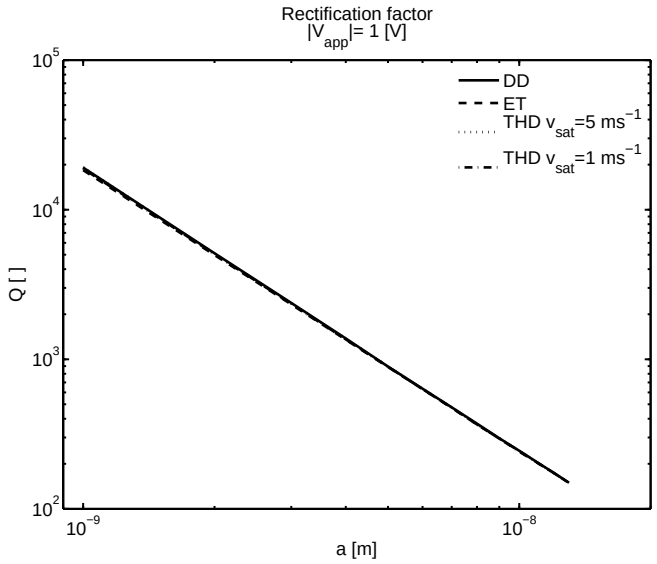

Figure 6.32: Rectification factor $Q(V_{app})$ ($|V_{app}| = 1\,\mathrm{V}$) as a function of nanochannel radius. Different lines are from different models: DD, ET and THD.

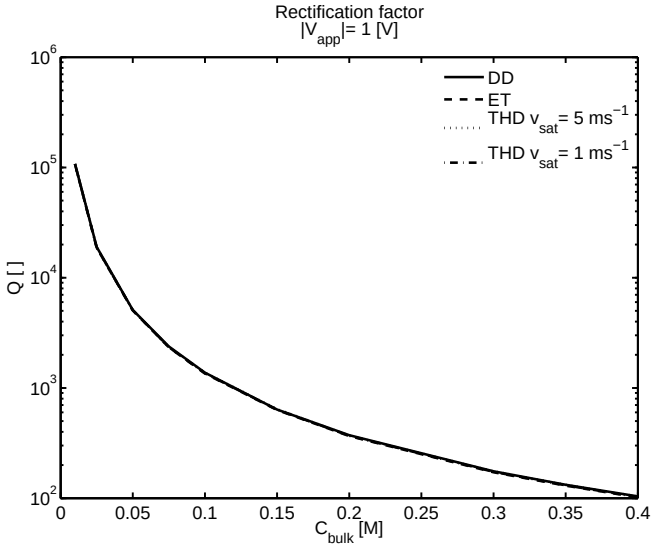

Figure 6.33: Rectification factor $Q(V_{app})$ ($|V_{app}| = 1\,\mathrm{V}$) as a function of bath concentration C_{bulk}. Different lines are from different models: DD, ET and THD.

6.6.3 Current vs. bulk concentration

We have computed I_{FWD}, I_{REV} adn $Q(V_{app})$ for $|V_{app}| = 1\mathrm{V}$ varying baths concentration C_{bulk} from 0.01 to 0.4 M, with DD, ET and THD model (for $v_{sat} = 1\,\mathrm{ms}^{-1}$ and $v_{sat} = 5\,\mathrm{ms}^{-1}$). We have obtained almost identical results, as can be seen from the rectification factor Q if Figure 6.33

6.6.4 I-V curves

In Figure 6.34 are illustrated I-V curves computed by using DD, ET, THD ($v_{sat} = 1\,\mathrm{ms}^{-1}$ and $v_{sat} = 5\,\mathrm{ms}^{-1}$) models. Once again, models give almost identical results.

6.6.5 Boundary layers

In all our simulations with different models we have noticed the presence of significant boundary layers in almost all physical quantities: concentrations, electric field, drift velocities and ion temperatures. The presence of such boundary layers occurs at any value of applied bias $V_{app} > 0$, saturation velocity v_{sat}, channel length L, channel radius a, bulk concentration C_{bulk} and so they seem to be an intrinsic feature of the channel investigated in the present section. In Figures 6.35a and 6.35b we show the electric field

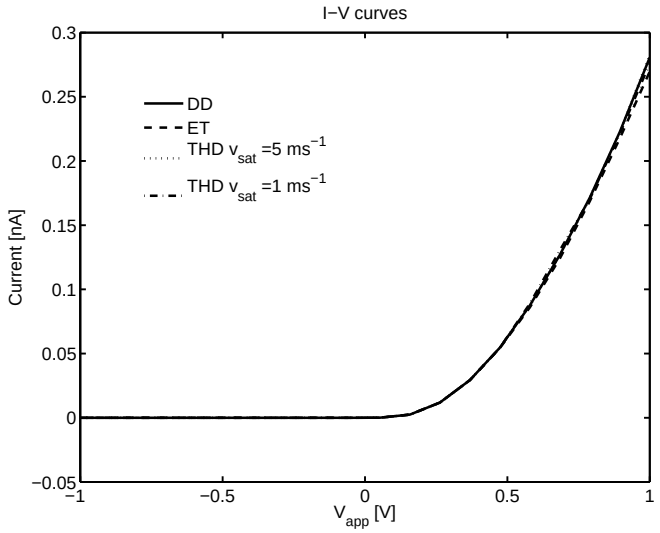

Figure 6.34: I-V curves. Different lines are from different models: DD, ET and THD.

and velocity profiles with $V_{app} = 1\,\mathrm{V}$ computed from the DD model in order to show that boundary layers are present even in the simplest model and under normal operating bias. It is then not surprising that ion temperature profiles from THD and HD models exhibit similar behaviour at boundaries, see Figures 6.35c and 6.35d, the profile in the THD case being concave due to the influence of its coupling with water temperature profile. Notice that the absolute temperature rise at boundaries is small and does not affect appreciably system dynamics of the device, as shown in the I-V graphs as a function of V_{app}, L or a in previous sections.

6.6.6 Conclusions

In our simulations we have changed the shape of the nanopore (length and radius) and bulk concentrations in the baths to see how different models prescribe different diode performance, which is expressed by the rectification factor Q. The profiles of Q obtained from different models are usually very similar. We have found considerable changes only in the case of the THD model with $v_{sat} = 1\,\mathrm{ms}^{-1}$ and small channel length, see Figure 6.29.

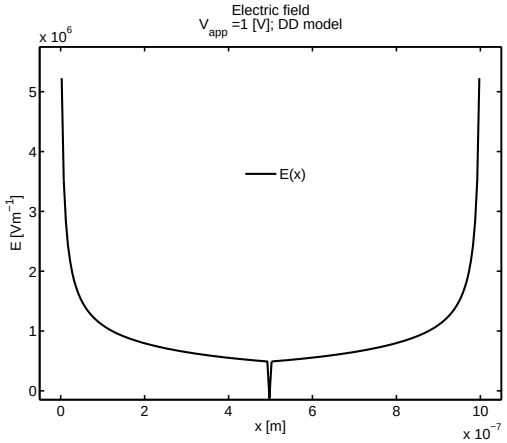

(a) Electric field profile. DD model.

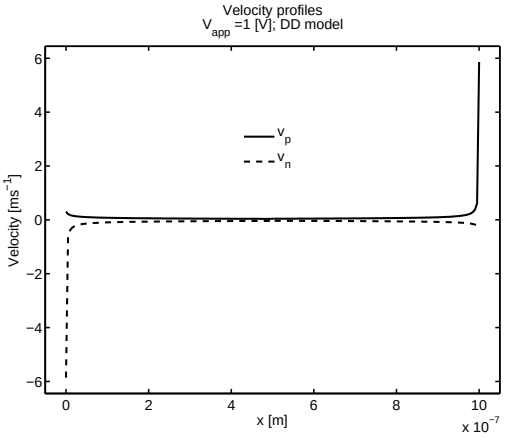

(b) Velocity profiles. DD model.

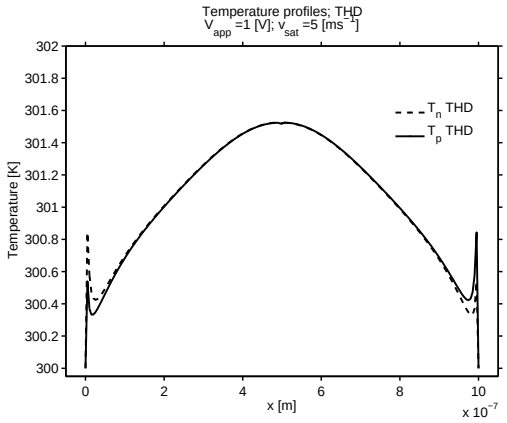

(c) Temperature profiles. THD model

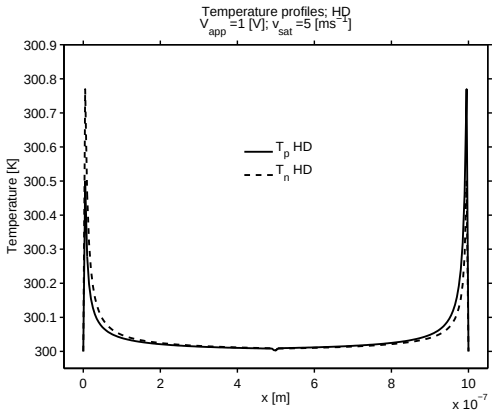

(d) Temperature profiles. HD model

Figure 6.35: Boundary layers in electric field, velocities and ion temperature profiles.

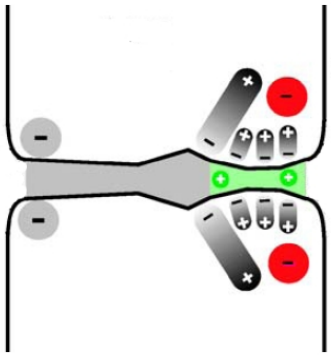

Figure 6.36: Schematic view of K channel. Regions length and charge are detailed in Table 6.5.

6.7 K channel

In this section we focus on another physiologically important channel, the K channel, following [41]. K channels play a central role in electrical signaling in the nervous system. A typical nerve cell has hundreds of thousands of K channels. A schematic view of the geometry of the problem is illustrated in Figure 6.36 (the KcsA channel structure shown is derived from X-ray crystallography).

We consider the flow of K^+ and Cl^- ions in water through a channel of radius $a = 0.5\,\text{nm}$ and length $L = 3.5\,\text{nm}$. The computational domain will also include regions into left and right baths. In the one-dimensional approximation to the K channel problem, the baths are represented by conical funnels extending 5 nm on either side of the channel, see Figure 6.37.

Figure 6.37: Channel plus bath domains. The baths are represented by conical funnels with increasing cross sectional area $A(x)$.

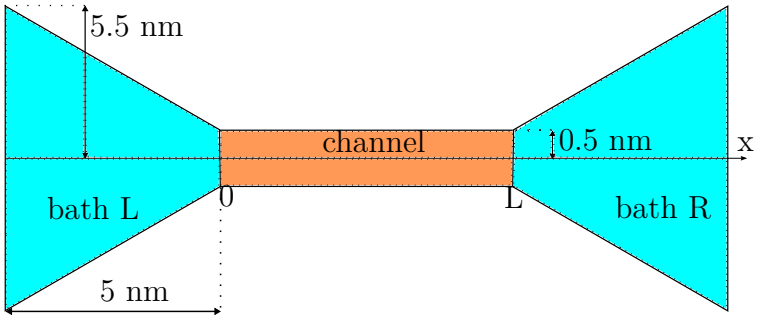

Table 6.5: K channel data. Diffusion coefficients are in $\times 10^{-9}\,\mathrm{m^2 s^{-1}}$.

Region	l[nm]	Q_{bck}[C]	ϵ_r	D_ν
Bath `L`	5.0	0	80	1.5
$-4q$ group	0.2	$-4q$	80	0.4
Non polar	1.1	0	4	0.4
Central cavity	1.0	$-q/2$	30	0.4
Filter	1.2	$-3q/2$	30	0.4
Bath `R`	5.0	0	80	1.5

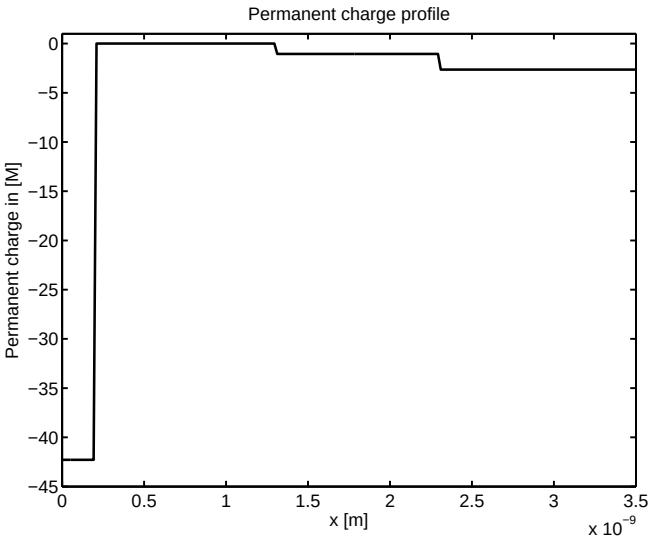

Figure 6.38: Permanent charge profile $N_{dop}(x)$ inside the channel.

For various sections of the channel and surrounding baths, the lengths l, background permanent charge Q_{bck} on the protein, relative dielectric constant ϵ_r and diffusion coefficients D_ν are given in Table 6.5. The fixed charged profile of the protein associated with the charge distribution Q_{bck} of Table 6.5 is shown in Figure 6.38. Ion concentration in baths is equal to $C_{bulk} = 0.15\,\mathrm{M}$ and the typical bias applied across the channel plus baths is $V_{app} = 1\,\mathrm{V}$.

Remark 6.3. We carried out simulations with both ions K^+ and Cl^-. However, the concentration of counterions is so small that it does not influence appreciably the system. So, for ease of presentation, we plot and discuss only physical quantities referred to ion K^+.

6.7.1 Modeling baths

The need of modeling baths is suggested by the fact that, as seen in Section 6.6.5, boundary layers in ionic charge density and electric field may develop at the ends of the channel. By modeling regions outside the channel, we can apply BCs far away from the channel so that physical quantities can reach their equilibrium far-field values.

The funnels that model baths should be wide enough so that the impedance of the baths to the ion flow is very small compared to the impedance of the channel. The cross sectional area $A(x)$ illustrated in Figure 6.37 is constant in the channel but not in the baths. The section radius at bath ends is $a_{bath} = 5.5\,\text{nm}$. In order to account for non-constant cross-sectional area into our 1D approximation we recall the definition of the divergence operator of a vector field $\mathbf{u}$:

$$\operatorname{div}\mathbf{u} := \lim_{\mathcal{V}\to 0} \frac{1}{\mathcal{V}} \int_{\partial\mathcal{V}} \mathbf{u}\cdot\mathbf{n}\, d\sigma \tag{6.14}$$

where $\mathcal{V}$ is a volume centered around $\mathbf{x}$ with bounding surface $\partial\mathcal{V}$. In 1D $\mathcal{V} = A(x)dx$ and (6.14) reduces to

$$\begin{aligned} \operatorname{div}\mathbf{u} &= \lim_{dx\to 0} \frac{1}{A(x)dx}\left[u(x+dx)A(x+dx) - u(x)A(x)\right] \\ &= \frac{1}{A}\frac{\partial}{\partial x}(Au). \end{aligned} \tag{6.15}$$

Whenever the divergence operator appears in any mathematical model, relation (6.15) must be used. In the remainder of this section we consider DD and ET models with this modification.

6.7.2 DD vs. ET

As a general statement, we notice that the DD and ET simulations produce completely similar results for this specific channel, see Figure 6.39. We can see that boundary layers develop at channel openings $x = 0$ and $x = 3.5\,\text{nm}$. The computed I-V curves are shown in Figure 6.40. All the reported results are in good agreement with [41].

Figure 6.41 shows water temperature profiles computed with different values of V_{app}. The absolute increment is very small, demonstrating that in the present situation the use of higher-order descriptions is unnecessary.

6.7.3 Conclusions

The addition of two sections at either side of the channel modeling baths should be adopted whenever possible because it allows the solution to develop

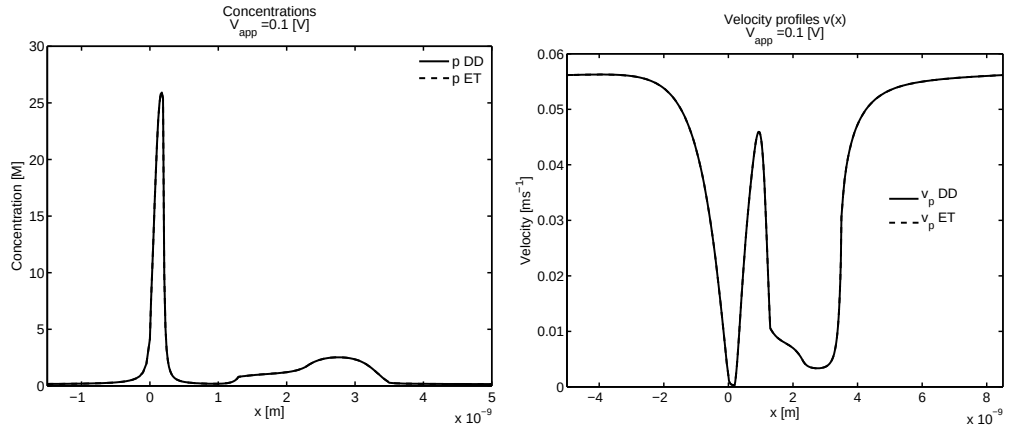

(a) Concentration. **(b)** Velocity.

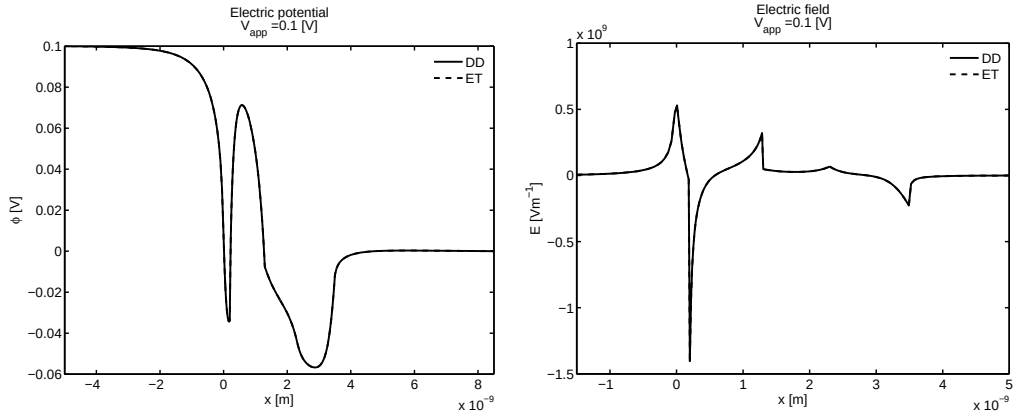

(c) Electric potential. **(d)** Electric field.

Figure 6.39: Concentration, velocity, potential and electric field profiles from DD and ET models. DD and ET models provide completely similar solutions.

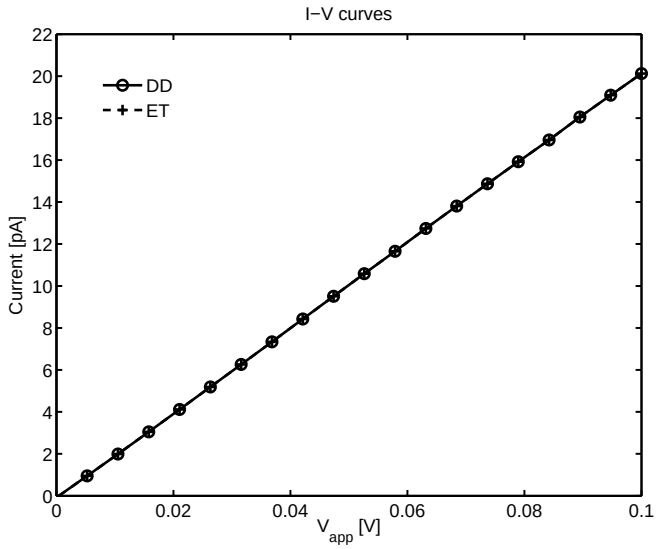

Figure 6.40: I-V curves from DD and ET models. Current is in pA.

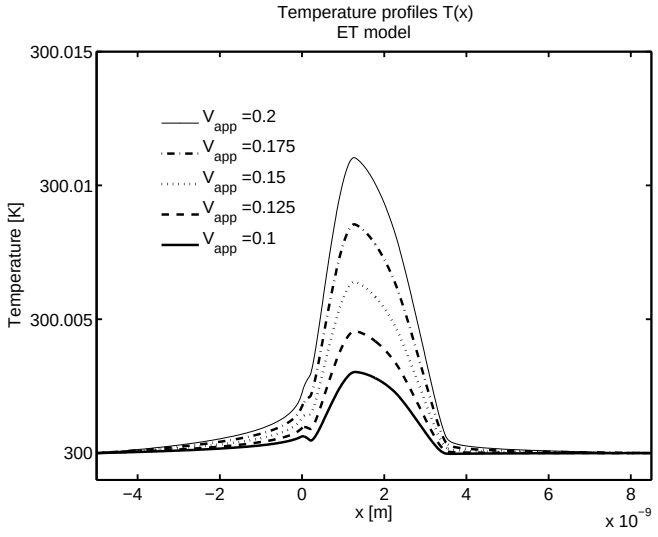

Figure 6.41: Water temperature computed from the ET model for different values of V_{app}. Temperature changes are very small.

more realistically at channel ends, since it is not forced to satisfy Dirichlet BCs at those points.

Chapter 7

Conclusions and Perspectives

In this concluding chapter, we provide a comment to the main results obtained in the thesis work and address possible future directions for next research.

7.1 General conclusions

In the thesis, a hierarchy of energy-dependent models for ion transport in biological and synthetic nanochannels has been proposed and numerically investigated.

Results indicate that temperature changes affect ion permeation in the nanochannels studied here, with particular impact in the case of the Gramicidin-A channel. This conclusion agrees well with the analogy between this type of channel and the so-called "ballistic diode", which is a typical example of semiconductor device where significant non-equilibrium effects are well-known to play a major role in determining device performance.

In all the other investigated channel structures, it is fair to observe that temperature changes, despite being visible, are usually relatively small with respect to the isothermal reference configuration, so that they do not influence current flow appreciably.

As a general comment, it is worth noting that the computed results depend strongly on the parameter v_{sat} which can affect system behaviour with respect to heat changes since it prescribes the collision frequency of ions. More precisely, a high value of v_{sat} leads the system to the overdamped limit (DD model), which corresponds to assuming constant temperature in the channel. Lack of information about a quantitative characterization of the parameter v_{sat} is a substantial limitation of the present analysis and deserves further experimental investigation and subsequent model calibration.

Besides temperature changes, we have also analyzed the effect of nonlinear

convective terms that are accounted for by the THD and HD models. In all simulated cases (except for the K-channel where the THD and HD models have not been verified), results indicate that the magnitude of convective terms is relatively small so that they can be neglected without severely affecting information on system dynamics.

7.2 Perspectives

The modeling and computational study performed in this thesis work are just a preliminary step of a more general research activity aimed to characterize the electro-chemical function of a biological channel and, most importantly for new frontier applications, bio-synthetic devices.

In this respect, the choice of a simple one-dimensional geometrical representation of the channel should be extended to a more realistic 2D/3D description in order to better represent the morphology of the channel protein and surface charge distribution.

Results have also pointed out that the simulation domain should include a portion of the baths. This is to avoid the possibility of unphysical boundary layers at the channel ends in ion concentrations, velocities and temperatures due to Dirichlet boundary conditions. This important aspect has to be carefully taken into account in future research analysis.

More quantitative experimental investigation is finally needed to better characterize the values of important model parameters, such as the saturation velocity v_{sat}, which have proved to possibly affect in a significant manner both microscopic variables (ion concentrations, temperatures and electric field) and macroscopic variables (I-V curves) in the simulation of a nanochannel.

Acknowledgements

Voglio ringraziare il Prof. Riccardo Sacco per la disponibilità e generosità con cui mi ha seguito lungo tutte le fasi di sviluppo della tesi, aiutandomi con suggerimenti, appunti, correzioni e proficue discussioni, andando ben oltre gli obblighi della professione.

I want to thank Prof. Joseph W. Jerome for being my co-advisor and for precious comments and remarks.

Ringrazio la mia famiglia che mi ha supportato, finanziato e sopportato in questi anni di studio.

Saluto i compagni dell'Università: Andrea, Francesco, Steve, Paolo e Stefano.

Fabio Manganini

Appendix A

Some notes on the Discontinuous-Galerkin method

In many problems of practical interest, *convection* plays an important role: meteorology, weather-forecasting, oceanography, gas dynamics, aeroacoustics, turbomachinery, turbulent flows, granular flows, oil recovery simulation, modeling of shallow water, transport of contaminant in porous media, viscoelastic flows, semiconductor device simulation, magneto-hydrodynamics, and electromagnetism, among many others. It is well known that, due to the convective terms, the exact solution of (nonlinear) purely convective problems develops discontinuities in a finite time, even for smooth initial data.
The standard Continuous Galerking (CG) method imposes *a-priori* the continuity of the approximate solution; this leads to globally coupled systems, i.e. systems where a change in a data at one node affects (at least in principle) the solution at all nodes. Thus, for a purely hyperbolic problem or, more in general, for problems with dominant convection where discontinuous solutions may arise, it seems more appropriate to use the DG method because it does not force any continuity requirement at interelement boundaries.

In this appendix, we provide a short description of the Discontinuous Galerking (DG) method. For a detailed history of its developement over the years, we refer to [29] and to all references cited therein.

A.1 The DG method for a scalar linear advection-diffusion problem

The DG method was first introduced in 1973 by Reed an Hill [79] for solving the hyperbolic linear equation for neutron transport

$$\sigma u + \operatorname{div}(\mathbf{a}u) = f \quad \text{in } \Omega \tag{A.1}$$

where Ω is a bounded polygon, σ is a real number and $\mathbf{a}$ a constant vector convective field. To describe the DG method, we construct a triangulation $\mathcal{T}_h = \{K\}$ of Ω, multiply the equation by a test function v and integrate over K. After formal integration by parts, we get

$$\sigma(u,v)_K - (u, \mathbf{a}\cdot\nabla v)_K + \langle \mathbf{a}\cdot\mathbf{n}_K u, v\rangle_{\partial K} = (f,v)_K$$

where $\mathbf{n}_K$ denotes the outward unit normal of ∂K, and

$$(u,v)_K = \int_K uv\, dK \qquad \langle w,v\rangle_{\partial K} = \int_{\partial K} wv\, d\sigma.$$

Next, we take our approximate solution u_h to be a polynomial of degree at most k on each element K of the triangulation. The approximate solution u_h is then determined as the unique solution of the following weak formulation

$$\forall K \in \mathcal{T}_h : \sigma\,(u_h,v)_K - (u_h, \mathbf{a}\cdot\nabla v)_K + \left\langle \hat{h}, v\right\rangle_{\partial K} = (f,v)_K\,, \quad \forall v \in P_k(K)$$

where $P_k(K)$ denotes the space of polynomials of degree at most k on the element K and $\hat{h}$ is the *numerical flux* given by

$$\hat{h}(\mathbf{x}) = \mathbf{a}\cdot\mathbf{n}_K(\mathbf{x}) \lim_{s\downarrow 0} u_h(\mathbf{x} - s\mathbf{a}).$$

Note that the quantity $\lim_{s\downarrow 0} u_h(\mathbf{x} - s\mathbf{a})$ is nothing but the value of u_h upstream the characteristic direction $\mathbf{a}$. As a consequence, the degrees of freedom of u_h in the element K can be computed in terms of the values of u_h upstream the characteristic hitting ∂K. In other words, the approximate solution u_h can be computed element by element when the elements are suitably ordered according to the carachteristic direction $\mathbf{a}$, see Figure A.1.

Since DG methods assume discontinuous approximate solutions, they can be considered as generalizations of finite volume methods. As a consequence, the DG methods incorporate the ideas of *numerical fluxes* and *slope limiters* into the finite element framework in a very natural way. Owing to their finite element nature, the DG methods have the following advantages over classical finite volume and finite differences methods [29]:

- DG methods of arbitrarily high formal order of accuracy can be obtained by suitably choosing over each element $K \in \mathcal{T}_h$ the degree of the approximating polynomials according to the local regularity of the exact solution;

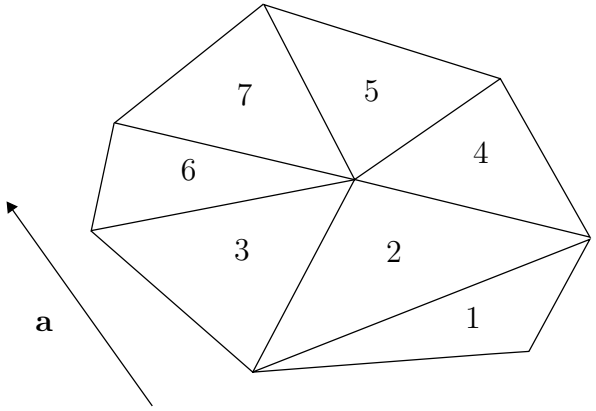

Figure A.1: The order in which u_h may be calculated is indicated.

- DG methods are highly parallelizable. Since the elements are discontinuous, the mass matrix is block diagonal and since the size of the blocks is equal to the number of degrees of freedom inside the corresponding elements, the blocks can be inverted by hand.
- DG methods are very well suited for handling complicated geometries and require an extremely simple treatment of the boundary conditions in order to achieve uniformly high-order accuracy.
- DG methods can easily handle adaptivity strategies since refinement or unrefinement of the grid can be achieved without taking into account the continuity restrictions typical of conforming finite element methods. Moreover, the degree of the approximating polynomial can be easily changed from one element to the other. Adaptivity is of particular importance in hyperbolic problems given the complexity of the structure of the discontinuities.

A.2 The DG method for the HD model

The DG method introduced for the numerical solution of (A.1) can be extended to deal with linear/non linear hyperbolic systems and, also, with parabolic and elliptic equations. Here, we focus the attention to nonlinear, convection-diffusion systems of the form

$$\frac{\partial \mathbf{u}}{\partial t} + \mathbf{div}\,\mathbf{F}(\mathbf{u}) = \mathbf{R}(\mathbf{u}), \quad \text{in } (0,T)\times\Omega. \tag{A.2}$$

As a special case, we briefly illustrate the Runge-Kutta DG method (RKDG) applied to the hydrodynamic model for semiconductor device sim-

ulation, following the work done in [26]. The HD model of Section 2.3 for $\mathbf{u} = (\nu, p_x, p_y, p_z, W_\nu)^t$ can be written in the form (A.2) by introducing the *flux function* $\mathbf{F}(\mathbf{u}) = (\mathbf{f}_x, \mathbf{f}_y, \mathbf{f}_z)$ with the following components:

$$\mathbf{f}_x = v_x\mathbf{u} + \begin{bmatrix} 0 \\ \nu k_B T_\nu \\ 0 \\ 0 \\ v_x \nu k_B T_\nu \end{bmatrix}; \quad \mathbf{f}_y = v_y\mathbf{u} + \begin{bmatrix} 0 \\ 0 \\ \nu k_B T_\nu \\ 0 \\ v_y \nu k_B T_\nu \end{bmatrix}; \quad \mathbf{f}_z = v_z\mathbf{u} + \begin{bmatrix} 0 \\ 0 \\ 0 \\ \nu k_B T_\nu \\ v_z \nu k_B T_\nu \end{bmatrix}.$$

The RHS is given by

$$\mathbf{R}(\mathbf{u}) = \mathbf{r}(\mathbf{u})_{\mathbf{E}} + \mathbf{r}(\mathbf{u})_{coll} + \mathbf{r}(\mathbf{u})_{heat} \tag{A.3}$$

with

$$\mathbf{r}(\mathbf{u})_{\mathbf{E}} = \mp q\nu \begin{bmatrix} 0 \\ E_x \\ E_y \\ E_x \\ \mathbf{v}\cdot\mathbf{E} \end{bmatrix}; \quad \mathbf{r}(\mathbf{u})_{coll} = -\begin{bmatrix} 0 \\ p_x/\tau_{p_\nu} \\ p_y/\tau_{p_\nu} \\ p_z/\tau_{p_\nu} \\ (W_\nu - W_{0\nu})/\tau_{w_\nu} \end{bmatrix};$$

$$\mathbf{r}(\mathbf{u})_{heat} = \begin{bmatrix} 0 \\ 0 \\ 0 \\ 0 \\ \text{div } (\kappa \nabla T_\nu) \end{bmatrix}$$

Notice that the convective terms are grouped in $\mathbf{F}(\mathbf{u})$, while diffusive and reacting terms lie in $\mathbf{R}(\mathbf{u})$, so that the LHS of (A.2) defines a nonlinear hyperbolic operator. To proceed, we introduce a triangulation $\mathcal{T}_h$ of the domain Ω into rectangles R. Then for each time $t \in (0, T]$, each of the components of the approximate solution $\mathbf{u}_h(t)$ is taken in the space

$$V_h = \{p \in L^\infty(\Omega) : p_{|R} \text{ is linear}, \forall R \in \mathcal{T}_h\}. \tag{A.4}$$

Equation (A.2) can be discretize in space by using the DG method, described in details later. Thus, the resulting discrete equations can be rewritten as the following system of ODEs:

$$\frac{d\mathbf{u}_h}{dt} = \mathbf{L}_h(\mathbf{u}_h) + \mathbf{R}(\mathbf{u}_h), \quad t \in (0, T),$$
$$\mathbf{u}_h(t = 0) = \mathbf{u}_{0h},$$

where $\mathbf{L}_h$ is the approximation of $-\mathbf{div}\,\mathbf{F}$ and $\mathbf{u}_{0h}$ is the approximation of the initial condition $\mathbf{u}(t=0)=\mathbf{u}_0$. This system of ODEs is discretized with a second-order Runge-Kutta method, and the resulting scheme can be written as:

$$\begin{aligned}\mathbf{u}_h^* &= \mathbf{u}_h^n + \Delta t\,(\mathbf{L}_h(\mathbf{u}_h^n) + \mathbf{R}(\mathbf{u}_h^n)\,;\\ \mathbf{u}_h^{**} &= \mathbf{u}_h^{**} + \Delta t\,(\mathbf{L}_h(\mathbf{u}_h^n) + \mathbf{R}(\mathbf{u}_h^n)\,;\\ \mathbf{u}_h^{n+1} &= \frac{1}{2}(\mathbf{u}_h^{**} + \mathbf{u}_h^*).\end{aligned}$$

where the superscript n indicates the solution at time $t = n\Delta t$. The Runge-Kutta time discretization is explicit and thus the method is stable under the condition

$$\frac{\partial \mathbf{F}}{\partial \mathbf{u}}\frac{\Delta t}{\Delta x} < \frac{1}{3}$$

To illustrate the DG discretization for equation (A.2), we denote by $u^{(k)}$ the k-th component of $\mathbf{u}$, then we multiply each k-th scalar equation in (A.2) by $v_h \in V_h$, integrate over each $R \in \mathcal{T}_h$, replace the exact solution $\mathbf{u}$ with its approximation $\mathbf{u}_h$, and formally integrate by parts to obtain

$$\begin{aligned}\frac{d}{dt}\int_R u_h^{(k)} v_h\,d\mathbf{x} + \sum_{e\in\partial R}\int_e \mathbf{F}^{(k)}(\mathbf{u}_h)\cdot\mathbf{n}_e v_h\,ds - \int_R \mathbf{F}^{(k)}(\mathbf{u}_h)\cdot\nabla v_h\,d\mathbf{x}\\ = \int_R \mathbf{R}^{(k)}(\mathbf{u}_h) v_h\,d\mathbf{x}, \qquad \forall v_h \in V_h,\end{aligned}$$

where $\mathbf{n}_e$ is outward unit normal to the edge e, and $\mathbf{F}^{(k)} = (f_x^{(k)}, f_y^{(k)}, f_z^{(k)})^t$. The quantity $\mathbf{F}^{(k)}(\mathbf{u}_h)\cdot\mathbf{n}_e$ does not have a precise meaning since $\mathbf{u}_h$ is discontinuous at $\mathbf{x} \in e \in \partial R$, so that it must be replaced with a numerical flux $\mathbf{h}_{e,R} \simeq \mathbf{F}(\mathbf{u}_h)\cdot\mathbf{n}_e$ defined for $\mathbf{x} \in e \in \partial R$ as:

$$\mathbf{h}_e(\mathbf{x}) = \frac{1}{2}\left\{\mathbf{F}(\mathbf{u}_h^{int}(\mathbf{x}))\cdot\mathbf{n}_e + \mathbf{F}(\mathbf{u}_h^{ext}(\mathbf{x}))\cdot\mathbf{n}_e - \alpha_e\left(\mathbf{u}_h^{ext}(\mathbf{x}) - \mathbf{u}_h^{int}(\mathbf{x})\right)\right\}$$

where

$$\begin{aligned}\mathbf{u}_h^{int}(\mathbf{x}) &= \lim_{\substack{\mathbf{x}'\to\mathbf{x}\\ \mathbf{x}'\in R}} \mathbf{u}_h(\mathbf{x}')\\ \mathbf{u}_h^{ext}(\mathbf{x}) &= \lim_{\substack{\mathbf{x}'\to\mathbf{x}\\ \mathbf{x}'\in R^C}} \mathbf{u}_h(\mathbf{x}')\end{aligned}$$

and

$$\alpha_e = \max\{\lambda(\bar{\mathbf{u}}_R); \lambda(\bar{\mathbf{u}}_{R_{next}})\},$$

and R_{next} is the rectangle adjacent to edge e, $\bar{\mathbf{u}}_R$ is the mean of $\mathbf{u}_h$ on R and

$$\lambda(\mathbf{u}) = \sqrt{\frac{5}{3}k_B T/m} + |\mathbf{v}|,$$

is an upper bound for the eigenvalues of the Jacobian of $\mathbf{F} \cdot \eta$ evaluated at $\mathbf{u} = (\nu, p_x, p_y, p_z, W_\nu)$ for all unit vectors η.

Appendix B

Functional Analysis

Let us assume V and W to be normed function spaces endowed with the norms $\|\cdot\|_V$ and $\|\cdot\|_W$, respectively.

Definition B.1 (Linear Functionals)**.** *Let v be an arbitrary element of V. We call* linear functional *from V into W every correspondance $l = l(v) : V \to W$ such that*

$$l(\alpha v + \beta w) = \alpha l(v) + \beta l(w) \qquad v, w \in V \qquad \alpha, \beta \in \mathbb{R}. \tag{B.1}$$

We also say that l is continuous *if there exists a positive constant M_l such that*

$$|l(v)| \leq M_l \|v\|_V \qquad \forall\, v \in V. \tag{B.2}$$

We denote by $L(V;W) : V \to W$ the set of real-valued linear continuous functionals $l(v)$ from V into W. The norm on $L(V;W)$ is defined as

$$\|l\|_{L(V;W)} := \sup_{v \in V, v \neq 0} \frac{\|l(v)\|_W}{\|v\|_V}. \tag{B.3}$$

We introduce the *Fréchet derivative* of the nonlinear operator F, evaluated at $v \in V$, defined as:

$$w \to F'(v)w := \lim_{\eta \to 0} \frac{F(v + \eta w) - F(v)}{\eta} \qquad \forall\, w \in V. \tag{B.4}$$

From the definition (B.4), we see that:

$$F' : V \to L(V;V), \tag{B.5}$$

that is, $F'(\cdot)$ is a linear operator from V into $L(V;V)$, acting on the generic element w belonging to the normed function space V.

Definition B.2 (Ball in V)**.** *Let z be an arbitrary element of V. For $\varepsilon > 0$, we define the ball of radius ε and centered at z as*

$$B(z;\varepsilon) := \{x \in V s.t. \|x - v\|_V < \varepsilon\}. \tag{B.6}$$

Appendix C

List of symbols

Symbol	Meaning	Units
$\mathbf{x}$	position vector	m
t	time variable	s
z	ionic valence	
m	particle mass	Kg
T	temperature	K
ϕ	electric potential	V
ϕ_ν	electrochemical potential	V
V_{th}	thermal potentail	V
$\mathbf{E}$	electric field	$\mathrm{V\,m^{-1}}$
$\mathbf{J}$	current density	$\mathrm{A\,m^{-2}}$
ρ	charge density	$\mathrm{C\,m^{-3}}$
ν, p, n	particle concentration	$\mathrm{m^{-3}}$
N_{ref}	reference concentration	$\mathrm{m^{-3}}$
$\mathbf{v}$	particle velocity	$\mathrm{m\,s^{-1}}$
$\mathbf{p}$	momentum density	$\mathrm{Kg\,m^{-2}\,s^{-1}}$
$\mathbf{u}$	group velocity	$\mathrm{m\,s^{-1}}$
$\mathbf{k}$	waves number	$\mathrm{m^{-1}}$
$\mathbf{F}$	total forces	$\mathrm{J\,m^{-1}}$
$\mathbf{P}$	pressure tensor	$\mathrm{J\,m^{-3}}$
e_I	internal energy density	$\mathrm{J\,Kg^{-1}}$
$\mathbf{q}$	heat flux	$\mathrm{W\,m^{-2}}$
W	total energy density	$\mathrm{J\,m^{-3}}$
w	total energy	J
τ	relaxation time	s
ϵ	dielectric permettivity	$\mathrm{F\,m^{-1}}$

N_{dop}	doping profile	m^{-3}
κ	thermal conductivity	$\mathrm{W\,m^{-1}\,K^{-1}}$
ς	electrical conductivity	$\mathrm{S\,m^{-1}}$
σ	surface charge denisty	$\mathrm{C\,m^{-2}}$
D	diffusion coefficient	$\mathrm{m^2\,s^{-1}}$
μ	electrical mobility	$\mathrm{m^2\,V^{-1}\,s^{-1}}$
c	specific heat	$\mathrm{J\,K^{-1}\,Kg^{-1}}$
ϱ	mass density	$\mathrm{Kg\,m^{-3}}$
Q_{tot}	total charge	C
a	channel radius	m
L	channel length	m
V_{app}	externally applied bias	V
v_{sat}	saturation velocity	$\mathrm{m\,s^{-1}}$

Symbol	**Meaning**	**Units**	**Value**
q	electron charge	C	1.602×10^{-19}
k_B	Boltzmann's constant	$\mathrm{J\,K^{-1}}$	1.380×10^{-23}
$\bar{h}$	reduced Planck's constant	$\mathrm{J\,s^{-1}}$	1.054×10^{-34}

Bibliography

[1] A.J.Storm, J.H.Chen, X.S.Ling, H.W.Zandbergen, and C.Dekker. Fabrication of solid-state nanopores with single-nanometre precision. *Nature Materials*, 2:537–540, 2003.

[2] A.M. Anile and S. Pennisi. Thermodynamic derivation of the hydrodynamical model for charge transport in semiconductors. *Phys. Rev. B*, 46:13186–13193, 1992.

[3] P.Yu Apel, Yu.E. Korchev, Z.S. Siwy, R. Spohr, and M. Yoshida. Diode-like single-ion track membrane prepared by electro-stopping. *Nuclear Instruments and Methods in Physics Research Section B: Beam Interactions with Materials and Atoms*, 184(3):337 – 346, 2001.

[4] D.N Arnold and F. Brezzi. Mixed and nonconforming finite element methods: implementation, postprocessing and error estimates. *Math. Modeling and Numer. Anal.*, 19(1):7–32, 1985.

[5] I. Babuska. Error-bounds for finite element method. *Numerische Mathematik*, 16:322–333, 1971.

[6] G. Baccarani and M.R. Wordeman. An investigation of steady-state velocity overshoot in silicon. *Solid-State Electronics*, 28(4):407 – 416, 1985.

[7] L. Ballestra, S. Micheletti, and R. Sacco. Semiconductor device simulation using a viscous-hydrodynamic model. *Computer Methods in Applied Mechanics and Engineering*, 191:5447–5466, 2002.

[8] V. Barcilon. Ion flow through narrow membrane channels: part I. *SIAM J. Appl. Math.*, 52(5):1391–1404, 1992.

[9] V. Barcilon, D. Chen, R.S. Eisenberg, and J.W. Jerome. Qualitative properties of steady-state Poisson-Nernst-Planck systems: perturbation and simulation study. *SIAM J. Appl. Math.*, 57(3):631–648, 1997.

[10] V. Barcilon, R. S. Eisenberg, and D. P. Chen. Ion flow through narrow membrane channels: part II. *SIAM J. Appl. Math.*, 52(5):1405–1425, 1992.

[11] A.J. Bard and L.K. Faulkner. *Electrochemical Methods*. John Wiley & Sons, 2 edition, 2001.

[12] K. Blotekjaer. Transport equations for electrons in two-valley semiconductors. *Electron Devices, IEEE Transactions on*, 17(1):38–47, 1970.

[13] M. Brera, J.W. Jerome, Y. Mori, and R. Sacco. A conservative and monotone mixed-hybridized finite element approximation of transport problems in heterogeneous domains. *Computer Methods in Applied Mechanics and Engineering*, 199(41-44):2709 – 2720, 2010.

[14] F. Brezzi. On the existence, uniqueness and approximation of saddle-point problems arising from lagrangian multipliers. *ESAIM: Mathematical Modelling and Numerical Analysis - Modélisation Mathématique et Analyse Numérique*, 8(R2):129–151, 1974.

[15] H. Cao, Z. Yu, J. Wang, J.O. Tegenfeldt, R.H. Austin, E. Chen, W. Wu, and S.Y. Chou. Fabrication of 10 nm enclosed nanofluidic channels. *Applied Physics Letters*, 81:174–176, 2002.

[16] A.H. Carter. *Classical and Statistical Thermodynamics*. Prentice Hall PTR, 2001.

[17] C. Cercignani. *Boltzmann Equation*. Applied Mathematical Sciences Series. Springer-Verlag, 1988.

[18] D. P. Chen, V. Barcilon, and R. S. Eisenberg. Constant fields and constant gradients in open ionic channels. *Biophysical journal*, 61(5):1372–1393, 1992.

[19] D. P. Chen and R. S. Eisenberg. Charges, currents, and potentials in ionic channels of one conformation. *Biophysical journal*, 64(5):1405–1421, 1993.

[20] D. P. Chen and R. S. Eisenberg. Flux, coupling, and selectivity in ionic channels of one conformation. *Biophysical journal*, 65:727–746, 1993.

[21] D. P. Chen, R. S. Eisenberg, A. Tripathy, L. Xu, and Meissner G. Permeation through the calcium release channel of cardiac muscle. *Biophysical journal*, 73(3):1337–1354, 1997.

[22] D. P. Chen, R. S. Eisenberg, A. Tripathy, L. Xu, and Meissner G. Selectivity and permeation in calcium release channel of cardiac muscle: Alkali metal ions. *Biophysical journal*, 76:1346–1366, 1999.

[23] D. P. Chen, R. S. Eisenberg, A. Tripathy, L. Xu, and Meissner G. Calcium ion permeation through the calcium release channel (ryanodine receptor) of cardiac muscle. *Physical Chemistry*, 107:9139–9145, 2003.

[24] D.P. Chen, R.S. Eisenberg, J.W. Jerome, and C.W. Shu. Hydrodynamic model of temperature change in open ionic channels. *Biophysical Journal*, 69(6):2304 – 2322, 1995.

[25] P. Chen, T. Mitsui, D.B. Farmer, J. Golovchenko, R.G. Gordon, and D. Branton. Atomic layer deposition to fine-tune the surface properties and diameters of fabricated nanopores. *Nano Letters*, 4:1333–1337, 2004.

[26] Z. Chen, B. Cockburn, J.W. Jerome, and C.W. Shu. Mixed-RKDG finite element methods for the 2-d hydrodynamic model for semiconductor device simulation. *VLSI Design*, 3(2):145–158, 1995.

[27] L.J. Cheng and L.J Guo. Nanofluidic diodes. *Chem Soc Rev*, 39(3):923–938, 2010.

[28] P. Ciampolini, A. Pierantoni, A.Liuzzo, and G. Baccarani. 3-D simulations of silicon devices: Physical models and numerical algorithms. In G. Baccarani, editor, *Process and Device Modeling for Microelectronics*, chapter 2, pages 53–107. Elsevier, 1993.

[29] B. Cockburn, G.E. Karniadakis, and C.W. Shu. The development of Discontinuous Galerkin methods, 1999.

[30] D. Constantin and Z.S. Siwy. Poisson-Nernst-Planck model of ion current rectification through a nanofluidic diode. *Phys. Rev. E*, 76:041202, 2007.

[31] R.K. Cook and J. Frey. An efficient technique for two-dimensional simulation of velocity overshoot effects in si and gaas devices. *COMPEL: The International Journal for Computation and Mathematics in Electrical and Electronic Engineering*, 1(2):65 – 87, 1982.

[32] H. Daiguji, Y. Oka, and K. Shirono. Nanofluidic diode and bipolar transistor. *Nano Letters*, 5(11):2274–2280, 2005.

[33] H. Daiguji, P. Yang, and A. Majumdar. Ion transport in nanofluidic channels. *Nano Letters*, 4:137–142, 2004.

[34] C. Dekker. Solid-state nanopores. *Nature Nanotech.*, 2:209–215, 2007.

[35] T. Desai, D. Hansford, L. Kulinsky, A. Nashat, G. Rasi, J. Tu, Y. Wang, M. Zhang, and M. Ferrari. Nanopore technology for biomedical applications. *Biomedical Microdevices*, 2(1):11–40, 1999.

[36] J Douglas and J. E. Roberts. Global estimates for mixed methods for second order elliptic equations. *Math. Comp.*, 44:39–52, 1985.

[37] J. Edsall and J. Wyman. *Biophysical Chemistry.* Academic Press, NY, 1958.

[38] R.S. Eisenberg. Ions in fluctuating channels: Transistors alive. *Fluct. Noise Lett.*, 11, 2012.

[39] R. Fan, M. Yue, R. Karnik, A. Majumdar, and P. Yang. Polarity switching and transient responses in single nanotube nanofluidic transistors. *Phys. Rev. Lett.*, 95, 2005.

[40] A. Forghieri, R. Guerrieri, P. Ciampolini, A. Gnudi, M. Rudan, and G. Baccarani. A new discretization strategy of the semiconductor equations comprising momentum and energy balance. *Computer-Aided Design of Integrated Circuits and Systems, IEEE Transactions on*, 7(2):231–242, 1988.

[41] C.L. Gardner, W. Nonner, and R.S. Eisenberg. Electrodiffusion model simulation of ionic channels: 1d simulations. *Journal of Computational Electronics*, 3(1):25–31, 2004.

[42] A. Gnudi, F. Odeh, and M. Rudan. Investigation of non-local transport phenomena in small semiconductor devices. *European Transactions on Telecommunications*, 1(3):307–312, 1990.

[43] H.K. Gummel. A self-consistent iterative scheme for one-dimensional steady state transistor calculations. *IEEE Trans. Electron Devices*, ED-11:455–465, 1964.

[44] A.C. Guyton and J.E. Hall. *Textbook of Medical Physiology.* Elsevier, 11 edition, 2006.

[45] C.C. Harrell, Y. Choi andL.P. Horne, L.A. Baker, Z.S. Siwy, and C.R. Martin. Resistive-pulse DNA detection with a conical nanopore sensor. *Langmuir*, 22, 2006.

[46] A. Harten, B. Engquist, S. Osher, and S.R. Chakravarthy. Uniformly high order accurate essentially non-oscillatory schemes, {III}. *Journal of Computational Physics*, 131(1):3 – 47, 1997.

[47] B. Hille. *Ionic Channels of Excitable Membranes*. Sinauer Associates, Incorporated, 2001.

[48] K. Huang. *Statistical Mechanics*. John Wiley & Sons, 2 edition, 1987.

[49] J.D Jackson. *Classical Electrodynamics*. Wiley, 23 edition, 1998.

[50] J.W. Jerome. *Analysis of charge transport: a mathematical study of semiconductor devices*. Springer-Verlag, 1996.

[51] J.W. Jerome. Analytical approaches to charge transport in a moving medium. *Transport Theory and Statistical Physics*, 31:333–366, 2002.

[52] J.W. Jerome, B. Chini, M. Longaretti, and R. Sacco. Computational modeling and simulation of complex systems in bio-electronics. *Journal of Computational Electronics*, 7(1):10–13, 2008.

[53] J.W. Jerome and R. Sacco. Global weak solutions for an incompressible charged fluid with multi-scale couplings: Initial-boundary value problem. *Nonlinear Analysis*, 71:e2487–e2497, 2009.

[54] E.B. Kalman, I. Vlassiouk, and Z.S. Siwy. Nanofluidic bipolar transistors. *Advanced Materials*, 20(2):293–297, 2008.

[55] M. Karhanek, J.T Kemp, N. Pourmand, R.W. Davis, and C.D Webb. Single DNA molecule detection using nanopipettes and nanoparticles. *Nano Letters*, 5:403–407, 2005.

[56] R. Karnik, C. Duan, K. Castelino, H. Daiguji, and A. Majumdar. Rectification of ionic current in a nanofluidic diode. *Nano Letters*, 7(3):547–551, 2007.

[57] R. Karnik, R. Fan, M. Yue, D. Li, P. Yong, and A. Majumdar. Electrostatic control of ions and molecules in nanofluidic transistors. *Nano Letters*, 5:943–948, 2005.

[58] T. Kerkhoven and Y. Saad. On acceleration methods for coupled nonlinear elliptic systems. *Numerische Mathematik*, 60:525–548, 1992.

[59] J. Koryta and K. Stulik. *Ion-Selective Electrodes*. Cambridge University Press, 1983.

[60] L.D. Landau and E.M. Lifshitz. *Mechanics. Course of Theoretical Physics*, volume 1. Pergamon press, 2 edition, 1969.

[61] S.E. Laux, M.V. Fischetti, and D.J. Frank. Monte Carlo analysis of semiconductor devices: the DAMOCLES program. *IBM J. Res. Dev.*, 34(4):466–494, 1990.

[62] A.A. Lev, Y.E. Korchev, T.K. Rostovtseva, C.L. Bashford, D.T. Edmonds, and C.A. Pasternak. Rapid switching of ion current in narrow pores: Implications for biological ion channels. *Proceedings: Biological Sciences*, 252:187–192, 1993.

[63] R. A. Levis and J. L. Rae. Technology of patch- clamp electrodes. In A. A. Boulton, G. B. Baker, and W. Walz, editors, *Patch-Clamp Applications and Protocols*, volume 26 of *Neuromethods*, pages 1–36. Humana Press, 1995.

[64] J. Li, D. Stein, C. McMullan, D. Branton, M.J. Aziz, , and J.A. Golovchenko. Ion-beam sculpting at nanometre length scales. *Nature*, 412:166–169, 2001.

[65] R.L. Liboff. *Introduction to the Theory of Kinetic Equations*. John Wiley & Sons, New York, 1 edition, 1969.

[66] D.R. Lide. *Handbook of Organic Solvents*. CRC Press, 1994.

[67] M. Longaretti, B. Chini, J.W. Jerome, and R. Sacco. Electrochemical modeling and characterization of voltage operated channels in nano-bioelectronics. *Sensor Letters*, 6(1):49–56, 2008.

[68] A. Mara, Z.S. Siwy, C. Trautmann, J. Wan, and F. Kamme. An asymmetric polymer nanopore for single molecule detection. *Nano Letters*, 4:497–501, 2004.

[69] G. Marino, J. W. Jerome, B. Chini, M. Longaretti, and R. Sacco. Computational models in nano-bio-electronics: simulation of ionic transport in voltage operated channels. *Journal of Nanoscience and Nanotechnology*, 8(7):1–9, 2007.

[70] P.A. Markowich, C.A. Ringhofer, and C. Schmeiser. *Semiconductor Equations*. Springer-Verlag, 1990.

[71] M.Rudan and F.Odeh. Multi-dimensional discretization scheme for the hydrodynamic model of semiconductor devices. *COMPEL: The*

International Journal for Computation and Mathematics in Electrical and Electronic Engineering, 5(3):149 – 183, 1986.

[72] M.Rudan, F.Odeh, and J.White. Numerical solution of the hydrodynamic model for a one-dimensional semiconductor device. *COMPEL: The International Journal for Computation and Mathematics in Electrical and Electronic Engineering*, 6(3):151 – 170, 1987.

[73] J.P. Nougier, J.C. Vaissiere, D.Gasquet, J.Zimmermann, and E. Constant. Determination of transient regime of hot carriers in semiconductors, using the relaxation time approximations. *Journal of Applied Physics*, 52(2):825–832, 1981.

[74] J.T. Oden and J.N. Reddy. On mixed finite element approximations. *SIAM J. Numer. Anal.*, 3(12):393–404, 1976.

[75] J.H. Park and J.W. Jerome. Qualitative properties of steady-state Poisson-Nernst-Planck systems: mathematical study. *SIAM J. Appl. Math.*, 57(3):609–630, 1997.

[76] T.H.H. Pian. Finite element formulation by variational principles with relaxed continuity requirements. In A.K. Aziz, editor, *The Mathematical Foundation of the Finite Element Method with Application to Partial Differential Equations*. Academic press, New York, 1972.

[77] A. Plecis, R.B. Schoch, and R. Renaud. Ionic transport phenomena in nanofluidics: experimental and theoretical study of the exclusion-enrichment effect on a chip. *Nano Letters*, 5:1147–1155, 2005.

[78] A. Quarteroni and A. Valli. *Numerical Approximation of Partial Differential Equations*. Springer-Verlag, 1997.

[79] W.H. Reed and T.R. Hill. Triangular mesh methods for the neutron transport equation. In *National topical meeting on mathematical models and computational techniques for analysis of nuclear systems*. 1973.

[80] K. Rohit, K. Castelino, and A. Majumdar. Field-effect control of protein transport in a nanofluidic transistor circuit. *Appl. Phys. Lett.*, 88, 2006.

[81] I. Rubinstein. *Electrodiffusion of Ions*. SIAM, 1990.

[82] M. Rudan, A. Gnudi, and W. Quade. A generalized approach to the hydrodynamic model of semiconductor equations. In G. Baccarani, editor, *Process and Device Modeling for Microelectronics*, chapter 2, pages 109–154. Elsevier, 1993.

[83] B. Sakmann and E. Neher. *Single-channel Recording*. Springer Science+Business Media, 2009.

[84] O.A. Saleh and L.L Sohn. An artificial nanopore for molecular sensing. *Nano Letters*, 3:37–38, 2003.

[85] D.L. Scharfetter and H.K. Gummel. Large signal analysis of a silicon Read diode oscillator. *IEEE Trans. Electron Devices*, ED-16(1):64–77, 1969.

[86] M. Schmuck. Analysis of the Navier-Stokes-Nernst-Planck-Poisson system. *Mathematical Models and Methods in Applied Sciences*, 19(6):993–1015, 2009.

[87] S.G. Schultz. *Molecular Biology of Membrane Transport Disorders*. Springer, 1996.

[88] S. Selberherr. *Analysis and Simulation of Semiconductor Devices*. Springer-Verlag, 1984.

[89] C.W. Shu and S. Osher. Efficient implementation of essentially non-oscillatory shock-capturing schemes. *Journal of Computational Physics*, 77(2):439 – 471, 1988.

[90] C.W. Shu and S. Osher. Efficient implementation of essentially non-oscillatory shock-capturing schemes, {II}. *Journal of Computational Physics*, 83(1):32 – 78, 1989.

[91] M.S. Shur. Influence of nonuniform field distribution on frequency limits of gaas field-effect transistors. *Electronics Letters*, 12:615–616, 1976.

[92] Z.S. Siwy. Ion-current rectification in nanopores and nanotubes with broken symmetry. *Advanced Functional Materials*, 16(6):735–746, 2006.

[93] Z.S. Siwy, P. Apel, D. Baur, D.D. Dobrev, Y.E. Korchev, R. Neumann, R. Spohr, C. Trautmann, and K.O. Voss. Preparation of synthetic nanopores with transport properties analogous to biological channels. *Surface Science*, 532-535(0):1061 – 1066, 2003.

[94] Z.S. Siwy, E. Heins, C.C Harrell, P. Kohli, and C.R. Martin. Conical-nanotube ion-current rectifiers: the role of surface charge. *Journal of the American Chemical Society*, 126(35), 2004.

[95] R. Stratton. Diffusion of hot and cold electrons in semiconductor barriers. *Physical Review*, 126(6):2002 – 2014, 1962.

[96] L. Stryer, J.M. Berg, and J.L. Tymoczko. *Biochemistry*. New York: W.H.Freeman., 2002.

[97] R.C. Tolman. *The Principles of Statistical Mechanics*. Dover Books on Physics. Dover Publications, 1938.

[98] P. Tong. New displacement hybrid finite element models for solid continua. *International Journal for Numerical Methods in Engineering*, 2(1):73–83, 1970.

[99] S. Umehara, N. Pourmand, C.D. Webb, R.W Davis, K. Yasuda, and M. Karhanek. Current rectification with poly-l-lysine-coated quartz nanopipettes. *Nano Letters*, 6(11):2486–2492, 2006.

[100] I. Vlassiouk and Z.S. Siwy. Nanofluidic diode. *Nano Letters*, 7(3):552–556, 2007.

[101] I. Vlassiouk, S. Smirnov, and Z.S. Siwy. Ionic selectivity of single nanochannels. *Nano Letters*, 8(7):1978–1985, 2008.

[102] I. Vlassiouk, S. Smirnov, and Z.S. Siwy. Nanofluidic ionic diodes. comparison of analytical and numerical solutions. *ACS Nano*, 2(8):1589–1602, 2008.

[103] C. Wei, A.J. Bard, and S.W. Feldberg. Current rectification at quartz nanopipet electrodes. *Analytical Chemistry*, 69(22):4627–4633, 1997.

[104] Q. Xia, K.J. Morton, R.H. Austin, and S.Y Chou. Sub-10 nm self-enclosed self-limited nanofluidic channel arrays. *Nano Letters*, 8:3830–3833, 2008.

[105] E. Zeidler. *Vol I: Fixed point theorems*. Nonlinear Functional Analysis and Its Applications. Springer-Verlag, 1986.

[106] B. Zhang, Y. Zhang, and H.S. White. The nanopore electrode. *Analytical Chemistry*, 76(21):6229–6238, 2004.